DISSIPATIVE PARTICLE DYNAMICS SIMULATION FOR SELF-ASSEMBLY OF POLYMER AND SURFACTANT SOLUTION

By

MING-TSUNG LEE

A dissertation submitted to the

Graduate School-New Brunswick

Rutgers, The State University of New Jersey

In partial fulfillment of the requirements

For the degree of

Doctor of Philosophy

Graduate Program in Chemical and Biochemical Engineering

Written under the direction of

Alexander V. Neimark

And approved by

_____

_____

_____

_____

_____

New Brunswick, New Jersey

October, 2015

ABSTRACT OF THE DISSERTATION

DISSIPATIVE PARTICLE DYNAMICS SIMULATION FOR SELF-ASSEMBLY OF POLYMER AND SURFACTANT SOLUTION

by MING-TSUNG LEE

Dissertation Director:

Alexander V. Neimark

Dissipative Particle Dynamics (DPD) is a mesoscale tool bridging the gap between microscopic atomistic simulation and macroscopic thermophysical modeling. After its interaction parameters are mapped to the Flory-Huggins parameters (Groot and Warren, Journal of Chemical Physics, 1997), DPD has become very popular in studying the self-assembly of polymer and surfactant solution. Although DPD has demonstrated the capability to qualitatively describe the equilibrium morphology of soft matter, quantitative prediction compared with experiments is rarely achieved. The reasons are, non-separately, the ambiguous physical unit interpretations and the case-dependent force field parameterizations. Here we present a scale-bridging method to extract both microscopic and macroscopic information for parameterization. The interaction parameters are calibrated by Monte Carlo simulation and mapped to infinite dilute coefficient of the reference compounds in the coarse grained particles. The robustness and consistency of the parameterization are examined against the experimental micellar properties of several surfactants, by varying coarse grained levels and reference compounds.

Modeling dynamic properties in self-assembled materials using DPD is even tricky. A practical example is to model proton transfer of polyelectrolyte membrane (PEM) in the fuel cell, where proton dissociates from the acidic sites of hydrated PEM and transfer within the hydrophilic domain. Such detailed, reaction-like behavior can't be quantified directly from the simulation due to the simplicity of current DPD model. One would need to either correlate the morphology to the proton diffusivity by empirical equations, or perform inverse mapping and continue with expensive atomistic simulations. Here we present an advanced approach which describes the proton dynamics in water as well as its dissociation equilibrium from the acid. Combined with the scale-bridging parameterization, the model predicts the morphology, water transfer, and proton conductivity of sulfonated polystyrene at several sulfonation and hydration levels, and has very good agreements with experimental measurement and atomistic simulation results.

Acknowledgements

My most sincere gratitude to my thesis advisor Professor Neimark, my mentor Dr. Vishnyakov, the colleagues I cooperated with, and, most important of all, my wife.

Table of Contents

List of tables

List of illustrations

spherical micelles (f) $\Delta a_{TW} = 19.6\ k_B T/R_c$, very stiff molecules with $K_\theta = 120$, worm-like micelles form.

p. 39, Figure 4-5. Probability distribution of finding a surfactant molecule in an aggregate consisting of N molecules for C_8E_8 at surfactant concentration of 4% vol. Line (1) (dotted): flexible model with no rigidity, $\Delta a_{TW} = 19.6 k_B T/R_c$. Line (2) (black solid): $\Delta a_{TW} = 19.6 k_B T/R_c$, rigidity applied using second neighbor harmonic bonds, $K_{1\text{-}3} = 20\ k_B T/R_c^2$. Line (3) (hollowed): $\Delta a_{TW} = 19.6 k_B T/R_c$, rigidity applied by harmonic angle potential $K_\theta = 5\ k_B T/\text{rad}^2$). Line (4) (red solid): flexible chains with no rigidity with increased tail-water repulsion $\Delta a_{TW} = 23.6\ k_B T/R_c$.

p. 41, Figure 4-6. Averaged critical micelle concentration CMC and aggregation number N_{ag} of MEGA-10 (a, b) and C_8E_8 (c, d) at 4% surfactant concentration. Parameters (independent variables) are referred to the two abscissa axis: rigidity to the bottom axis (blue) and conservative mismatch Δa_{TW} to the upper axis (red). Ordinate show CMC (a,c) and N_{ag} (b,d) of the surfactants. Blue squares show the dependence of CMC and N_{ag} on $K_{1\text{-}3}$ with a constant $\Delta a_{TW} = 19.6\ k_B T/R_c$. Red circles show the dependence of CMC and N_{ag} on tail-solvent hydrophobic mismatch Δa_{TW} for flexible chains ($K_{1\text{-}3} = 0$). Black dotted lined indicate experimental CMC values for MEGA-10 (a) and C_8E_8 (c). Error bars for of CMC are comparable with the symbol size.

p. 43, Figure 4-7. Distribution of the micelle asphericity factors in different systems. (1) Spherical micelles in C_8E_8 surfactant, $\Delta a_{TW} = 19.6\ k_B T/R_c$, rigidity applied using second neighbor bond, $K_{1\text{-}3} = 20\ k_B T/R_c^2$. (2) Non-spherical symmetric aggregates in C_8E_8 type surfactant, flexible model with stronger tail-water hydrophobic mismatch $\Delta a_{TW} = 23.6\ k_B T/R_c$, $K_{1\text{-}3} = 0$. (3) Mostly spherical micelles in MEGA-10 type surfactant, Δa_{TW}=19.6 $k_B T/R_c$, rigidity applied using the harmonic angle potential, $K_\theta = 5 k_B T/\text{rad}^2$. (4) Worm-like micelles in MEGA-10 type surfactant, $\Delta a_{TW} = 19.6\ k_B T/R_c$, very rigid model, $K_\theta = 120 k_B T/\text{rad}^2$.

p. 48, Figure 5-1. Examples of coarse-grained models of C_nE_m surfactrants with different bead diameter R_c. T beads (red) are for hydrophobic tail, and H beads (green) are for hydrophilic head. Water beads (blue) with corresponding bead size are illustrated by N_W, the number of water molecules in aW bead.

p. 53, Figure 5-2. (a) Schematics of MD-DPD mapping. Example shows the hexadecane modeled by coarse grained bead sized 0.71 nm. Each beads represents four methylene groups. Center to center bead distances are calculated for DPD model (four connected beads) for r_{12}, r_{13}, r_{14}, etc. The reference "coarse grained" MD coordinates are calculated from the center of mass from the bead components. (b-e) Normalized distribution of center-to-center bead distance from DPD (dashed lines) and of the distances between the center of masses for alkane chain fragments from atomistic MD simulations (solid lines) (f-i) Normalized distribution of center-to-center bead distance from DPD (dashed lines) and of the distances between the center of masses for PEO-400 chain fragments from atomistic MD simulations (solid lines).

Section 1. Introduction

Dissipative Particle Dynamics (DPD) has become a common tool for mesoscale modeling of self-assembly in surfactant and polymeric systems. In DPD, the system components are modeled by quasiparticles ("beads"), each of which represents several atoms that are lumped together. The beads interact via short-range soft repulsion potentials that affords superb computational efficiency. Despite the simplicity of the models, DPD provides qualitative and sometimes quantitative description of the structure and thermodynamics of quite complex systems. Examples include micellization in surfactant solutions,[1-3] morphology of cell membranes and lipid bilayers,[4-5] phase segregation in polyelectrolyte membranes,[6-8] to name a few. This thesis focuses on the micellization of surfactant and the nano-segregation of polyelectrolyte membrane, which will be introduced in the following paragraphs subsequently.

Surfactant is a amphiphilic molecule composed of hydrophobic tail and hydrophilic head. Self-assembly in surfactant solutions is ubiquitous phenomenon in natural systems and technological processes. Once the concentration of surfactant exceeds the critical micelle concentration (CMC), the surfactant molecules aggregate into micelles, which may contain from scores to hundreds of molecules. Micelles may coalesce further and form various ordered and disordered mesophases. The problem of theoretical prediction of CMC and micelle aggregation number (N_{ag}, the average number of surfactant molecules per micelle) has many important practical implications and constitutes one of the cornerstone problems in colloid science and engineering.

Micellization of ionic and non-ionic surfactants has been extensively studied using molecular simulations starting from early nineties, [9-11]. However, the attempts to quantitatively predict experimental data remain limited. The most advanced simulation studies [12-17] are based on the state-of-the-art coarse-grained molecular dynamics (CGMD) and Monte Carlo (MC) methods, including recent CGMD calculations with using graphics processing units[15] and atomistic implicit-solvent MD using EEF1 solvation model[18] designed for proteins. Despite the recent progress in CGMD simulations of micellar systems, it is desirable to elaborate a more computationally efficient method, which would be based on the use of soft repulsion potentials within the DPD framework. However, two main issues needs to be overcome to achieve the desired performance of DPD in quantitative prediction for micellar properties.

The major issue to overcome in order to achieve quantitative prediction using DPD is the parameterization of soft repulsion potentials. Pool and Bolhuis [19] performed MC simulations with the soft repulsion potentials from ref [20] and obtained extremely low values of CMC. The authors expressed doubts on the very applicability of coarse-grained models with soft repulsion potentials to qualitative predictions of such parameter-sensitive properties like CMC and suggested that hard-core solvent should be an essential feature of the coarse-grained model. DPD studies of micellization have been so far rather sparse. The authors of recent publications [21-22] studied micellization of model non-ionic surfactants of different structure and demonstrated the DPD ability of modeling the formation dynamics and equilibrium distribution of micellar aggregates, but they did not target particular experimental systems.

The main problem hindering such attempts is a lack of the verified parameters of coarse-grained soft-core potentials. In general, the coarse-grained potentials should be fitted to the thermodynamic [5, 23-24] and/or structural [5, 15, 25] properties of reference systems. For this purpose, one has to simulate the model fluid and to choose the potential parameters from the best fit of the calculated target properties to the properties of a reference fluid, obtained from atomistic simulations or experiments. Liquid-liquid equilibria and interfacial tensions between liquid phases are the most common target properties used for validating coarse-grained models. In their seminal paper [23], Groot and Warren (GW) suggested a linear correlation between the DPD repulsion parameter a_{IJ} and the Flory-Huggins (FH) mismatch parameter χ_{IJ}. It was shown that the FH parameterization provides reasonable description of the interfacial tension between homopolymer melts. This method is convenient, since the FH parameters are available in the literature for many systems. However, the FH model for DPD parameterization is merely a *proxi*: one has to take into account the particular method used for defining χ_{IJ} parameters. In addition, it was shown that the LLE diagram predicted by the FH model qualitatively differs from the results of MC simulation of the DPD fluid [24].

The parameterization by Groot and Warren (GW) [23] has become a gold standard employed in most DPD simulations due to its simplicity and computational efficacy. Nevertheless, the formation of mesoscale interfaces is very sensitive to the variations in the chain local conformations affected by chain rigidity, relative volumes of coarse-grained chain fragments, and interactions between them, e.g. between heads and tails. These factors weren't taken into account in GW model, and thusly limit its applicability for quantitative description of self-assembly in surfactant and polymeric systems.

Several improvements have been done for refining the GW parameterization. Groot and Rabone [4] introduced different intracomponent parameters for different bead types to properly describe the properties of lipid bilayers. Backer et al. [26] introduce various masses for different species. Travis et al. [27] suggested determining both intra- and inter- component parameters from the cohesive energy density of individual components. The authors obtained a good agreement between calculated and experimental liquid-liquid phase diagrams for a mixture of two chemically similar liquids. Maitia and McGrother [28] derived correlations between χ, Δa and R_c. They concluded that Δa should increase proportionally to R_c. They suggested modified correlation between χ and Δa to account for this dependence on the bead diameter. χ values were obtained from the cohesive energy densities. The authors also stressed that mechanical equilibrium between liquid phases in important for proper parameterization. Spaeth et al. [29] introduced beads of different effective diameters. The mixtures of soft DPD spheres of different sizes were studied in depth by Kacar et al. [30] The parameters for DPD models of individual components were designed to produce the same pressure in pure liquids; the bead densities in different phases were allowed to differ. The authors obtained equation on state for mixtures of single-bead components and related to intercomponent DPD parameters to the Flory-Huggins parameters χ_{ij}. Liyana-Arachchi et al. [31] reported a detailed Monte Carlo study of ρ - P-T properties and structure of single component DPD fluids as well as the phase diagrams of symmetric ($a_{II} = a_{JJ}$) and asymmetric ($a_{II} \neq a_{JJ}$) binary mixtures. They suggested an equation of state for single-bead DPD mixtures that allowed facile fitting of the parameters to experimental LLE data. The properties of DPD models of polymer solutions were explored in MC simulations of Wijmans and Smit. [24] The mismatch parameters in these

papers are fitted to LLE phase diagrams of reference mixtures. The other target property for fitting DPD parameters is surface tension between liquid phases. The correlations between χ and Δa were first obtained by Groot and Warren and are often used in DPD simulations of polymers. [20, 32-33] Malti and McGrother [28] extended this approach to beads of different diameters. It is worth noting a limited availability of experimental data on surface tension. They are not as easy to calculate using the theoretical models compared to LLE diagrams.

Another important factor determining micelle size and shape is the rigidity of surfactant molecule. [34] Although the importance of rigidity is well recognized, its impact on micellization has not been studied systematically. Several studies explore the effect of chain rigidity on micelle shape. Based on the experimental observations, Heerklotz *et al.* [35] hypothesized that a spherical micelle must contain very few highly ordered/stretched surfactant chains to shape the micelle and also a considerable number of highly disordered chains to fill its hydrophobic core. Increased rigidity of the tail segment may favor the formation of rod-like micelles. Sterpone *et al.* [36] studied the correlation of interfacial packing of alkyl-polyethyleneglycole type surfactants with different flexibility of surfactant hydrophilic head segment using molecular dynamics simulations. They found that "hydrophilic head acts as an entropic reservoir for overcompensating the positive enthalpic variation at sphere-to-rod transition". Thus, increased flexibility of the head segment may favor rod-like micelles, similarly to effect of increased rigidity of the tail segment. Srinivasan and Blankschtein [37] looked into the role of rigidity in micellization by comparing the behavior of similar surfactants with alkyl and perfluoroalkyl tails. Fluorocarbons are effectively stiffer than hydrocarbons of similar molecular volume; the

authors observed that increased rigidity caused fluorinated surfactants form micelles of smaller curvature (that is, worm-like or bi-layer) under the solution conditions, at which non-fluorinated surfactants would form spherical aggregates. Similar discussion about the rigidity affecting the micelle shape for perfluoroalkyl sulfonamide ethoxylate $C_8F_{17}EO_{10}$ can be found in ref. [38]. Firetto el al. [39] used grand canonical Monte Carlo simulations to study the effect of chain rigidity on CMC and micelle size for the model surfactant composed of four head and tail groups, by changing the rigidity of the whole chain, and selectively of either hydrophobic or hydrophilc segment. CMC was found to decrease and N_{ag} to increase with the chain rigidity, which is consistent with the experimental observation on fluorinated surfactants [37]. In a recent paper, Lin *et al.* [22] studied self-assembly of various model polymeric surfactants using dissipative particle dynamics (DPD) simulations and observed a decline in CMC with the greater degree of the rigidity of the solvophobic or solvophilic blocks. N_{ag} grew with the rigidity but the shape of micelles remained approximately spherical. Warm-like micelles were observed in the concentrated solutions of rigid surfactants.

In addition to surfactant micellization, the other topic of interest in this these is modeling proton conductivity of polyelectrolyte membrane (PEM) implemented in PEM fuel cell. Hydrated polyelectrolyte for fuel cells typically consists of a hydrophobic organic backbone, to which strong acid groups are attached. Upon hydration (or solvation by other protonating compounds that are also used in PEM [40]), the acid groups dissociate, releasing protons and making the PEM proton-conductive. Because PEM have both hydrophobic and hydrophilic components, their structure is strongly non-uniform and may be very complex. Typically, a hydrated PEM segregates onto the hydrophilic subphase formed by

the acid groups, protons and polar solvents, and the hydrophobic subphase formed by the organic backbone. The hydrophilic subphase makes a network of clusters and channels through which water and protons diffuse. The morphology of the network is determined by the chemical structure of the polyelectrolyte and the hydration level. Thus, the proton transport through PEM is controlled by several phenomena that have very different characteristic spatial and temporal scales: (1) dissociation of the individual acid groups (2) proton transfer between solvent molecules and/or acid groups (3) overall segregation morphology of the hydrated PEM.

Due to the wide range of the scales determining water and proton transport in PEM, their modeling typically employs hybrid approaches, where different techniques are utilized to model the membrane segregation and water/proton diffusion on different levels. The segregation morphology, whose typical scale ranges from several to tens of nanometers is predicted by a mesoscale methods, such as thermodynamic [41-42] and self-consistent field theory, [43-44] Mesodyn, [45] coarse grained molecular dynamics (CG MD) [46-50] or DPD [8, 51-61]. Then, the diffusion of water and protons is considered in a static structure obtained from mesoscale modeling. Water and ion diffusion is typically considered in a pre-determined "ideal" environments such as cylindrical channels [62-63] and then the results can be extrapolated onto the structures obtained by mesoscale methods to predict the overall transport properties.

Because Nafion is the best-known PEM material, most simulation studies considered Nafion and other similar perfluorinated polyelectrolytes. The first DPD simulation of Nafion was conducted by Yamamoto et al. [8] The conservative repulsion parameters were estimated from the mixing energy calculations conducted with atomistic

modeling. The electrostatic interactions were implicitly mimicked by short-range forces. [8] The authors found irregular segregation morphologies, with reasonable correspondence to experimental results. They suggested that the proton conductivity may be estimated from water cluster connectivity in the structures obtained. [64] Later, Dorenbos et al [65], and Wu et al [58, 60] employed the same model for studies of nanostructure and water diffusion in several perfluorinated ionomers that differed by equivalent weight and sidechain length. Dorenbos et al [65] estimated water diffusion in the resulting DPD structures. The segregated structure was mapped onto a lattice; each lattice site belonged to either mobile (aqueous) or immobile (organic) subphase. Water self-diffusion coefficients were estimated using the random walks on the lattices obtained. The authors concluded that the same approach cannot be applied to proton conductivity, since a lattice replica of a nanosegregated structure does not carry any information on the local environment around any particular site, and therefore is unable to properly account for the interaction between protons and negatively charged sulfonate groups. Later, Dorenbos et al [66] used the models developed for bulk Nafion in simulations of the PEM in contact with carbon catalyst support.

Sawada et al [67] accounted for possible crosslinking of the perfluorinated skeleton chains and found that crosslinking leads to much smaller hydrophilic aggregates of only 1.8nm in diameter. Eliott et al [57] combined DPD results with experimental SAXS/SANS studies using a novel model-independent procedure. The modeling revealed a multi-level membrane organization, with hydrophilic – hydrophobic segregation on smaller scale and larger scale organization of the fluorocarbon backbone. This result is consistent with previous NMR studies. [68-69] Jorn and Voth [70] modeled the nanostructure of segregated polymer with standard short range DPD potentials, and then considered proton transport in

the structures obtained using smoothed particle hydrodynamics (SPH). [71] Transport coefficients and coarse-grained forces for the polymer backbone, side chain, proton, and water interactions were derived from MD simulations. The proton conductance profiles determined in this simulation at 40 nm scale are in semi-quantitative agreement with results of earlier experiments. [72-73] The authors also showed that accounting for the electrostatic interactions is crucial for the improvement of proton transport modeling with DPD.

DPD models with electrostatics considered implicitly were applied to other polyelectrolytes, such as sulfonated poly(phenylene) sulfone (sPSO2) at different sulfonation levels, [74] SPEEK [75], and grafted copolymers with varying type and the attachment of the side chain. [54] Explicit treatment of electrostatic interactions in DPD was enabled by the development of smeared charge models. In this approach, the charge is distributed around the bead center linear, [6] Slater-type exponential, [76] Gaussian-type, [77] and Bessel-type [78] distributions of charge density have been considered in the literature [78]. The charge distributions are isotropic and spherically symmetric. The charges interact in an isotropic medium of a uniform dielectric constant ε, although newly introduced polarizable models [79] enable more precise simulations at extra computational cost. The smeared charge approach was applied to hydrated Nafion [7] in the first explicit charge DPD simulation of PEM. The adsorption isotherms were calculated by Widom trial insertions of water beads into the Nafion structures generated by DPD, and the saturation hydration levels were identified for different equivalent polymer weights. Water diffusion was estimated from random walk in lattice replicas of the segregated polymer. The simulation results showed a good agreement with the experiment on potassium-substituted Nafion.

This succinct review shows that in published mesoscale studies of polyelectrolytes, dissociation/association of acid groups was considered indirectly. The degree of dissociation has to be essentially pre-assumed. For example, in the recent DPD simulations [7] of metal-substituted Nafion polymer at low water content, the dissociation degree was fixed and the respective fraction of the alkali metal counterions were considered as dissociated from their sulfonate groups and represented by hydrated counterion beads; the rest of the counterions were kept attached to the sidechains, and such pairs were modelled by neutral beads. Thus the dissociation degree [7] was determined by the coarse graining scheme rather than by chemical consideration. Alternatively, each dissociating group may be assigned a fractional charge according to a degree of dissociation calculated theoretically. This approach was employed in DPD simulations of α-synuclein that contains both carbonic acid and amine groups. [1] and in ionic diblock surfactants by Posel et al [80]. Both approaches share the same major drawback: the dissociation of a particular counterion is determined by the macroscopic properties such as hydration or pH. In reality the dissociation of a proton and its mobility are determined by local environment around it. Therefore, it is desirable that the dissociation is embedded directly into the mesoscale simulation forcefield.

The first main contribution of this thesis is the development of a systematic parameterization methodology based on a combination of top-down and bottom-up approaches. The methodology keeps intact the GW model assumptions of the equal bead size and equal intro-component repulsion potential and includes several steps: 1) – dissection of system compounds into equal size fragments, which correspond to reference compounds, and choice of the bead size that determines the level of coarse-graining, 2) –

determination of the intra-component repulsion parameter from the density and compressibility of the solvent at given coarse-graining level, 3) – determination of the bond potentials between same type beads from the fitting to atomistic MD simulations of conformations of respective homo-oligomers, 4) determination of inter-component (mismatch) parameters from the fitting of IDAC in binary solutions of reference compounds to the results of MC simulations of respective DPD fluids, 5) determination of inter-component (mismatch) parameters from the fitting the activity in aqueous solution of respective reference compound oligomers, 6) determination of head-tail repulsion and bond parameters and verification of the overall set of parameters against atomistic MD simulations of molecule conformations. This approach was shown to be efficient in studies of micellization of selected non-ionic surfactants [81] and was extended to modeling ionic surfactants [82] and polymer brushes in organic solvents. [83] The flexibility of the method is examined on a nonionic surfactant polyethylene oxide alkyl ether (C_nE_m) of different composition. A molecule of C_nE_m surfactant consists of n hydrophobic alkyl monomers (CH_3 or CH_2) and m hydrophilic oxyethylene units (CH_2OCH_2). By varying the chain composition and comparing the simulation results with experimental data on critical micelle concentration (CMC) and aggregation number (N_{ag}), we demonstrate and verify the robustness of the proposed methodology.

This parameterization method certainly improve the performance of DPD in modeling self-assembly of surfactant and polymer solution, however, segregation in polyelectrolytes is especially challenging, as it involves redistribution of charged species far beyond the molecular scale. The dissociation of a particular counterion is determined by the local environment around it rather than by macroscopic properties such as pH. It is

therefore desirable that the dissociation is embedded directly into the simulation forcefield. In published DPD studies of polyelectrolytes, dissociation/association of counterions was considered indirectly. The second class of problems that may require explicit consideration of dissociating ions is related to their transport in complex geometries, such as proton exchange ionomers of which Nafion is the best-known example. The mechanisms of proton mobility in such environments include the Grotthuss-type "hopping" that involves formation of various proton-water complexes like hydronium H_3O^+, Zundel $H_5O_2^+$, and Eigen $H_9O_4^+$ ions, as well as proton-water-sulfonate complexes. In the literature, the hopping mechanisms were accounted for in an indirect manner.

The second main contribution of this thesis is the development of a new mesoscale simulation framework that directly incorporates dissociation-association of proton-base complexes into the DPD forcefield. We specifically address the proton mobility in the water and protonation equilibria in the solution of acids by artificially mimicking Grotthuss-type mechanisms of formation and breakup of the proton-water and proton-anion (such as deprotonated acid) complexes. The proton is introduced as a separate charged bead that forms dissociable bonds with proton receptive base beads, such as water or deprotonated acid anions. The proton-base bonds are described by Morse potentials. When the proton established Morse bonds with two bases, they form an intermediate complex, and the proton is able to "hop" between the bases artificially mimicking the Grotthuss diffusion mechanism. The interaction of model proton with different bases and formation of the proton-base complexes are controlled by the Morse potential. The model provides quantitative agreement with experiments for the proton

self-diffusion coefficient and hopping frequency, as well as for the degree of dissociation of benzenesulfonic acid.

The developed proton model is then applied to DPD simulation for proton diffusion in a hydrated polyelectrolye, and sulfonated polystyrene (sPS) is chosen as a characteristic example. sPS is a polymer of a significant practical importance, since various sPS based materials (especially block copolymers of sPS and polyolefins) are used in proton exchange fuel cells; their industrial potential is propped by a low cost, as they are generally cheaper that perfluorinated PEM of Nafion type. In sPS-polyolefin block copolymers, water-swollen sPS forms the hydrophilic domain. But the hydrophilic domain itself is segregated onto the aqueous subphase formed by the sulfonic acid groups surrounded by water and protons and the hydrophobic alkylbenzene subphase. The segregation inside hydrated sPS was observed both experimentally and in simulations. [84-86] The morphology is irregular and depends on the level of sulfonation, and the scale of segregation is believed to be relatively small. Small size of the hydrophilic channels, tangible dissociation constant of the acid group, and the ability to vary the sulfonation level substantially, make sPS an ideal system for examining the advantages and limitations of our DPD approach. The simulation results semi-quantitatively predict nanoscale segregation of the hydrated sPS in to hydrophobic and hydrophilic subphases, water self-diffusion and proton connectivity. As hydration increases, the hydrophilic subphase shows a classical transition from a collection of isolated water clusters to a percolated network. The analysis of connectivity and water diffusion demonstrates the importance of dynamic percolation via formation and breakup of temporary junctions between water aggregates. The new DPD approach qualitatively

predicts the ratio of proton to water self-diffusion and its dependence on hydration. The proton conductivity reasonably agrees with experiments.

This thesis is instructed as follows. In Section 2, the general form of DPD force field is reviewed, based on the Groot and Warren formulism and the modification in this thesis. In Section 3, the top-down approach in obtaining repulsion parameters for chain molecule is introduced. The correlation between DPD repulsion parameter and thermodynamics activity coefficient is derived and constructed. Three different nonionic surfactants are studied where the chain rigidity is applied through harmonic bonds. The predicted micellar properties have superb agreements with experimental data. In Section 4, the importance of the chain rigidity is discussed. The interplay of strength of rigidity and of repulsion parameter is examined by modeling the micellization of nonionic surfactant C_8E_8 and MEGA-10. It reveals that the bond and rigidity coefficients need to be precisely determined together with the determination of the repulsion parameter in order to reproduce the correct equilibrium morphology of micellization. In order to improve the force field related to the chain configuration, a bottom-up approach is introduced in Section 5. The bond and rigidity of DPD models are surgically determined by matching the conformations of the chain molecules in the atomistic scale and based on the coarse grained size of DPD. Repulsion parameters are also determined based on the obtained bond conformation and bead size, correspondingly. The scheme is examined by reproducing the micellar properties of CE surfactant with a variety of tail and head ratio, showing the approach is robust in the applicable range. In order to apply the parameterization to modeling proton transfer in PEM, an advanced DPD proton model is introduced in Section 6. The new proton model reproduces the proton dynamics in the bulk water as well as the

dissociation equilibrium of proton from the acidic sites of the PEM fragments. The proton model is applied to study the sulfonate polystyrene in Section 7, equilibrium morphologies and the dynamics properties of sPS are studied compared to previous atomistic simulation and available experiments. The thesis is concluded in Section 8.

Section 2. Force field of DPD

The system under consideration is presented as multicomponent mixture of beads with equal effective diameter R_C. The system dynamics and equilibrium are studied by solving Newton equations of motions with pair-wise inter-bead forces given in Eq.1.

$$\begin{aligned}\mathbf{F}_{ij}(\mathbf{r}_{ij}) &= \mathbf{F}_{ij}^{(\mathrm{B})}(\mathbf{r}_{ij}) + \mathbf{F}_{ij}^{(\mathrm{A})}(\theta_{ij}) \\ &+ \mathbf{F}_{ij}^{(\mathrm{C})}(\mathbf{r}_{ij}) + \mathbf{F}_{ij}^{(\mathrm{D})}(\mathbf{r}_{ij}, \mathbf{v}_{ij}) + \mathbf{F}_{ij}^{(\mathrm{R})}(\mathbf{r}_{ij}) + \mathbf{F}_{ij}^{(\mathrm{E})}(\mathbf{r}_{ij}) + \mathbf{F}_{ij}^{(\mathrm{M})}(\mathbf{r}_{ij})\end{aligned} \tag{2-1}$$

The details of each force in eq. 2-1 is introduced as follows:

(1) $\mathbf{F}_{ij}^{(\mathrm{B})}$ and $\mathbf{F}_{ij}^{(\mathrm{A})}$ are intra-molecule bond and angle interactions in charge of chain conformations. In this thesis, we use harmonic bond and FENE bond for bonds between neighbor beads (1-2 bonds) and between second neighbor beads (1-3 bonds), that $\mathbf{F}_{ij}^{(\mathbf{B})}(\mathbf{r}_{ij}) = K_b\left(r_{ij} - r_0\right)\dfrac{\mathbf{r}_{ij}}{r_{ij}}$ for harmonic bonds, and $\mathbf{F}_{ij}^{(\mathrm{B})}(\mathbf{r}_{ij})$= $K_\mathrm{b}(r_0 - r_\mathrm{ij})/(1 - ((r_\mathrm{ij} - r_0)^2/r_\mathrm{m}^2))\mathbf{r}_{ij}/r_{ij}$ for FENE bonds. K_b is bond rigidity, r_0 is the equilibrium bond length, and r_m is the maximum bond length. In Section 7 of modeling polyelectrolyte membrane, the polymer is relatively complex (compared to linear chains we considered earlier) and contains very rigid fragments, we also introduced standard harmonic angle potentials between certain pairs of nearest neighbor bonds that $\mathbf{F}_{ij}^{(\mathrm{A})}(\theta_{ikj}) = K_\theta\left(\theta_0 - \theta_{ikj}\right)$. Assuming the bead *i* and *j* are separated by another bead *k*, θ_{ikj} refers to the angle between vectors *ik* and ,*jk* and θ_0 and K_θ are the equilibrium angle and stiffness.

(2) $\mathbf{F}_{ij}^{(\mathrm{C})}$ is the conservative force for bead repulsion. It acts only on the overlapped beads that $\mathbf{F}_{ij}^{(\mathrm{C})}(\mathbf{r}_{ij}) = a_\mathrm{IJ}\, w\left(r_{ij}\right)\mathbf{r}_{ij}/r_{ij}$. The weighting factor w indicates the degree of bead

overlapping that $w(r_{ij}) = 1 - r_{ij}/R_C$ for $r_{ij} < R_C$ and $w(r_{ij}) = 0$ for $r_{ij} \geq R_C$. The magnitude of repulsive force is characterized by the repulsion parameter a_{IJ} specific to the given bead pair of types I and J. The intra-component repulsion parameters between beads of the same type are set equal irrespective to the bead type (i.e. $a_{JJ} = a_{II}$). The determination of intra- and inter- component repulsion parameters will be discussed in the following sections.

(2) The random force $\mathbf{F}_{ij}^{(R)}$ and drag force $\mathbf{F}_{ij}^{(D)}$ institute the Langevin thermostat; they act also between the overlapping beads along the line connecting the bead centers. The drag force is velocity-dependent: $\mathbf{F}_{ij}^{(D)}(\mathbf{r}_{ij}, \mathbf{v}_{ij}) = -\gamma w(r_{ij})^2 (\mathbf{r}_{ij} * \mathbf{v}_{ij})$, where $\mathbf{v}_{ij} = \mathbf{v}_j - \mathbf{v}_i$; $\mathbf{v}_i$ and $\mathbf{v}_j$ are the current velocities of the particles. The random force $\mathbf{F}_{ij}^{(R)}$ that accounts for thermal fluctuations, is taken proportional to the conservative force: $\mathbf{F}_{ij}^{(R)}(\mathbf{r}_{ij}) = \sigma w(r_{ij}) r_{ij} \theta_{ij}(t) \mathbf{r}_{ij}/r_{ij}$, where $\theta_{ij}(t)$ is a randomly fluctuating in time variable with Gaussian statistics. The fluctuation-dissipation relationship couples the noise level σ and friction factor γ that $\sigma^2 = 2\gamma kT$. [87] The parameters is set as $\gamma = 4.5$, a suggested value for a better simulation temperature control. [23]

(3) The electrostatic interactions $\mathbf{F}_{ij}^{(E)}$ are modeled using the smeared charge approach with the Slater-type charge density distribution with an exponential decay, [76] $f(r) = \frac{q}{\pi\lambda^3} \exp\left(-\frac{2r}{\lambda}\right)$, where λ is the effective smearing radius. The electrostatic force $\mathbf{F}_{ij}^{(E)}$ between charged particles *i* and *j* in eq. 2-1 is expressed as

$$\mathbf{F}_{ij}^{(\mathrm{E})}(\mathbf{r}_{ij}) = \frac{e^2 q_i q_j}{4\pi k T \varepsilon_0 \varepsilon_r R_{\mathrm{C}} r_{ij}^2}\left[1-\exp\left(-2R_{\mathrm{C}} r_{ij}/\lambda r_{ij}\right)\left(1+2R_{\mathrm{C}} r_{ij}/\lambda\left(1+R_{\mathrm{C}} r_{ij}/\lambda\right)\right)\right]\frac{\mathbf{r}_{ij}}{r_{ij}} \qquad (2\text{-}2)$$

At long range, the electrostatic interaction of smeared charges (Eq. 2-2) reduces to the Coulomb potential. The standard Ewald summation [88] is used to account for long-range electrostatics. The choice of the smearing radius $\lambda = 0.25R_{\mathrm{c}}$ for all charged beads was made on technical reasons (Supporting Information of ref [89], Section S2). Similar suggestions can be found in recent DPD studies. [78, 80, 90].

(4) The last term $\mathbf{F}_{ij}^{(\mathrm{M})}(\mathbf{r}_{ij})$ in Eq.2-1 models the forces only between proton bead P and proton receptive beads such as water bead W or sulfonic bead S in benzenesulfonic acid (Section6) or sPS side chain (Section 7). The P—base interactions are modelled by the Morse potential, cut and shifted at cutoff radius r^{M}:

$$\mathbf{F}_{ij}^{(\mathrm{M})}(\mathbf{r}_{ij}) = -2\alpha_{\mathrm{IJ}} K_{\mathrm{IJ}} \exp\left[\alpha_{\mathrm{IJ}}\left(r_{ij}-r_{ij}^0\right)\right]\left\{1-\exp\left[\alpha_{\mathrm{PB}}\left(r_{ij}-r_{ij}^0\right)\right]\right\}\mathbf{r}_{ij}/r_{ij} \text{ , at } r_{ij} < r_{ij}^{\mathrm{M}} \qquad (2\text{-}3)$$

The Morse potential has a minimum at $r_{ij} = r_{ij}^0$ and is characterized by the strength parameter K_{IJ} and effective steepness α_{IJ}. $\mathbf{F}_{ij}^{(\mathrm{M})}$ applies to interactions of P beads with bases (S and W beads). That is, a P bead connected to a single S bead by Morse potential, forms a neutral acid. Formation of a new Morse bond between the same P and another base (say, a W bead) leads to a formation of an intermediate complex. A P-base pair dissociates when r_{PS} exceeds r^{M}, leading to a breakup of the complex. If the Morse pair that dissociates is the original P-S pair, the entire process describes dissociation of the acid in water. In ref [89] we show how through the sequence of formations and breakup of Morse bonds P beads can "hop" between the bases (here sulfonates S and waters W), artificially mimicking the

Grotthius [89] mechanism of proton diffusion. The process of P bead transfer between the bases is associated with a potential barrier, similarly to actual acts of proton transfer in aqueous solutions. By adjusting the depth and steepness of the Morse potential, we were able to reproduce both proton mobility in bulk water and the dissociation equilibrium of the acid. The details will be discussed in Section 6, and the forcefield is implemented in the DL_MESO DPD package. [91]

Section 3. Parameterization for repulsion parameters

In this section, we suggest a new approach to parameterizing the soft-core interactions and demonstrate that the classical DPD scheme with repulsion potentials (1) between the beads of the same size R_c is capable of quantitative predicting micellization in non-ionic surfactant solutions. We studied three typical examples of surfactant molecules of different chemical structures with experimentally known CMC and N_{ag} values. These examples were chosen to represent different classes of non-ionic and zwitter-ionic surfactants of suitable molecule size and structure that could be handled with modest computational resources: (1) Octaethylene glycol monooctyl ether C_8E_8, made of hydrophobic octyl tail and hydrophilic oxyethylene head; (2) dodecyldimethylamine oxide (DDAO), whose hydrophilic segment is zwitter-ionic aminoxide group treated as nonionic for short distance between the charged atoms; (3) n-Decanoyl-N-methyl-D-glucamide (MEGA-10), also composed of alkyl tail and amide middle segments, and glycol hydrophilic segments.

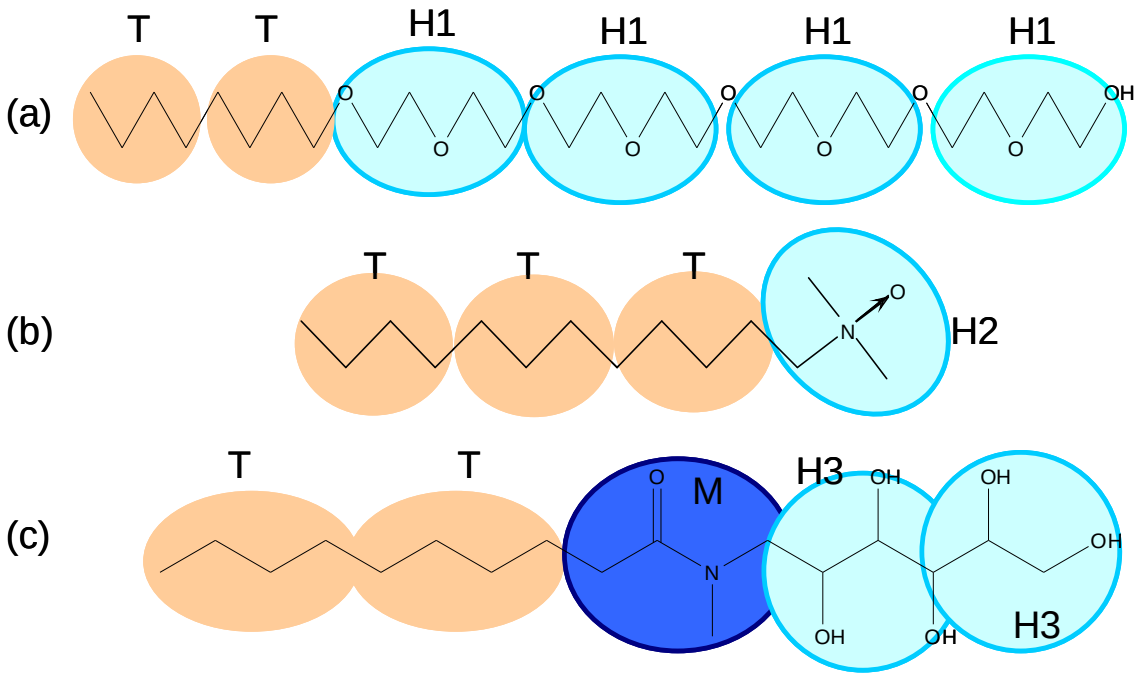

Figure 3-1. Schematics of coarse-graining. (a) C_8E_8 (Octaethylene glycol monooctyl ether $nC_8H_{17}(OCH_2CH_2)_8OH$; coarse-grained model TT-H1H1H1H1); (b) DDAO (Dodecyldimethylamineoxide $nC_{12}H_{25}NO(CH_3)_2$, coarse-grained model TTT-H2); (c) MEGA-10 (N-Decanoyl-N-methylglucamine $nC_9H_{19}(NCH_3)(HCOH)4CH_2OH$, coarse-grained model TT-MH3H3).

The coarse-grained models of the surfactant molecules are presented in Figure 3-1 and Table 3-1. The surfactants were dissected into the tail, head, and middle beads of approximately same size. The volumes of different fragments were estimated from the masses and densities of reference compounds: n-octane, triglyme, N-methyl acetamide, ethyleneglycole, and water. For CE surfactant, we followed the dissection by Groot [32]. Because the tails in all three surfactants are alkyl chains of length in multiples of four, the tail T-bead contained four carbon atoms approximately representing the butyl group, C_4H_9. The water W-bead was chosen to contain n_W=4 molecules. This choice is consistent with ref [4], where the T-bead volume was evaluated from experimental scattering volumes of

water and dodecane [92]; roughly one CH_2 group in T-bead corresponds to one water molecule in W-bead.

Table 3-1. Coarse-grained models of surfactants, reference compounds, and DPD repulsive parameters (a_{ij}).

Bead type	Reference compound	Model compound	Repulsion parameter, kT/R^2_c
W	4 H_2O	monomer W	a_{WW} =a_{II}=106.5
T	$CH_3(CH_2)_6CH_3$	dimer TT	Δa_{TW}=19.6
H_1 in C8E8	$CH_3OCH_2CH_2OCH_3$	dimer H_1H_1	Δa_{H1W}=1.0; Δa_{TH1}=6.5
H_2 in DDAO	$CH_3N(O)(CH_3)_2$	dimer H_2	Δa_{H2W}=-23.5; Δa_{TH2}=6.2
H_3 in MEGA-10	$OHCH_2(CHOH)_3CH_2OH$	dimer H_3H_3	Δa_{H3W}=1.0; Δa_{TH3}=9.8
M in MEGA-10	$CH_3CON(CH_3)_2$	monomer M	Δa_{MW}=3.0; Δa_{H3M}=3.0; Δa_{TM}=3.6

Following ref [4], the reduced density ρ^* of DPD beads (the average number of bead centers in $1R_c^3$) was set to ρ^*=3, which corresponds to the bead size of R_c = 7.1Å. For the sake of simplicity, we followed the conventional implementation [4] and assumed that the

self-repulsion parameter a_{II} and size $R_{c,I}$ for all types of beads are the same and equal to those of W-beads; $a_{II} = a_{WW}$ and $R_{c,I} = R_c$. The self-repulsion conservative parameter $a_{WW}=106.5kT/R_c$ was determined from the water compressibility as in ref [93]. This value is in reasonable agreement with published data.[23] Note that the W-bead self-repulsion parameter a_{WW} represents the starting point for parameterization of other coarse-grained components.

Assigning the binary repulsion parameters a_{IJ} for beads of different types is the most critical step in the parameterization procedure. Here, we suggest defining a_{IJ} values from the best match of the infinite dilution activity coefficients γ_∞ of binary solutions of A and B model particles composed of I and J type beads calculated within the adopted DPD model to the experimental or *ab initio* computed γ_∞ values of the solutions formed by the reference compounds, which correspond to the coarse-grained beads. The A and B components of these binary solutions may represent either monomers or dimers of coarse-grained beads. In particular, a convenient choice is to select A=I or A=I_2, and B=J or B=J_2, depending on the availability of reference data needed for the parameter fitting. Infinite dilution activity coefficients are standard properties of binary solutions, with the vast body of data available in the literature, as they are measured with well-established methods such as headspace technology.

For model binary solutions, γ_∞ are calculated with the Widom insertion MC technique [94] that is especially efficient for soft particle systems,

$$\lg(\gamma_\infty) = \ln\left\langle \exp\left(-E_{AB}^{ins}/kT\right)\right\rangle_{NVT} - \ln\left\langle \exp\left(-E_{AA}^{ins}/kT\right)\right\rangle_{NVT} - \ln n_B b_A / n_A b_B \qquad (3\text{-}1)$$

Here, E_{AB}^{ins} is the energy of random insertion of A molecule into bath of B molecules simulated in the canonical ensemble, E_{AA}^{ins} is the energy of insertion of A particle in the bath of A particles, and $b_{A/B}$ is the number of beads in A or B particles (b =1 for monomers and b =2 for dimers). Eq. 3-1 is derived in Supporting Information of ref [1]. Note that in Eq. 3-1, only E_{AB}^{ins} term depends on a_{IJ}.

The strategy of assigning of a_{IJ} is the following. First, we construct in MC simulations the calibration $\gamma_\infty(a_{IJ})$ dependencies, which are unique for monomer-monomer, monomer-dimer, and dimer-dimer solutions. The respective calibration curves are presented in Figure 3-2. Because γ_∞ has a relatively weak dependence on the self-repulsion parameter, it is determined by the mismatch parameter $\Delta a_{IJ} = a_{IJ} - a_{II}$, which is correlated almost linearly with $\lg(\gamma_\infty)$ that is convenient for fitting (see Supporting Information of ref [1]). Then, interpolating experimental γ_∞ onto the respective reference curve, a_{IJ} is obtained for the particular bead pair.

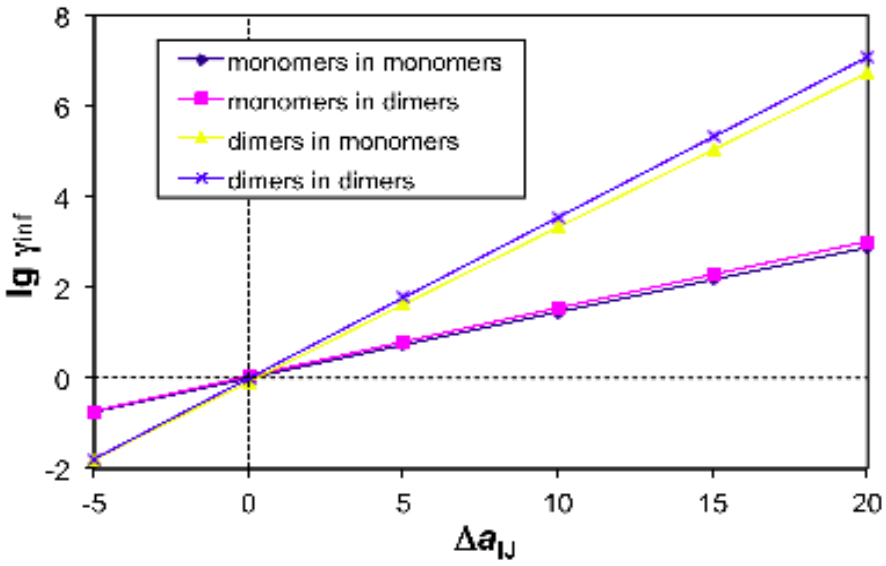

Figure 3-2. Calibration correlations between infinite dilution activity γ_∞ and mismatch DPD parameter Δa_{IJ} for binary solutions formed by monomeric coarse-grained compound and their dimers at $R_c = 7.1$

The repulsion parameter a_{TW} between T- and W-beads was determined as following. The most natural choice of the reference compound for the T-bead would be butane. However, butane is a vapor at ambient conditions, and the DPD model is not suitable for the simulating of vapor-liquid equilibrium. Therefore, we chose octane as the reference compound for the T-beads. We present octane, which has the volume of approximately 8 water molecules or two T-beads, as T_2 *dimer*. The T—T bond length is chosen at $0.8R_c$, which is consistent with both the octane molecular structure and the DPD fluid density of $\rho^*=3$, since the distance between neighboring beads in BCC lattice at this density is close to $0.8R_c$. The value of $a_{TW} = a_{WW} + \Delta a_{TW}$ is estimated from the experimental value of γ_∞ using the monomer-dimer and dimer–monomer reference curves from Fig. 2. Because water and octane are almost completely immiscible, γ_∞ is obtained from the

solubility of octane in water, as $\gamma_\infty = 1 / x_{LLE}$, where x_{LLE} is the octane molar fraction at liquid-liquid equilibrium. Using experimental data from ref [95], we obtained $\Delta a_{TW} = 18.7$ kT/R_c^2, or $a_{TW} = 125.2$ kT/R_c^2. Similarly, from water solubility in octane we obtain $\Delta a_{TW}=20.6$ kT/R_c^2 , which is close to the first value, as well as to the parameter obtained from Flory-Huggins using $\Delta a = \chi/0.293$ correlation suggested by Wijmans et al [24].

In a similar fashion, we chose the reference compounds for the other coarse-grained fragments of the surfactants given in Table 3-1 and calculated a_{IJ} for all bead pairs using the similar algorithm from monomer-monomer or dimer-dimer reference curves from Fig. 2 in accord to the respective reference compounds. The experimental data for the reference compounds of some bead pairs was not found. In this case, we calculated γ_∞ using COSMO-RS model [96] with COSMOtherm software [97]. However, these calculations did not always lead to plausible results. For example, diglyme, the reference head bead of C_8E_8, modeled as H1H1 dimer is miscible with water [98], which means that a_{H1W} should be close to a_{WW}. Unable to find the experimental value of γ_∞, we performed COSMO-RS calculations and found that the calculated value of γ_∞ depended heavily on the conformer and showed relatively hydrophobic solvation with $\lg(\gamma^\infty)$ varying from 0.95 to 2.6. This implies, in conflict with experiments, that diglyme would be miscible with octane rather than with water. As a reasonable compromise, we assigned a_{H1W} from the Flory mismatch parameter $\chi_{H1W} = 0.3$ reported by Saeki et al. [99].

Rigidity of surfactant molecules substantially influences the CMC, especially for long molecules. In this work, we maintained molecule rigidity by using 1-3 secondary harmonic bonds that connected beads separated by 2 primary bonds, and the length equals

to the sums of the length of the beads. From MD simulations of hexadecane at 298K and 1atm performed with TraPPE forcefield [100], we assumed bond length proportional to the number of covalent bonds between the neighboring beads of the chain, and rigidity inverse proportional to the number of flexible angles. As a result, the rigidity $K_{1\text{-}2}$ of 1-2 and 1-3 bonds was calculated as $320/n_t$ where n_t is the number of n_t is the number of flexible torsion angles between the bead centers. In a homopolymer chain, 1-2 bonds are twice as rigid as 1-3 bonds. The validity of this assumption is confirmed by the distributions of the interbead distances calculated using the atomistic MD and DPD simulations. The effects of rigidity on CMC and other experimentally verifiable quantitative characteristics of surfactants have, to our knowledge, never been systematically studied and call for a detailed separate work that is beyond the scope of this note.

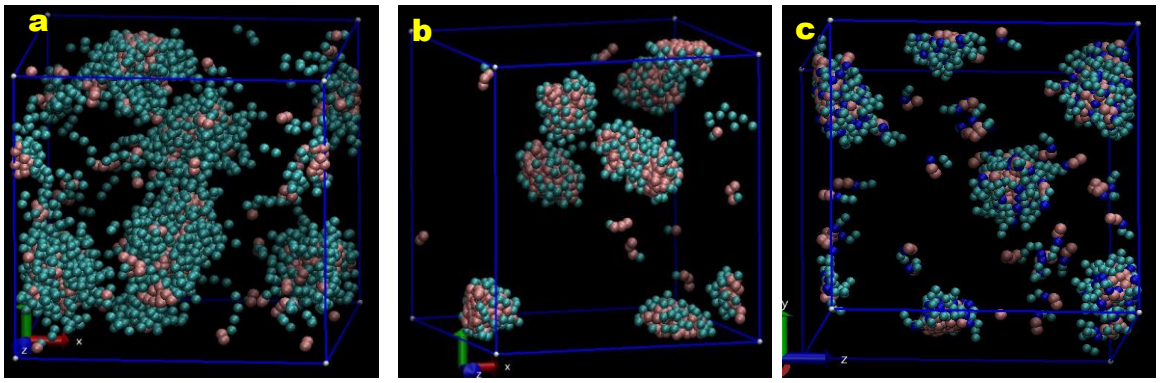

Figure 3-3. Snapshots of equilibrated DPD configurations for surfactant (a) C8E8 (model: TTHHHH) at φ_S =0.04, (b) DDAO (model: TTTH) at φ_S =0.02, and (c) MEGA-10 (model: TTMHH) at φ_S =0.04 in water. Bead colors: cyan-head H-bead, pink-tail T-bead, and blue-middle M-bead (in MEGA-10).

Using the models and techniques described above and the model parameters from Table 3-1, CMC and N_{ag} were calculated and compared with available experimental data.

DPD simulations were performed with the original algorithm based on the work of Pagonabarraga et al. [101] and are described in Supporting Information of ref [1]. CMC was obtained from the recorded simulation trajectories as follows. Two surfactant molecules were assumed to belong to the same aggregate if any two of their tail or middle beads overlapped. If an aggregate contained more than a certain threshold n_{mic} of surfactant molecules, it was counted as a micelle; if a surfactant molecule belonged to a cluster containing less than n_{mono} surfactant molecules, it was assumed to belong to the aqueous solution of monomers in equilibrium with the micelles. The concentration of "monomeric" surfactant in water was treated as the CMC. Aggregation was considered as complete and equilibrium reached when the CMC and micelle numbers stabilized and became practically insensitive to the choice of n_{mono} and n_{mic} within reasonable limits. In the "production" calculations, we used n_{mic}=15 and n_{mono}=5. In Figure 3-3, we present typical snapshots of the equilibrated micellar systems. The CMC was calculated from the ratio of the number of "free" monomers n_{free} (that included surfactants in all aggregates smaller than n_{mono}) to the number of water beads, and converted into mmol/L as $M_{CMC}= n_{free}/(N_A n_W n_{H2O} R_c^3)$, where n_{H2O} is the number of water beads in the box. In the Supporting Information of ref [1], we present the dependence of the aggregation number on the values of n_{mono} and n_{mic} used for the micelle and cluster definitions for MEGA-10 system.

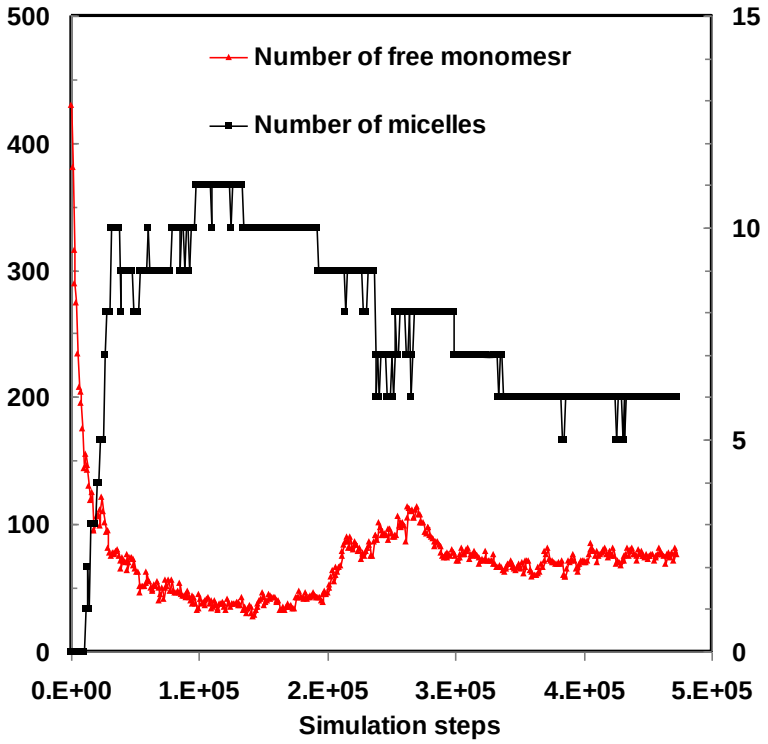

Figure 3-4. Evolution of number of free monomers (left vertical axes) and number of micelles (secondary vertical axes) in solution of surfactant C_8E_8 at concentration $\varphi_S = 0.04$. After $3.4*10^5$ steps, the number of micelle is fluctuating from 5 to 6; the number of free monomer is fluctuating at averaged 72 with absolute variance equals to 5. Each dot represents one trajectory saved each 1000 simulation steps.

Possible dependence of M_{CMC} on the system size and the total surfactant load was carefully checked. For C_8E_8 system, we performed a series of simulations at three surfactant volume fractions φ_s=0.02, 0.04, and 0.06. Even though the aggregation number increased drastically because of micelle merging (see Table 3-1, and snapshots in Supporting Information or ref [1]), we observed very low fluctuations and no evident trend for the calculated M_{CMC}. The evolution of the number of micelles in C_8E_8 system at φ_s=0.04 is shown in Figure 3-4. The averaged CMC 11.8 ± 0.4mmol/L is in quantitative agreement with experimental value 10. [102] The aggregation number 63 at φ_s=0.04 and 83 at φ_s=0.06

also agree with experimental value 72 [103] at φ_s=0.05 and the same temperature. Good agreement with the experiment was also obtained for DDAO, where the calculated CMC of 1.3 mmol/L fell within the experimental range of 1~2 mmol/L [104], and the N_{AG} coincided with the experiment nearly exactly (77 versus 76). For MEGA-10, the calculated CMC is 7.5 mmol/L, which is close to the experimental value of 6~7 mmol/L [105] .

In conclusions, we suggested a straightforward methodology for obtaining conservative soft repulsion parameters for DPD simulations of surfactant solutions formed by relatively small molecules. The main idea of the proposed parameterization method is fitting to the experimental data on infinite dilution coefficients of reference compounds composed of coarse-grained fragments of the molecule under consideration. In most cases such data is available from the literature, or can be obtained in routine experiments. When experimental γ^{∞} are unavailable, we used thermodynamic models (in this work, we select COSMO-RS, but other approaches such as group-contribution models are also available). These models have to be applied cautiously, as this work shows. Widening the scope of experimental data to which DPD parameters can be fitted is highly desirable. For example, water-octanol and water-hexane partitioning coefficients are widely used for environmental purposes, are available for many compounds and characterize their relative hydrophobicity. However, utilization of this data is belong the scope of this letter.

We tested our approach against CMC and mean aggregation number of several non-ionic surfactants of different chemistry and obtained quantitative agreement with experiments. Although the methodology described here is limited by the assumptions of equal bead size and equal self-repulsion parameters, the presented examples show its potential for modeling complex micellar systems in a computationally efficient manner.

Further development of the proposed parameterization method should involve: extension to multicomponent solutions of course-grained particles with the fractional numbers of groups per beads [5] and beads of different sizes [28] in order to account for unequal volumes of reference compounds available from, e.g., Bondi tables; extension to ionic surfactants by incorporation of electrostatic interactions with dissolvable counter-ions as was suggested in ref [6]; independent determination of self-repulsion parameters from the compressibility of reference pure liquids in a similar way as it is done for water. Also, the proposed method is not limited to surfactants, it can be adopted for coarse-grained modeling of self-assembly, rheological, and transport properties of other complex fluid and soft matter systems.

Section 4. The role of chain rigidity

In this section, we examine the effect of molecule rigidity on the self-assembly of linear non-ionic surfactants using conventional DPD simulations with the standard soft-core repulsion potentials. Chain rigidity is controlled using the second neighbor ("1-3") harmonic bonds.[1] Several simulations with the angle potential are performed for comparison. We focus on quantitative characterization of the most basic properties of dilute surfactant solutions: CMC, N_{ag}, and micelle shape.

We consider two surfactants from our previous study [1]: octaethylene glycol monooctyl ether (C_8E_8) and n-decanoyl-N-methyl-D-glucamide (MEGA-10). Both molecules are relatively small, with molecular weights of 350 and 482 g/mol, respectively, and were modeled as linear chains of 6 (C_8E_8) and 5 (MEGA-10) soft beads connected by standard harmonic nearest neighbor bonds. Thus, each bead represented only 4-5 heavy atoms and was substantially smaller than the persistence length. The coarse-grained models of the surfactant molecules and repulsive parameters are presented in Figure 4-1 and Table 4-1. The surfactants were dissected into the tail T, head H, and middle M beads of the same size as the water bead W represented $n_W = 4$ water molecules.

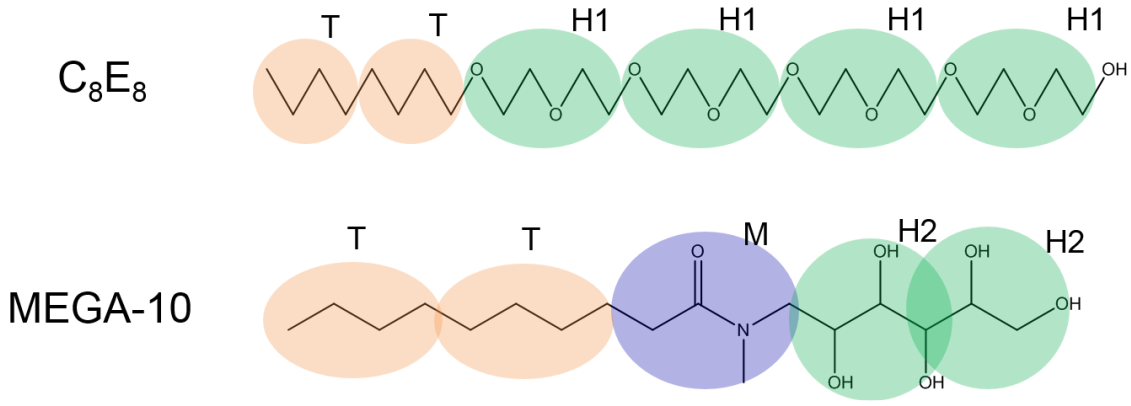

Figure 4-1. Schematic of coarse-grained surfactant models. C_8E_8 (octaethylene glycol monooctyl ether n-$C_8H_{17}(OCH_2CH_2)_8OH$) is presented as the chain of 2 tail and 4 head beads, TT-H1H1H1H1. MEGA-10 (*n*-decanoyl-N-methylglucamine, n-$C_9H_{19}(NCH_3)(HCOH)_4CH_2OH$) is modeled as a linear chain of 2 tail beads, 1 middle bead, and 2 head beads, TT-M-H2H2).

We used the most common formulation of the method: the reduced density ρ^* of DPD beads (the average number of bead centers in 1 R_c^3) was set to $\rho^* = 3$, all beads had the same effective diameter R_c = 7.1 Å, and the self-repulsion parameter a_{II} was equal to a_{WW}=106.5 k_BT/R_c for all bead types, as determined from the water compressibility as in ref. [93] Conservative repulsion parameters between beads that belong to different types were determined from best fit to the infinite dilution activity coefficients of binary solutions formed by reference compounds that represent coarse-grained fragments of surfactant molecules, as described in ref. [1] Parameter γ that determines the level of energy fluctuation and dissipation governed by random and drag forces, was set to 1.5. Note that dynamic properties of micellar systems are not targeted in this work.

Table 4-1 lists the equations and parameters that define surfactant rigidity. Neighboring beads are connected by harmonic bonds, the choice of equilibrium bond length and bond stiffness is described in ref. [1] The rigidity of the coarse-grained surfactant molecule was controlled by imposing either the harmonic potential between the second neighbor beads, or the harmonic angle potential between the nearest neighbor bonds, Figure 4-2. In the first method, each pair of beads that has a common neighbor was connected by a "second neighbor" harmonic bond whose equilibrium length was equal to the sum of the equilibrium lengths of the bonds to the common neighbor. For example, for a sequence of beads L-M-N, $r_e^{(LN)} = r_e^{(MN)} + r_e^{(LM)}$, $E^{LN} = K_{1\text{-}3}(r^{(LN)} - r_e^{(LN)})^2$. In the second

method, the neighboring bonds were bound by a harmonic angle potential $E^{LMN} = K(\theta^{LMN} - \theta_e^{LMN})^2$. In both cases, the straight conformation corresponds to the minimum of potential energy. Compared to both harmonic [22] and cosine [39] angle rigidity potential, the second neighbor bond potential is less stiff when $\theta \cong \pi$, but imposes a higher penalty at low angles ($\theta \cong 0$) (Figure 4-2). Although the harmonic angle potential is more conventional, we have to note that the rigidity potentials of coarse-grained molecules reflect torsional flexibility and 1-3 bonds may describe this flexibility more accurately than harmonic angles and cosine formula. Noteworthy, with such introduced second neighbor 1-3 bond potentials, we obtained [1] quantitative agreement with the experimental CMC and N_{ag} for C_8E_8 and MEGA-10 (at $K_{1\text{-}3} = 20\ k_BT/R_c^2$) surfactants considered in this work.

Table 4-1. Coarse-grained model of molecules, reference compounds, and DPD repulsive parameters. Hydrophobic mismatch parameter is defined as $\Delta a_{IJ} = a_{IJ} - a_{II}$

Bead	Reference compound	Reference Model	Repulsive parameters kT/R_c
W	4 H_2O	W, monomer	$a_{WW} = a_{II} = 106.5$
T	$CH_3(CH_2)_6CH_3$	TT, dimer	$\Delta a_{TW} = 19.6$
M	$CH_3CON(CH_3)_2$	M, monomer	$\Delta a_{MW} = \Delta a_{MH2} = 3.0$, $\Delta a_{MT} = 3.0$
H_1	$CH_3OCH_2CH_2OCH_3$	H_1H_1, dimer	$\Delta a_{H1W} = 1.0$, $\Delta a_{H1T} = 6.5$
H_2	$OHCH_2(CHOH)_3CH_2OH$	H_2H_2, dimer	$\Delta a_{H2W} = 1.0$, $\Delta a_{H2T} = 9.8$
Potential	Definition of rigidity	$K_{1\text{-}2}$, $K_{1\text{-}3}$, $K\theta$	Equilibrium length/angle
1-2 bond	$E = K_{1\text{-}2}(r_{i,i+1} - r_e)^2$	40 [k_BT/R_c^2]	0.8 [R_c]
1-3 bond	$E = K_{1\text{-}3}(r_{i,i+2} - r_e)^2$	0–20 [k_BT/R_c^2]	1.6 [R_c]
angle	$E = K\theta(\theta - \theta_e)^2$	5–120 [k_BT/rad^2]	π

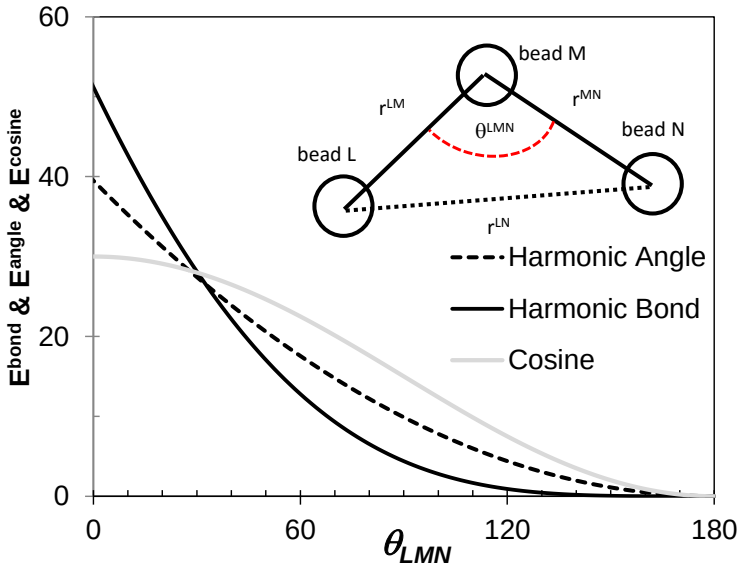

Figure 4-2. Two methods for accounting for the chain rigidity: second neighbor (1-3) bond harmonic potential (solid line) and harmonic angle potential (dashed line). Cosine rigidity potential $E(\theta) = K_\theta (1 + \cos \theta)$ employed in previously published studies [39] is shown by grey line for comparison.

Using the models and techniques described above, we calculated CMC and N_{ag} in model C_8E_8 and MEGA-10 surfactants for a wide range of hydrophobic mismatch Δa_{TW} and second neighbor rigidity $K_{1\text{-}3}$ parameters. The nearest neighbor bonds had the same length and rigidity in all systems (Table 4-1). The list of systems modeled and average properties obtained are given in Supporting Information, Table S1 of ref [81]. We considered 65 micellar solutions with surfactant volumetric fraction ϕ ranging from 0.02 to 0.06. This concentration range lies below the critical aggregation concentration for the systems considered. Simulation length was 2×10^6 DPD steps; time step of $\tau = 0.02\ \tau$ (3.83 ps) was chosen to keep temperature deviation under 1%. LAMMPS simulation package [106] was employed to perform DPD simulation.

Most simulations were performed in the simulation box of 30×30×30 R_c^3. Several addition simulations were performed in a larger box of 60×60×60 R_c^3 to confirm that the chosen box size of 30 R_c provides sufficiently accurate results for both CMC and N_{ag} with relatively inexpensive simulations. The influence of the box size on the system equilibration and on CMC and N_{ag} with example of C8E8 solutions are described in Supporting Information, section S-I. In order to evaluate the influence the surfactant concentration on micellization, we performed simulations of MEGA-10 solutions at ϕ = 0.01-0.08 (see Supporting Information, section S-II of ref [81]).

By quantifying the amount of micelles and free surfactants, we found that equilibrium was established after 5×10^5 steps. Once in 1,000 steps, configurations were saved for analysis. Two surfactant molecules were assumed to belong to the same aggregate if any two of their tail or middle beads overlapped. If an aggregate contained more than a certain threshold n_{mic} of surfactant molecules, it was counted as a micelle. If a surfactant molecule belonged to a cluster containing less than n_{mono} surfactant molecules, it was assumed to belong to the aqueous solution of monomers in equilibrium with the micelles. The concentration of "monomeric" surfactant in water was treated as the CMC. Aggregation was considered as complete and equilibrium reached when the CMC and micelle numbers stabilized and became practically insensitive to the choice of n_{mono} and n_{mic} within reasonable limits. In the "production" calculations, we used n_{mic} = 50 and n_{mono} = 10. A detailed discussion of choosing n_{mono} and n_{mic} can be found in ref. [1]. For CMC, statistical error calculated from mean square deviation ranged from 9% to 18%, with the averaged relative error of 14%. The deviation for N_{ag} ranged from 9% to 42%, based on the system and parameters.

A compendium of the simulation results for all 65 systems considered is given in Table S1 of Supplemental Information. As a typical example, we present in Figure 4-3 the two-dimensional diagram of the CMC dependence on Δa_{TW} and $K_{1\text{-}3}$ for MEGA-10 surfactant. The results obtained for two volume fractions of 2% and 4% confirm the accuracy of our calculations. This diagram shows that the CMC monotonically decreases with the increase of the hydrophobic mismatch and chain rigidity, so that the same CMC may correspond to the different sets of these parameters. The respective diagram of the N_{ag} dependence on Δa_{TW} and $K_{1\text{-}3}$ in given in Supporting Information, Figure S4 (b) of ref [81].

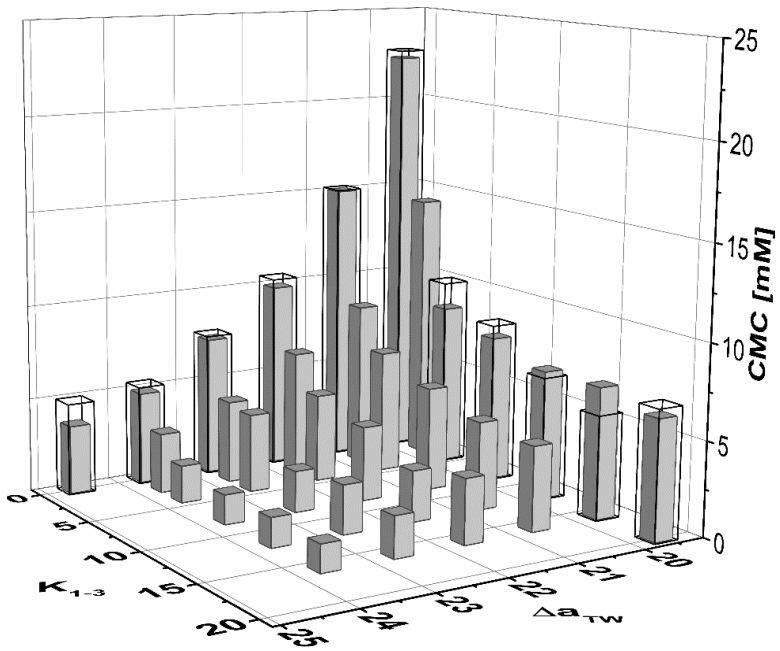

Figure 4-3. Dependence the critical micelle concentration (CMC) on the second neighbor bond rigidity ($K_{1\text{-}3}$) and hydrophobic mismatch (Δa_{TW}) parameters. MEGA-10 surfactant at volume fractions of 2% (open) and 4% (solid).

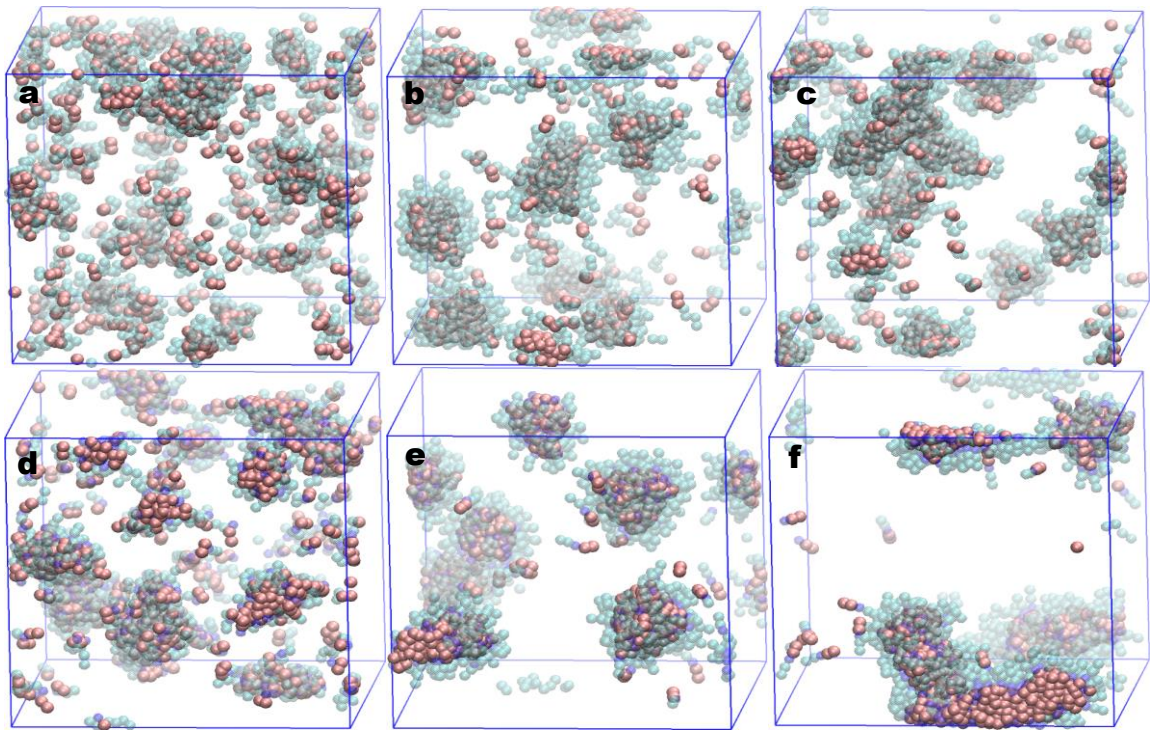

Figure 4-4. Micellization of C_8E_8 (a-c) and MEGA-10 (d-f) at 4% surfactant concentration. Head beads in cyan, tail beads in pink, middle beads in blue, water beads are not shown. (a) $\Delta a_{TW} = 19.6\ k_BT/R_c$, no chain rigidity is assigned, irregular segregation (b) $\Delta a_{TW} = 19.6\ k_BT/R_c$, chain rigidity maintained by 1-3 bonds, $K_{1\text{-}3} = 20$, well-defined spherical micelles (c) increased tail-water hydrophobic mismatch $\Delta a_{TW} = 23.6\ k_BT/R_c$, no rigidity with $K_{1\text{-}3} = 0$, agglomeration of micelles is evident. (d) $\Delta a_{TW} = 19.6\ k_BT/R_c$, no chain rigidity is assigned, irregular segregation (e) $\Delta a_{TW} = 19.6\ k_BT/R_c$, modest stiff molecules with chain rigidity maintained by harmonic angles, $K_\theta = 5$, well-defined spherical micelles (f) $\Delta a_{TW} = 19.6\ k_BT/R_c$, very stiff molecules with $K_\theta = 120$, worm-like micelles form.

Figure 4-4 shows snapshots of C_8E_8 and MEGA-10 surfactant solutions at $\phi = 4\%$. We keep repulsive parameters as well as the parameters for nearest neighbor bonds constant and adjust the second neighbor bond rigidity $K_{1\text{-}3}$ from zero (no rigidity, Figure 4a) to 20 k_BT/R_c^2 (Figure 4b). When no second neighbor force applied ($K_{1\text{-}3} = 0$), segregation is visually evident but irregular (Figure 4-4a). The aggregate size distribution (Figure 4-5, dashed line) shows that the probability of finding a molecule in an aggregate of size N decreases nearly monotonically with N. It is not even clear that this system is

indeed a micellar solution, since there is no clear qualitative criterion that allows distinguishing between "micelles" and smaller local "lumps," down to monomers dissolved in water.

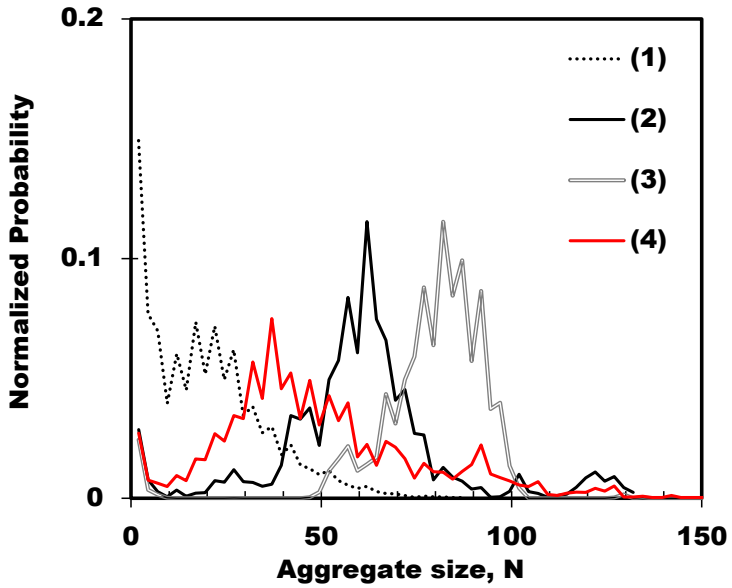

Figure 4-5. Probability distribution of finding a surfactant molecule in an aggregate consisting of N molecules for C_8E_8 at surfactant concentration of 4% vol. Line (1) (dotted): flexible model with no rigidity, $\Delta a_{TW} = 19.6 k_B T/R_c$. Line (2) (black solid): $\Delta a_{TW} = 19.6 k_B T/R_c$, rigidity applied using second neighbor harmonic bonds, $K_{1\text{-}3} = 20\ k_B T/R_c^2$. Line (3) (hollowed): $\Delta a_{TW} = 19.6 k_B T/R_c$, rigidity applied by harmonic angle potential $K_\theta = 5\ k_B T/\text{rad}^2$). Line (4) (red solid): flexible chains with no rigidity with increased tail-water repulsion $\Delta a_{TW} = 23.6\ k_B T/R_c$.

The situation changes rapidly as the rigidity is introduced. With a modest rigidity of $K_{1\text{-}3} = 5\ k_B T/R_c^2$, the surfactant forms well-defined spherical micelles. The distribution of micelle sizes rapidly changes: a well-defined minimum separates micelles from short-living small aggregates that are normally observed in molecular solutions. The former can be characterized by size and shape, which we will describe later. The resulting CMC decreases steeply as $K_{1\text{-}3}$ increases from 0 to $5\ k_B T/R_c^2$. Qualitatively similar observation

was reported in ref [107] where aggregation of two-dimensional model surfactants was studies by off-lattice Monte Carlo. If $K_{1\text{-}3}$ increases further, CMC appears to monotonically decrease as the surfactant molecule becomes more rigid. The micelles also become larger as $K_{1\text{-}3}$ increases from 0 to 5 k_BT/R_c^2 as N_{ag} rises from 58 to 70, but further increase in rigidity hardly affects the micelle size, which remains constant within a statistical error. The general decline of CMC with rigidity agrees with the literature. [22, 108]

Next, we examined, whether the effect of rigidity could be effectively compensated by increasing the short-range conservative repulsion between surfactant tail beads and water beads. Figure 4-6a,b shows CMC and N_{ag} for MEGA-10 surfactant. MEGA-10 behaved qualitatively similar to C_8E_8 (Figure 4-6c,d). As the rigidity is introduced, CMC falls sharply and the micelle size increases. As $K_{1\text{-}3}$ exceeds 5 k_BT/R_c^2, both properties show saturation with a modest influence of rigidity on CMC.

Same Figure 4-6 shows CMC and N_{ag} for flexible (no second neighbor bonds or angle potentials) surfactants with tails of different degrees of hydrophobicity quantified by Δa_{TW} parameter (definition in Table 4-1). Naturally, Δa_{TW} significantly affects the CMC (Figure 4-6a, c, red circles) and strongly hydrophobic tails make micellization well defined (Figure 4-5). No "saturation" is observed in CMC vs Δa_{TW} dependence, which can be approximated as an exponential decay (shown in Supporting Information, Figure S5a of ref [81]). CMC declines steeply as Δa_{TW} increases, similar to what we observed for CMC on increasing $K_{1\text{-}3}$ and fixed Δa_{TW}. Thus, the effect of the rigidity on CMC can be easily mimicked via changing the short-range repulsion forces. For example, completely flexible

MEGA-10 surfactant with $\Delta a_{TW} = 22.6\ k_BT/R_c$ has approximately the same CMC as a rigid surfactant with $\Delta a_{TW} = 19.6\ k_BT/R_c$ and $K_{1\text{-}3} = 16\ k_BT/R^2_c$.

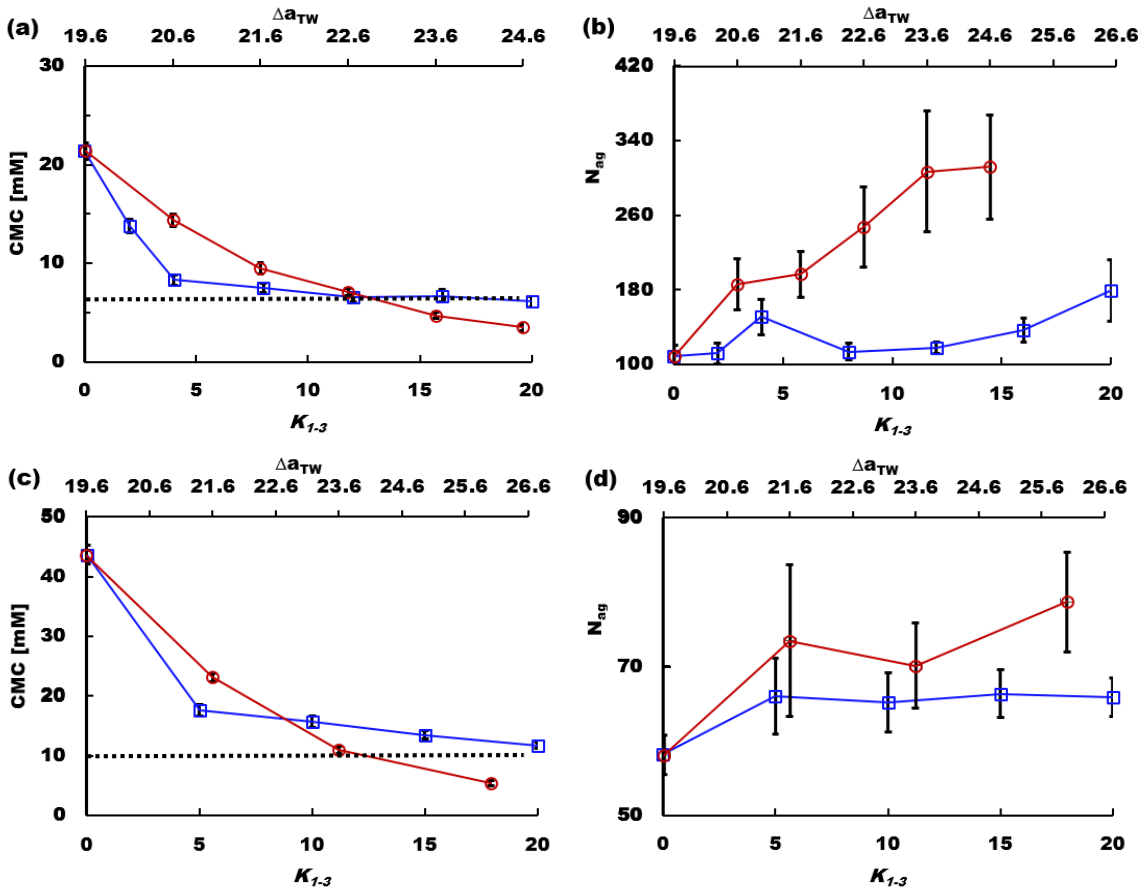

Figure 4-6. Averaged critical micelle concentration CMC and aggregation number N_{ag} of MEGA-10 (a, b) and C_8E_8 (c, d) at 4% surfactant concentration. Parameters (independent variables) are referred to the two abscissa axis: rigidity to the bottom axis (blue) and conservative mismatch Δa_{TW} to the upper axis (red). Ordinate show CMC (a,c) and N_{ag} (b,d) of the surfactants. Blue squares show the dependence of CMC and N_{ag} on $K_{1\text{-}3}$ with a constant $\Delta a_{TW} = 19.6\ k_BT/R_c$. Red circles show the dependence of CMC and N_{ag} on tail-solvent hydrophobic mismatch Δa_{TW} for flexible chains ($K_{1\text{-}3} = 0$). Black dotted lined indicate experimental CMC values for MEGA-10 (a) and C_8E_8 (c). Error bars for of CMC are comparable with the symbol size.

The same, however, cannot be said about the micelle size and shape. For example, Figures 4-4 b,c depict micellization of C_8E_8 in two systems with approximately the same

CMC: in one system rigidity is produced by second neighbor bonds, and the other one formed by flexible molecules with Δa_{TW} increased from 19.6 to $\Delta a_{TW} = 23.6\ k_B T/R_c$. System formed by rigid molecules (Figure 4-4b) forms well-defined near-spherical micelles, while in the system of flexible surfactants with stronger tail-water repulsion, micelle aggregation becomes evident. Figure 6d shows that despite similar CMC, N_{ag} for the flexible system is greater proximately threefold.

The shape of the aggregated was quantitatively characterized by asphericity factor A,[109] a generalized quantitative measure of the departure from spherical symmetry for the gross shape of a polymeric molecule [110] or percolating clusters. [22] A is obtained from the gyration tensor **S** calculated for each micelle: $S_{ij} = \frac{1}{N}\sum_{l=1}^{N}\left(S_{il} - S_i^{CM}\right)\left(S_{jl} - S_j^{CM}\right)$ and S_i^{CM} stands for the center of mass in coordinate i (i denotes x, y, or z). After three eigenvalues R_1^2, R_2^2, R_3^2 of the gyration tensor are obtained, asphericity is calculated as $A = \frac{1}{2R_g^4}\left[\left(R_1^2 - R_2^2\right) + \left(R_1^2 - R_3^2\right) + \left(R_3^2 - R_2^2\right)\right]$, where $R_g^2 = R_1^2 + R_2^2 + R_3^2$ is the radius of gyration. Asphericity ranges from zero for spherically symmetric objects to 1 for an infinite cylinder. In Figure 4-7, we compare the distribution of asphericity for two C_8E_8 systems, which have the same CMC: rigid chains characterized by $\Delta a_{TW} = 19.6\ k_B T/R_c$ and $K_{1\text{-}3} = 20\ k_B T/R_c^2$ and flexible chains characterized by $\Delta a_{TW} = 23.6\ k_B T/R_c$ and $K_{1\text{-}3} = 0$. In the latter case, the absence of rigidity is compensated by increased hydrophobic mismatch to provide the same CMC. Figure 4-7 clearly shows that the system with equal CMC values may exhibit drastically different patterns during the micellar self-assembly. The prominent peak at approximately A = 0.09 on the asphericity distribution corresponds to well-defined

spherical micelles. In the flexible surfactant system, elongated non-spherical aggregates prevail. It appears from the snapshots shown in Figure 4-4c that the larger aggregates are formed by micelles merged by their hydrophobic cores instead of well-defined worm-like micelles that should precede the formation of hexagonal liquid crystal. We may assume that although CMC of these two model surfactants coincide, the critical aggregation concentrations, testing of which is beyond the capability of our simulations, should be drastically different.

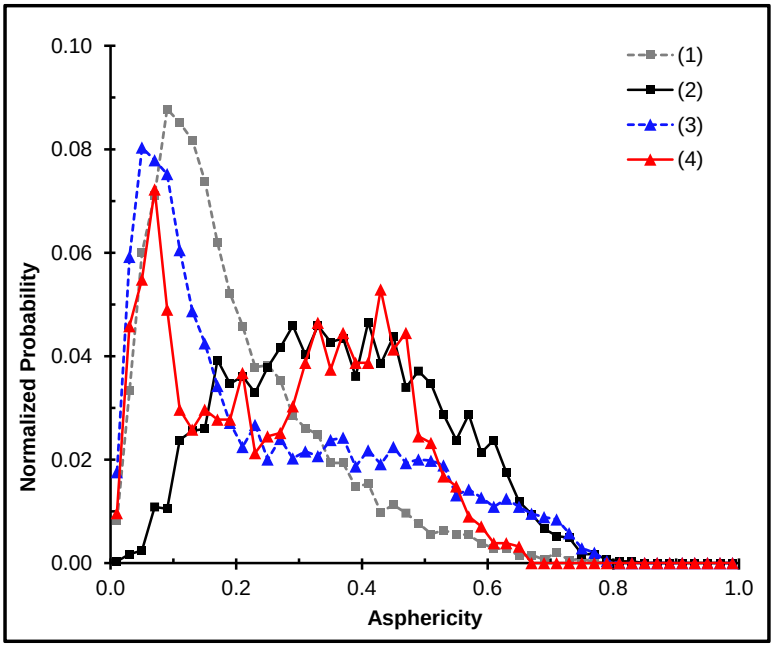

Figure 4-7. Distribution of the micelle asphericity factors in different systems. (1) Spherical micelles in C_8E_8 surfactant, Δa_{TW} = 19.6 k_BT/R_c, rigidity applied using second neighbor bond, $K_{1\text{-}3}$ = 20 k_BT/R_c^2. (2) Non-spherical symmetric aggregates in C_8E_8 type surfactant, flexible model with stronger tail-water hydrophobic mismatch Δa_{TW} = 23.6 k_BT/R_c, $K_{1\text{-}3}$ = 0. (3) Mostly spherical micelles in MEGA-10 type surfactant, Δa_{TW}=19.6 k_BT/R_c, rigidity applied using the harmonic angle potential, K_θ = 5k_BT/rad^2. (4) Worm-like micelles in MEGA-10 type surfactant, Δa_{TW} = 19.6 k_BT/R_c, very rigid model, K_θ = 120k_BT/rad^2.

In order to compare to what extend the choice of the rigidity potential affect the results of simulations, we studied micellization for very rigid surfactants, using the harmonic angle potential with K_θ ranging from 0 to 120 k_BT/rad^2. At relatively low K_θ values, the harmonic angle potential influences micellization similarly to the second-neighbor bond potential as shown in Figure 4-4d,e: the CMC decreases, while the micelle size increases, and micelles remain predominantly spherical (Figure 4-7). However, further increase in rigidity leads to the formation of large worm-like micelles. For example, the snapshot presented in Figure 4-4f, shows both smaller spherical and larger worm-like micelles. In Figure 4-7, these two types of aggregates are evident from two peaks on the asphericity factor distribution: a sharp peak around A = 0.07 corresponding to spherical micelles and a low broad peak (A = 0.33 – 0.47) corresponding to work-like aggregates. We should note that such a stiff model can by no means represent MEGA-10; for example, a very rigid surfactants may be built with polyaromatic (for example, rigid polyaromatic spacers are used in Gemini-type surfactants [111]), other polycyclic (such as sodium cholate [112]) or alkyne-type fragments. Because the rigid angle potential imposes constrains on conformations adopted by the tails, the tail beads cannot be efficiently packed inside the spherical micelle cores, which makes the spherical shape less favorable. Obviously, more efficient packing is possible within cylindrical micelle cores, which leads to the formation of work-like micelles. Interestingly, CMC monotonically decreases with the rigidity, despite the disruption of the micelle core structure by the angle potential. The effect of rigidity is expected to be even stronger for longer amphiphiles such as block copolymers, where the packing of hydrophobic tails in micelle cores should be even more important

than for short molecules studied here. Nevertheless, the effect of rigidity on the micelle shape is consistent with the experimental observations described in the introduction.

To conclude, the present work shows the importance of accurate accounting for the rigidity of molecules in DPD simulations of self-assembly processes, even in dilute surfactant solutions. We considered two common surfactants of different chemical structures: octaethylene glycol monooctyl ether and *n*-decanoyl-N-methylglucamine. Rigidity was introduced either with the second-neighbor harmonic bonds or harmonic angles potentials, so that the linear straight conformation corresponded to the minimum of intramolecular energy. We found that rigid surfactants had substantially lower CMC and form larger and better-defined micelles than flexible molecules with the same non-bonded interaction parameters. As rigidity increases further, its effect on micellization weakens significantly. The effects of rigidity on CMC and aggregation morphology are consistent to what were observed in the literature. [22] We also found that the effect of rigidity on CMC cannot be effectively mimicked by strengthening the hydrophobic mismatch between the hydrophobic tail and solvent beads: the parameters that produce the same CMC result in much higher average micelle size, as micelles of the more flexible surfactant easily aggregate and form larger agglomerates. Therefore, if we imagine a set of structurally similar linear surfactants with different tail hydrophobicity and chain rigidity but the same CMC, the aggregation number will have a minimum corresponding to the surfactants of intermediate rigidity: micelles formed by completely flexible surfactants tend to aggregate, while very rigid molecules tend to form well-defined rod-shaped micelles. As a methodological outcome, we conclude that the introduction of the second neighbor harmonic bonds is a convenient and efficient method for accounting for the chain rigidity

in DPD simulations. This potential can be parameterized from the analysis of the number of flexible angles in the coarse-grained chain fragment, as discussed in ref. [1] The proposed method can be recommended for studies of self-assembly and dynamics in various soft matter systems beyond the surfactant solutions considered here.

Section 5. Parameterization for chain configuration

In this section, we discuss the method rigorously determining the chain configuration. The target systems is the surfactant solution of C_nE_m with different coarse-graining levels and the forcefield used in DPD simulations. The rigidity on the head and tail segments on the basis of atomistic MD modeling of bulk phases of alkanes and PEO. We fit the bonded terms of the DPD model to configuration observed in MD. We choose reference compounds for the tail block on different coarse-graining levels based on the protocol introduced in section 3 of matching the intracomponent repulsion parameters to activities in solutions reference compounds, including IDAC and the solvent activities in polymers.

The scheme is applied to quantitative prediction of critical micelle concentration (CMC) and aggregation number (N_{ag}) in aqueous solutions of C_nE_m surfactants, where quantitative prediction of micellar properties is a benchmark problem for testing the new parameterization algorithm in DPD. [1, 113-114] We compare the performance of two methods in calibrating the bond and rigidity that is rigorously determined using FENE potential and estimated from the number of flexible torsions using harmonic potential as in section 3.

The neighboring beads in a surfactant model are connected by bonds (1-2 bond). Additional bonds are also applied on the second neighbor beads (1-3 bond) in order to describe the rigidity of the chain that significantly influences surfactant micellization. [81] The bonds are described by the FENE potential as introduced in section 2, which describes molecular rigidity better than the standard harmonic springs. [82]

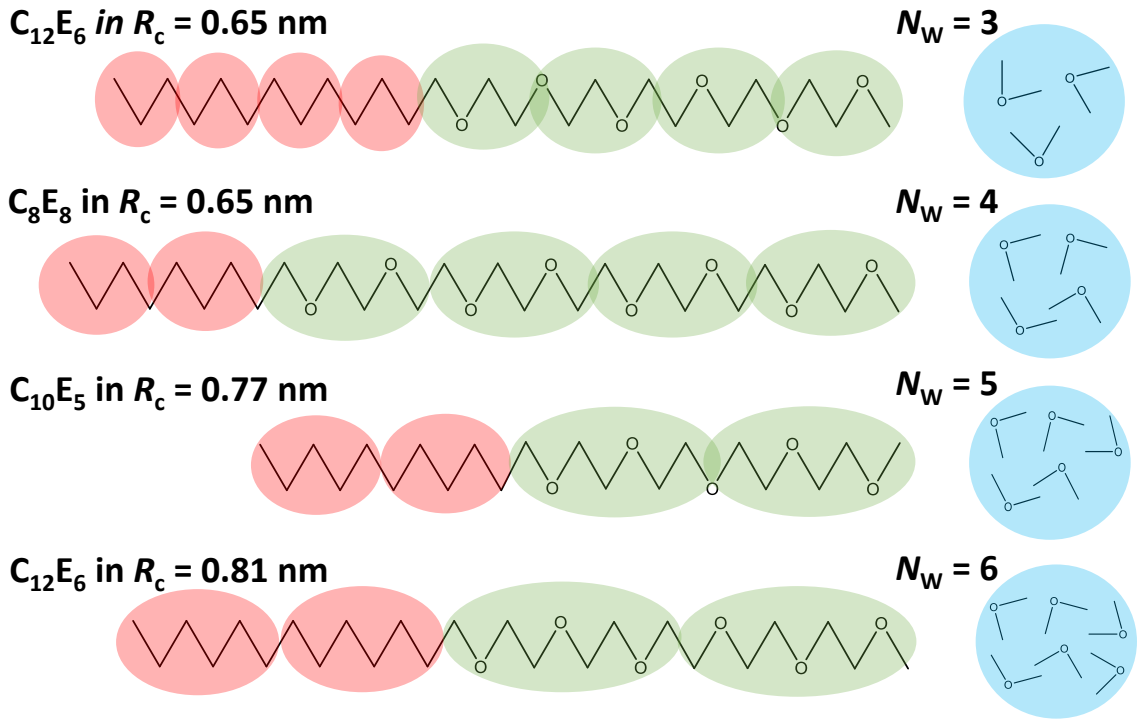

Figure 5-1. Examples of coarse-grained models of C_nE_m surfactrants with different bead diameter R_c. T beads (red) are for hydrophobic tail, and H beads (green) are for hydrophilic head. Water beads (blue) with corresponding bead size are illustrated by N_W, the number of water molecules in aW bead.

A C_nE_m surfactant molecule consists of an n hydrophobic alkyl monomer (CH_3 or CH_2) and m hydrophilic oxyethylene units (CH_2OCH_2). We model several systems with alkyl tail length from n = 8 to n = 12 and the PEO head from m = 3 to m = 9. The first DPD model of C_nE_m was introduced by Groot and Rabone, who studied the effect of such surfactants on the properties and rupture of lipid bilayers. [4] Parameterization was based on Flory-Huggins model parameters. Other coarse-grained simulation techniques were also allied to CE surfactants; for example, Jusufi et al. [115] derived hard-core potentials from atomistic simulation of short PEO oligomers in the water. CMC and aggregation number for C_nE_m (n = 6 to 12, m = 3 to 9) near-quantitatively reproduced the experimental results.

Coarse grained representations of C_nE_m surfactants are denoted as T_xH_y, where T denotes a hydrophobic tail bead and H denotes a hydrophilic head bead. The beads are connected by bonds into a single chain. The termination hydroxyl group of the E_m black is usually not modelled separately in DPD to reduce the number of parameters. [1, 4, 81] Based on the neutron reflection data [92] interpreted by Groot and Rabone, [4] two ethyl groups are assumed to occupy the same volume as one oxyethylene or two water molecules. For example, a T bead denotes a ($CH_xCH_2CH_2CH_2$) fragment of the hydrophobic alkyl block and a head bead denotes ($CH_2OCH_2CH_2OCH_2$) if one water bead contains four water molecules. From the liquid densities of octane and water at ambient conditions, we estimate that R_c equals to 0.65 nm, 0.71 nm, 0.77 nm, and 0.81 nm when a water bead W contains 3, 4, 5, and 6 water molecules, respectively. Details of coarse graining are listed in the Table 5-1.

Table 5-1. Surfactant ($CH_3(CH_2)_{n-1}(OCH_2CH_2)_mOH$) (a.k.a. C_nE_m) molecules and the corresponding DPD models T_xH_y at chosen bead size R_C (diameter in nm). Subscript n and m are the numbers of methylene and ethylene oxide groups, and x and y are the numbers of tail and head beads. System size (box length in R_C) varies based on the experimental CMC. Last two columns are reference compounds and the models in the calibration for inter-species parameters.

C_nE_m		T_xH_y		R_C (nm)	a_{II}	T bead fragment	H bead fragment
n	*m*	*x*	*y*				
8	4	2	2	0.71	106.1	$(CH_2)_4$	$(CH_2OCH_2)_2$
8	6	2	3	0.71	106.1	$(CH_2)_4$	$(CH_2OCH_2)_2$
8	8	2	4	0.71	106.1	$(CH_2)_4$	$(CH_2OCH_2)_2$
10	5	2	2	0.77	133.7	$(CH_2)_5$	$(CH_2OCH_2)_{2.5}$
12	3	4	2	0.65	78.5	$(CH_2)_3$	$(CH_2OCH_2)_{1.5}$

12	6	4	4	0.65	78.5	$(CH_2)_3$	$(CH_2OCH_2)_{1.5}$
12	9	4	6	0.65	78.5	$(CH_2)_3$	$(CH_2OCH_2)_{1.5}$
12	8	3	4	0.71	106.1	$(CH_2)_4$	$(CH_2OCH_2)_2$
12	3	2	1	0.81	161.2	$(CH_2)_6$	$(CH_2OCH_2)_3$
12	6	2	2	0.81	161.2	$(CH_2)_6$	$(CH_2OCH_2)_3$
12	9	2	3	0.81	161.2	$(CH_2)_6$	$(CH_2OCH_2)_3$

Box size (R_C)	Reference compounds for tail	Models for reference compounds
30	octane	dimer
30	octane	dimer
30	octane	dimer
45	decane	dimer
60	hexane	dimer
60	hexane	dimer
60	hexane	dimer
64	octane	dimer
60	hexane	monomer
60	hexane	monomer
60	hexane	monomer

Since water occupies almost the entire volume of the system, the self-repulsion parameters a_{II} are set equal for all bead types and fitted to isothermal compressibility of water. Because of difference in opinions in the literature on the scaling of the intramocomponent repulsion parameter with size, we performed MC simulations on the dependence of the compressibility on a for the reduced temperature range of $1.0 < T < 1.2$. The simulation results are shown in Supporting Information, Section S1. The correlation between isothermal compressibility as a function of a_{II} and T in reduced DPD units can be approximated as $\kappa_T = \left[1.686 + 0.112 \cdot \left(T - T_0 \middle/ T_0\right)\right] \cdot a_{II}$. Converting the equation using the physical unit of $k_B T$ and R_c, and matching to the experimental isothermal compressibility of water at the temperature, we obtain the intracomponent repulsion parameter that

$$a_{II} = 0.305 R_c^3 \cdot \left[1 - 0.95 \cdot \left(T - T_0 \middle/ T_0\right)\right] - 3.5 \qquad (5\text{-}1)$$

In general, the compressibility declines approximately linearly with a_{II} and our results are in good agreement with the GW correlations. A discrepancy with our previous work (see Supporting information to ref [1]) is obtained for high a_{II} ; the data reported here is certainly more precise. By matching the correlation obtained to the experimental compressibility of water, we calculated a_{II} for different R_c (Table 5-1). They are in reasonable agreement with the values used in the literature [4, 7, 33] and increase almost proportional to R_c^3. This result was expected because the dimensionless compressibility κ obtained in simulations is independent on R_c [28] while conversion coefficient between the reduced and physical units is proportional to R_c^3.

Having chosen the intracomponent repulsion parameters, we choose the parameters of nearest neighbor (1-2) and second neighbor (1-3) bonds. We fitted the bond parameters to the results of atomistic MD simulations. The procedure is identical to that from ref [7]. The bonds between T beads were parameterized from the best match between the atomistic and coarse-grained structures of liquid hexadecane. Hexadecane molecule was dissected into equal fragments of 3, 4, 5, or 6 carbons, according to the corresponding bead size (R_c = 0.65, 0.71, 0.77, and 0.81 nm). We calculated intramolecular distance distributions between the centers of mass of the fragments. These were matched to the distributions of the distances between corresponding beads of the coarse-grained model of hexadecane melt by adjusting the 1-2 and 1-3 FENE bond parameters (coarse-grained $C_{15}H_{32}$ was modelled for R_C = 0.65 nm and R_C = 0.77 nm, $C_{16}H_{34}$ was modelled for R_c = 0.71 nm and R_c = 0.77 nm, $C_{18}H_{38}$ was modelled for R_c = 0.81 nm). The schematics of the mapping procedure is shown as Figure 5-2a, and the obtained bead-to-bead distance distributions are shown in Figure 2b-e. It is clear that we are able to mimic the flexibility of the alkane tail in DPD simulations very well. We should notice that FENE bonds turned out to be superior to the harmonic in reproducing the rigidity of surfactant molecules.

In order to obtain bond parameters for the hydrophilic PEO head, we simulated PEO fragments of 9 monomers using a similar procedure. The shapes of intra-molecular bead-bead distance distributions are much more complex for PEO melts compared to alkanes. In general, the PEO chains are more flexible with shorter persistent length. Small peaks on the MD distributions correspond to particular preferential conformations of the PEO chains. However, we managed to reproduce the overall rigidity of the PEO chains

very reasonably as shown in Figure 5-2. All bond parameters are concluded in Table 5-2a-b.

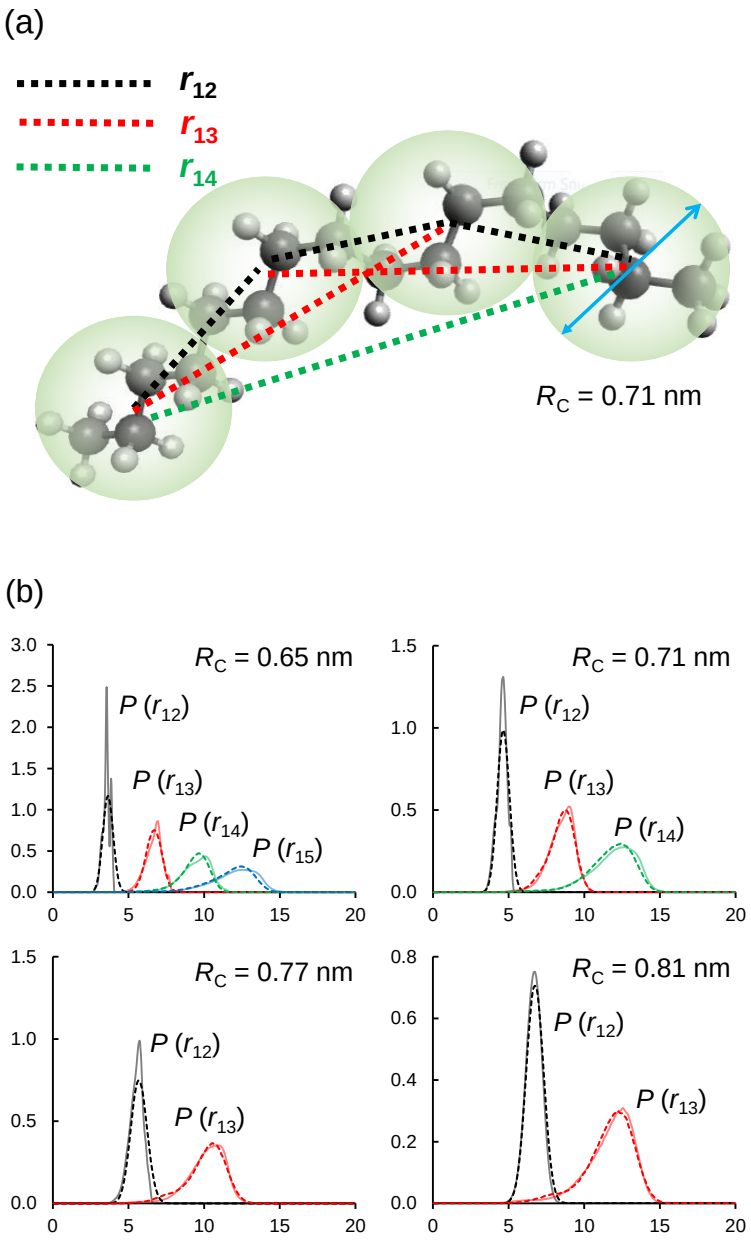

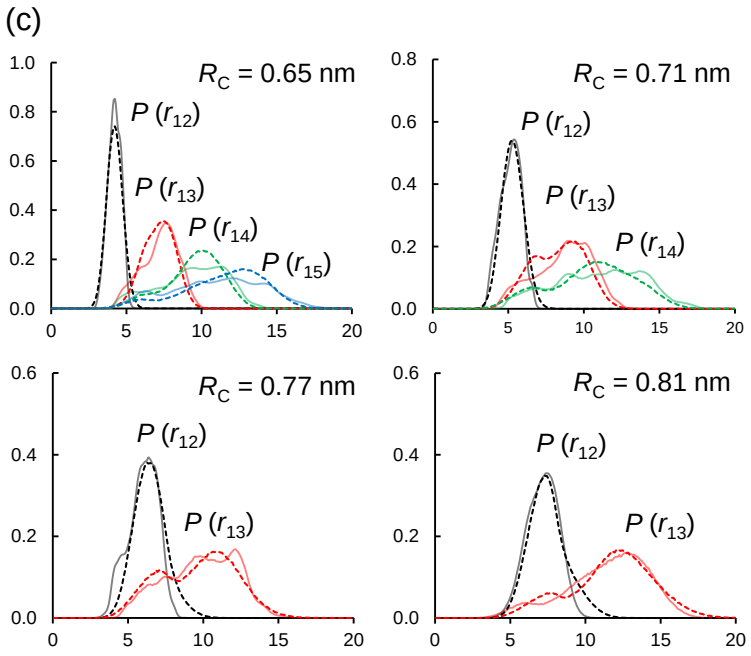

Figure 5-2. (a) Schematics of MD-DPD mapping. Example shows the hexadecane modeled by coarse grained bead sized 0.71 nm. Each beads represents four methylene groups. Center to center bead distances are calculated for DPD model (four connected beads) for r_{12}, r_{13}, r_{14}, etc. The reference "coarse grained" MD coordinates are calculated from the center of mass from the bead components. (b-e) Normalized distribution of center-to-center bead distance from DPD (dashed lines) and of the distances between the center of masses for alkane chain fragments from atomistic MD simulations (solid lines) (f-i) Normalized distribution of center-to-center bead distance from DPD (dashed lines) and of the distances between the center of masses for PEO-400 chain fragments from atomistic MD simulations (solid lines).

Table 5-2. FENE bond parameters obtained from the MD-DPD mapping for (a) surfactant tail and (b) surfactant head. Parameters for tail and head of modeled C_nE_m surfactant are mapped to reference compounds hexadecane and PEO-400. Nearest neighbor (1-2) bond provide connectivity, and second neighbor (1-3) bonds provide the rigidity of the molecule. r_0 and r_m are equilibrium bond length and maximum extendibility as described in Section 2. Table (c) contains the approximated bond and rigidity using the approach in ref. [1]

(a) Surfactant tail, FENE potential

R_C (nm)	a_{II}	Bond type	K_B	r_0	r_m
0.65	78.5	1-2	280.0	0.50	2
		1-3	80.0	1.11	4
0.71	106.1	1-2	280.0	0.61	2
		1-3	20.0	1.50	4
0.77	133.7	1-2	180.0	0.70	2
		1-3	8.0	1.85	4
0.81	161.2	1-2	190.0	0.81	2
		1-3	8.0	1.75	4

(b) Surfactant head, FENE potential

R_C (nm)	a_{II}	Bond type	K_B	r_0	r_m
0.65	78.5	1-2	100.0	0.56	2
		1-3	15.0	1.30	4
0.71	106.1	1-2	64.0	0.66	2
		1-3	5.0	1.42	4
0.77	133.7	1-2	30.0	0.75	2
		1-3	2.0	1.55	4
0.81	161.2	1-2	30.0	0.85	2
		1-3	2.2	1.90	4

(c) Approximated harmonic potential

R_C (nm)	Bond type	tail		head	
		K_B	r_0	K_B	r_0
0.65	1-2	106.7	0.6	71.1	0.9
	1-3	53.3	1.2	35.6	1.8
0.71	1-2	80.0	0.8	53.3	1.2
	1-3	40.0	1.6	26.7	2.4
0.81	1-2	53.3	1.2	35.6	1.8
	1-3	26.7	2.4	17.8	3.6

For comparison, we also examine the capabilities of a more simplistic model with harmonic potentials $\mathbf{F}_{ij}^{(B)}(\mathbf{r}_{ij}) = -K_B\left(r_{ij} - r_0\right)$ for 1-2 and 1-3 bonds according to ref. [1]For this simplistic model (further on referred to as Model 2, while the "regular" model with bonding parameters fitted to MD simulations is referred to as Model 1) 1-2 and 1-3 bond parameters were scaled by the number of flexible torsions between the connected bead centers $K_B = 160 / n_{tors}$ for 1-2 bonds and 1-3 bonds. r_0 were fixed to the distance between neighbor beads arranged in perfect BCC lattice at $\rho R_c^3 = 3$: r_0 was fixed to $r_0 = 0.2 n_{tors}$ for 1-2 and 1-3 bonds. The respective parameters of both models are given in Table 2c.

Inter-component repulsion parameters for tail T, head H, and water W beads are obtained from the activities in reference binary solutions. For hydrophobic beads T we choose different linear alkanes as reference compounds, the choice depends on R_c. The reference compound must be a liquid well below its boiling temperature at the simulation

conditions. That is, the smallest suitable alkane is hexane, which serves as the natural reference compound for T bead both with the coarsest dissection (Figure 5-1c) of R_c = 0.81 nm, where one T bead effectively represents six methyl/methylene groups. Correspondingly, hexane in this case is modeled as single bead T molecule. At finer coarse-graining levels, reference alkanes are presented as dimers of tail beads TT. For R_c = 0.65 nm T bead comprised of three CH_x groups is modeled as a TT dimer. Respectively, the reference compounds for R_c = 0.71 nm and R_C = 0.77 nm are octane and decane. The reference compounds and models are listed in Table 5-1.

The inter-component parameters mismatch between T and W beads is fitted to the experimental IDAC. We obtained calibration curves for $\gamma^{\infty}(\Delta a_{IJ})$ in a series of DPD or Monte Carlo simulations of pure reference compound for bead I, augmented by Widom insertion of a test molecule which constitutes a reference compound for bead J. For a given a_{IJ}, γ^{∞} is calculated using Eq. 5-2 (derived in ref [1], see Supporting Information):

$$\ln \gamma_{\mathbf{J}}^{\infty} + \ln\left(\frac{n_{\mathbf{I}} b_{\mathbf{J}}}{n_{\mathbf{J}} b_{\mathbf{I}}} \frac{\rho_{\mathbf{IJ}}}{\rho_{\mathbf{JJ}}}\right) = \ln\left\langle \exp\left(-E_{\mathbf{JJ}}^{\mathbf{ins}} / kT\right)\right\rangle - \ln\left\langle \exp\left(-E_{\mathbf{IJ}}^{\mathbf{ins}} / kT\right)\right\rangle \qquad (5\text{-}2)$$

γ^{∞} values obtained experimentally or by thermodynamic modeling are then interpolated onto the reference curves. For type J, n_J is the number of physical molecules that a coarse grained molecule represents (here, for water bead $n_J = N_W$, for alkanes n_J = 1). b_J is the number of beads in the coarse grained molecule (b_J = 1 for monomers, b_J = 2 for dimers and so on). $E_{\mathbf{IJ}}^{\mathbf{ins}}$ is the insertion energy for inserting of the reference molecule for J bead type into a bath of reference molecules for I bead type, which changes with the assigned repulsion parameters a_{IJ}. If the solvent molecule is dimer, we adjust the solvent density in

order to match the pressure of the solvent of monomer (water). Such adjustment is similar to Kacar et al, [30] and contributes to the correction term ρ_{IJ}/ρ_{JJ} . ρ_{IJ} is the density for the system inserting species J into the solvent of I. As illustrated schematic in Figure 5-3a, the density ρ_{IJ} is different than the density of the reference system ρ_{JJ} which equals to 3.

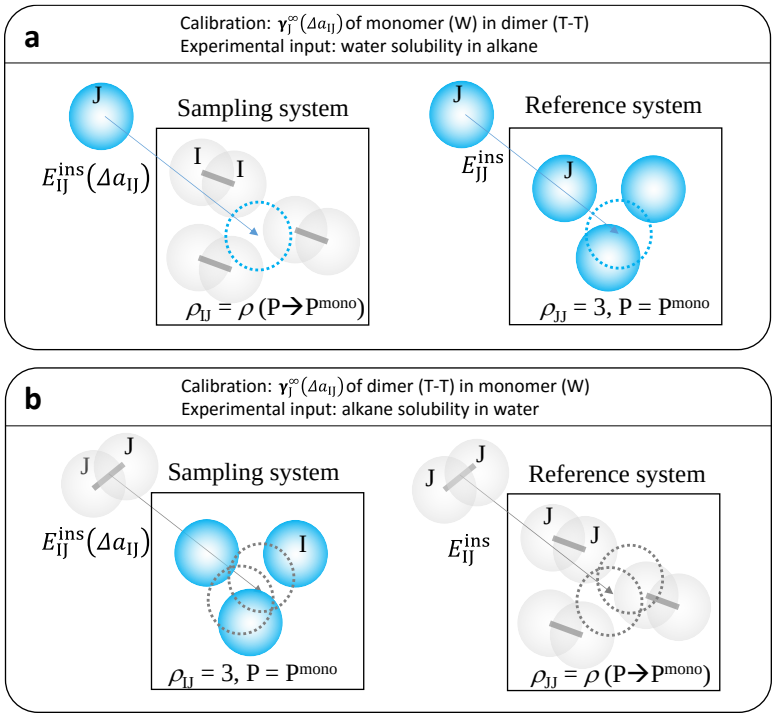

Figure 5-3. Example of the MC simulations for calculations of calibration relationship (Eq. 5-2). Reference compound for bead I is a single-bead molecule (monomer) and the reference compound for molecule J is a dimer. The calibration relationship (eq. 5-2) calculated for JJ molecules in I bath and for I molecules in JJ bath. Thus, for each Δa_{IJ} two MC simulations are performed. Additionally, we perform simulations to obtain insertion energies of I molecules in I bath and JJ molecules in JJ bath. The density in JJ bath is adjusted to give the same pressure as in I bath, where ρR_c=3.

It is worth noting that although ln (ρ_{IJ}/ρ_{JJ}) term is negligible (we used ρ = 3 for monomer solvent. ρ = 3.11, 3.05, and 3.01 for TT dimer at R_C = 0.65 nm, 0.71 nm, and 0.81 nm), the densities of the baths ρ_{IJ} and ρ_{JJ} substantially affect the insertion energies

and therefore dramatically change the calibration curves $\gamma^{\infty}(\Delta a_{IJ})$. This is because short and stiff bonds that reproduce the chain rigidities (Table 5-2) affect the fluid structure in the bath, which becomes quite different from the structure of one component DPD fluid with the same R_c. In the simulation of surfactant solution, water constitutes the bulk (96% in volume) of the system and alone determines the pressure in NVT ensemble. The hydrophobic cores of the micelles are effectively under constant pressure conditions created by the solvent, even though the DPD simulations are carried out in the canonical ensemble. For this reason, the reference $\gamma^{\infty}(\Delta a)$ curves for systems with dimers were calculated at pressure that corresponds to the solvent (a single-bead fluid) at the reduced density of $3R_C^{-3}$. Note that this issue is not significant for dimers with very soft bonds [23] or at $r_0 = 0.8$, [1, 81] (such as $R_c = 0.71$ nm in the Model 2 used in this paper) because the resultant fluid structure is very close to that of monomers and the pressure at $\rho R_c^3 = 3$ is practically the same as in the solvent bath.

With this procedure, we obtain the reference correlations between γ^{∞} and Δa for different system types. The correlations are given in Table 5-3. All reference curves are monotonic, but we have to note that the slope depends on the bead size, as shown in Figure 5-4. Even for the same physical solution of two molecules of similar sizes (say, hexane and water), different values of Δa are needed to achieve the same solubility for different coarse graining levels, especially when this liquids are very dissimilar and strongly separate. This is related to the dependence of the DPD fluid structure on a_{II} and should be taken into account when Δa is calculated from thermodynamic properties of reference solutions, including the calculations of Δa from FH parameters χ. For alkane-water mixtures, γ^{∞} are

estimated from the experimental solubilities (reciprocal of mole fraction) and interpolated onto the corresponding reference curves. Following ref. [1] we averaged the a_{TW} parameters obtained from water solubilities in alkanes and alkane solubilities in water. We have to mention that the experimental errors for such insoluble compounds as octane and decane are very substantial, but several sources give values that are reasonably consistent and they are used in the present work. We took the values recommended by IUPAC series [95, 116-117] that collect and examine different resources. The resulting parameters are given in Table 5-4.

The average tail-water mismatch parameters depend on the bead size. Generally, the larger the bead size, the higher Δa_{TW} . The reason that Δa_{TW} for R_c = 0.65 nm is higher than that for R_c = 0.71 nm is due to the shorter bond enforced on the tail-tail connection, and it need to be compensated somehow to reach the correct overall hydrophobicity. Such effects is not considered while Δa is mapped to Flory-Huggins parameters, for the Flory-Hugging theory assumes flexible molecules. In model 2 where the bond r_0/R_c is fixed, a_{TW} monotonically increases with Rc. It is difficult to tell to which extent the linearity ($\Delta a \propto R_c$) suggested in ref [28] holds, but the increase in significant.

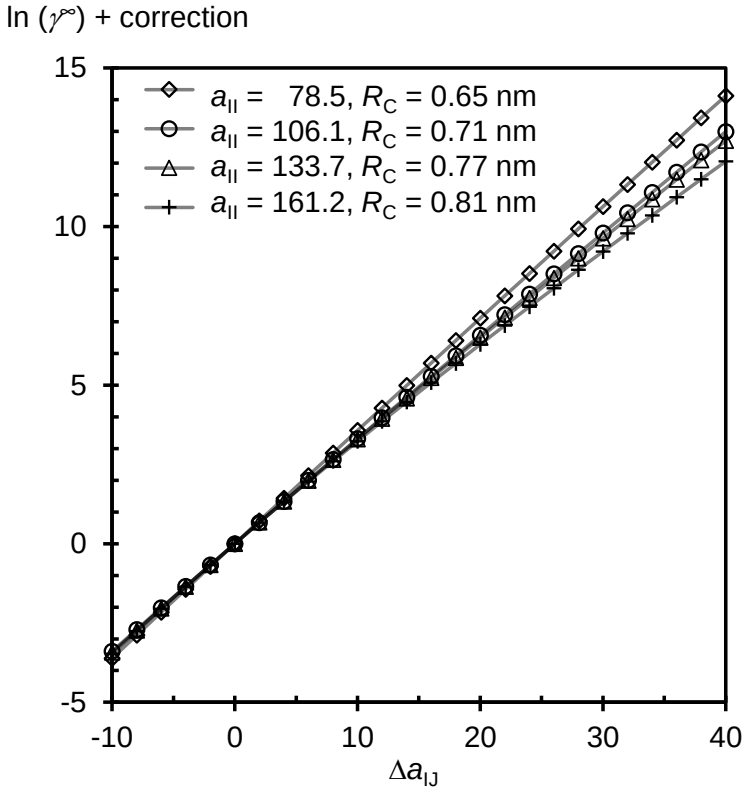

Figure 5-4. Calibration correlation between Δa and infinite dilute activity coefficient for two single bead components of types I and J. The correction term is independent of a_{IJ} given by the LHS of eq 5-2.

Table 5-3. Parameters for calibration relationships $\ln \gamma_A^{\infty} + \text{correction} = m\, \Delta a_{TW} + b$

solute: monomer,			solute: monomer,			solute: dimer		
R_C (nm)	m	b	R_C (nm)	m	b	R_C (nm)	m	b
0.65	0.31	0	0.65	0.29	0.33	0.65	0.63	-2.28
0.71	0.32	0	0.71	0.33	0.69	0.71	0.74	-1.23
0.77	0.33	0	0.77	0.34	-0.12	0.77	0.81	-1.80
0.81	0.35	0						

Table 5-4. Mismatch parameters for T -- W interactions obtained with eq.4 Model 1 use the calibration curves in Table 3. Model 2 use the approximate bond length from ref [1] Table 2c.

R_C (nm)	Compound	Model	solubility[ref]		Δa (method 1)	Δa
0.65	hexane	dimer	2.40E-06[116]	Δa_{TW}	21.2	22.3
	3 H_2O	monomer	6.10E-04[116]	Δa_{WT}	30.5	15.2
				avg. Δa_{TW}	25.9	18.8
0.71	octane	dimer	1.10E-07[95]	Δa_{TW}	20.4	24.6
	4 H_2O	monomer	6.10E-04[95]	Δa_{WT}	26.4	13.6
				avg. Δa_{TW}	23.4	19.1
0.77	decane	dimer	3.30E-09[117]	Δa_{TW}	23.6	-
	5 H_2O	monomer	6.30E-04[117]	Δa_{WT}	28.7	-
				avg. Δa_{TW}	26.1	-
0.81	hexane	monomer	2.40E-06[116]	Δa_{TW}	31.5	41.6
	6 H_2O	monomer	6.10E-04[116]	Δa_{WT}	26.0	15.8
				avg. Δa_{TW}	28.8	28.7

For the H beads, ethers (such as $CH_3OCH_2CH_2OCH_3$) appear to be the most suitable reference compounds. However, we face a shortage of reliable data on activities for the appropriate reference solutions. Groot and Rabone, [4, 27] fitted H-W parameters to LLE data for water-PEO solutions at higher temperatures, where PEO-water system undergoes a liquid-liquid separation. They obtained $\chi = 0.3$ and $\Delta a_{HW} = 1.3\ kT/R_c$. Here we opted to take short PEO oligomers (molecular weight = 400 g/mol) for reference compounds, because the data on water activity in PEO-water solutions were reported for a wide range of concentrations. [118-119] The procedure of a_{HW} parameter fitting is essentially the same as in ref.[83] We perform MC simulations with DPD models for PEO-water mixtures, where the overall bead densities are adjusted to yield bulk water pressures similarly to the dimer simulations described above. Figure 5-5 shows the activity of water in the PEO-water solution as a function of PEO mass fraction at 298.15 K for $R_c = 0.65$

nm. The activity of water $a_W(x)$ are calculated for different values of Δa_{HW} and compared with experimental data.[119] It is clear that the DPD model cannot describe water activity in PEO in the entire concentration range. This is not surprising taking in account the phase diagrams of DPD for polymers published by Wijmans and Smit. [24] Water activity in pure PEO (i.e. at infinite dilution) is reproduced at $\Delta a_{HW} = 4.5\ kT/R_c$. However, this would cause a liquid-liquid separation in water-rich systems (experimental PEO activities are not available in the literature). The best overall agreement is achieved with a much lower value of $\Delta a = 1.5\ kT/R_c$. Since water prevails in C_nE_m micelle coronas, we opted for this value which agrees well with the estimates of Groot and Rabone. [4] Δa_{HW} gives a very reasonable overall agreement between experimental and simulated dependences of water activity on composition for R_c = 0.65 nm and 0.71 nm. For R_c = 0.77 nm and 0.81 nm, MC statistics was very poor and we decided to use the same Δa_{HW} for all coarse-grained levels. For soluble fluids, $\chi(\Delta a)$ reference correlations generally show very weak dependence of coarse grained size. For tail and head interaction, the only available data also requires the extrapolation from a higher temperature. [120] We follow the mixing rule proposed by Groot and Rabone based on the chemical structure of ethylene oxide, and Δa_{TH} equals to one-third of Δa_{TW} (given in Table 5-4).

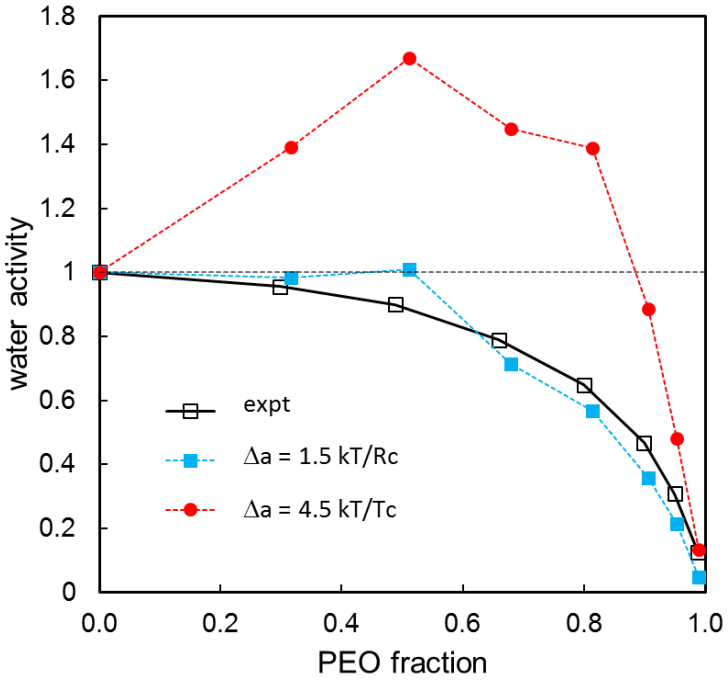

Figure 5-5. Water activity versus mass fraction of PEO in water-PEO mixture at 300 K. Experimental data (empty squares) is from Malcolm and Rowlinson.[119] Cyan squares are simulation results by using Δa_{HW} = 1.5, which produces the best overall agreement with the experiment. The red circles are simulation results by using Δa_{HW} = 4.5 (red circles), which has better agreement at the infinite dilute region of water (pure PEO).

Table 5-5. Critical micelle concentration (CMC) of C_nE_m surfactant with different tail (n) and head (m) length. Model 1 and model 2 refer to bonded parameters derived from atomistic MD simulations and approximately assigned, correspondingly. N_{ag} is the average aggregation number, and the aggregation pattern is exemplified with Figure 5-6.

Surfactant molecule		DPD model		Surfactant volume (%)	R_C (nm)
C_nE_m		T_xH_y			
n	m	x	y		
8	4	2	2	4%	0.71
8	6	2	3	4%	0.71
8	8	2	4	4%	0.71

10	5	2	2	2%	0.77
12	3	4	2	2%	0.65
12	3	2	1	2%	0.81
12	6	4	4	2%	0.65
12	6	2	2	2%	0.81
12	8	3	4	2%	0.71
12	9	4	6	2%	0.65
12	9	2	3	2%	0.81

$\log_{10}$ (CMC) [M]				Aggregation (method 1)	
method 1	method 2	relative error (%)	experiment [102]	N_{ag}	pattern
-1.96	-2.26	11%	-2.1	905	irregular[I]
-1.85	-2.19	9%	-2.01	539	irregular[II]
-1.74	-2.18	10%	-2	83	irregular[II]
-2.82	X	16%	-3.08	251	irregular[II]
-4.42	X	24%	-4	728	globular[III]
-3.97	X	63%	-4	471	globular[III]
-4.19	X	52%	-4.17	258	spherical&vesicular[IV]
-3.72	X	39%	-4.17	392	globular[III]
-3.18	-3.76	12%	-4	311	spheical & cylindrical[V]

-4.03	-3.8	13%	-4.1	111	spheical & cylindrical[V]
-3.6	-4.27	35%	-4.1	200	spheical & cylindrical[V]

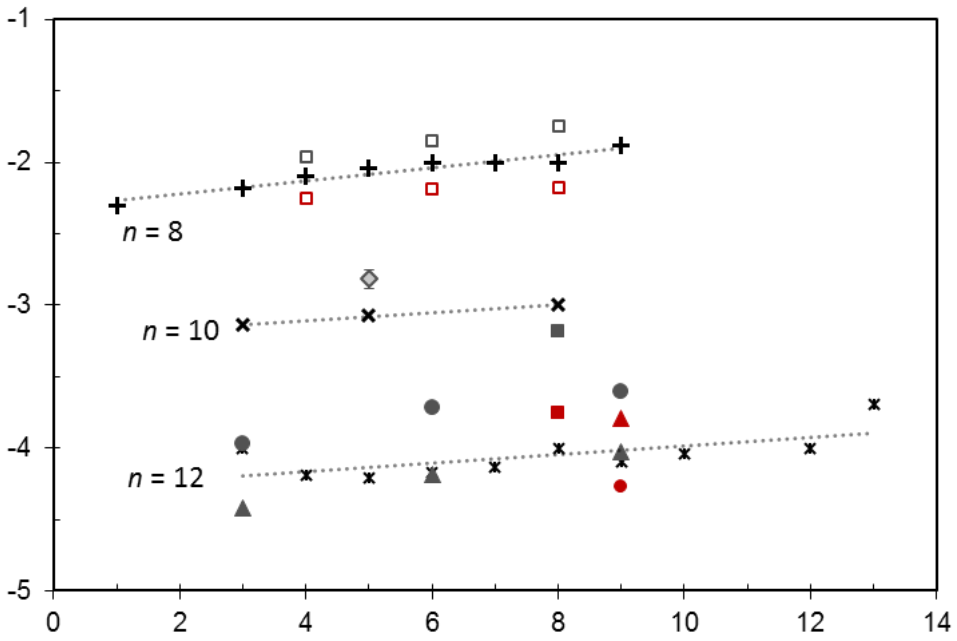

Figure 5-6. Critical micelle concentration (CMC) of C_nE_m obtained with DPD modeling and experiments. Each Different series show the dependence of CMC on hydrophilic segment length m for a given hydrophobic segment length *n*. Experimental data shown in black, with different symbols for different *n* (+ for *n* = 8, x for *n* = 10 and ж for *n* = 12). Lines are shows as guides for the eye. Simulated CMCs are shown in symbols: open symbols for *n* = 8, half-filled for *n* = 10, filled for *n* = 12) Symbol shape corresponds to the bead diameter (triangles for R_C = 0.65nm, squares for R_C = 0.71nm, diamonds for R_C = 0.77nm, circles for R_C = 0.81nm). Green symbols are used for the results obtained with the rigorous rigidity bonds, and brow symbols are used for the approximate rigidity model.

With the models and parameters described above, we calculate the CMC of select C_nE_m surfactants, using both models 1 and 2. DPD simulations of surfactant micellization are performed in the canonical NVT ensemble using LAMMPS. [106] Time steps is chosen as 0.01 $(kT/m)^{-1/2}R_c$. The total length of each simulation is 2 to 3 million steps depending on the box size. Periodic cubic box is sized from 32 to 64 R_c (Table 5-1) based on the targeted CMC estimated from the experiments. CMC is estimated from the average number of free surfactant in the solution, as the same way in our previous work. [1] This approximation is justified in ref. [81] Relative error is calculated from the deviation of CMC divide the average CMC. Surfactant molecules with tail bead overlapped are regarded as an aggregate, and the average aggregation numbers of all aggregates determine the aggregation number for the system, N_{ag}.

Table 5-5 summarizes the micellar properties obtained from the simulation compared with the available experimental data. CMC is mostly determined by the alkyl tail chain length *n*, and addition of one ethylene monomer decreases CMC by one order of magnitude. The influence of *m* on CMC is much weaker. Generally, CMC slowly increases with *m*. For the purpose of evaluation of the accuracy of the methods we selected a particular tail length *n* and performed simulations for several *m*, using, when possible, models with different bead size. $n = 8$ was the shortest hydrophobic block considered; we modeled C_8E_4, C_8E_6, and C_8E_8 surfactants using both models 1 and 2 with bead size R_C = 0.71 nm. As shown in Figure 5-6, simulated CMC increases as the hydrophilic block becomes longer, which qualitatively agree with experimental observation. The slight over-estimation is visible, but comparable to the statistical uncertainty of both simulations and experiments. Surprisingly, we can obtain also good accuracy without careful fitting of the

rigidity (model 2), as the approximate model gives very similar results but slightly underestimates the CMC.

For surfactants with longer hydrophobic tails $n = 12$, we present CMCs using model of different bead size. The statistical errors for these surfactants are much higher both in simulations and experiments, because lower free surfactant concentrations and large micelle size fluctuations. Model 1 with $R_c = 0.65$ nm showed a very good agreement with the experiments. With $R_c = 0.81$ nm, DPD model slightly overestimate the CMC, but the difference with experiment is still comparable to the error (in fact, almost exact agreement was obtained for $C_{12}E_3$). The reference compound for the hydrophobic tail is hexane in both cases (Table 1), but it is presented as a monomer for $R_c = 0.81$ nm and as a dimer for $R_c = 0.65$ nm. Our parameterization technique produces consistent results. A selected system $C_{12}E_9$ modeled by Model 2 at $R_c = 0.65$ nm and 0.81 nm also has good agreement with the experimental CMC. This indicates that although the representation on the molecule structure is not as accurate as in Model 1, the required hydrophobicity is compensated by the mismatch parameter during the calibration process. The only system where a serious discrepancy with the experiment is obtained is $C_{12}E_{8;}$ model 1 with $R_C = 0.71$ nm bead overestimates the CMC by the factor of 6.5. Overall the models show semi-quantitative to quantitative agreement with the experimental CMC values as shown in Figure 5-6. It should be stressed that the presented models are parameterized for different bead sizes, corresponding to various DPD model, with particular bond and rigidity, using diverse resources for mismatch parameters, yet still generate consistent results in CMC prediction.

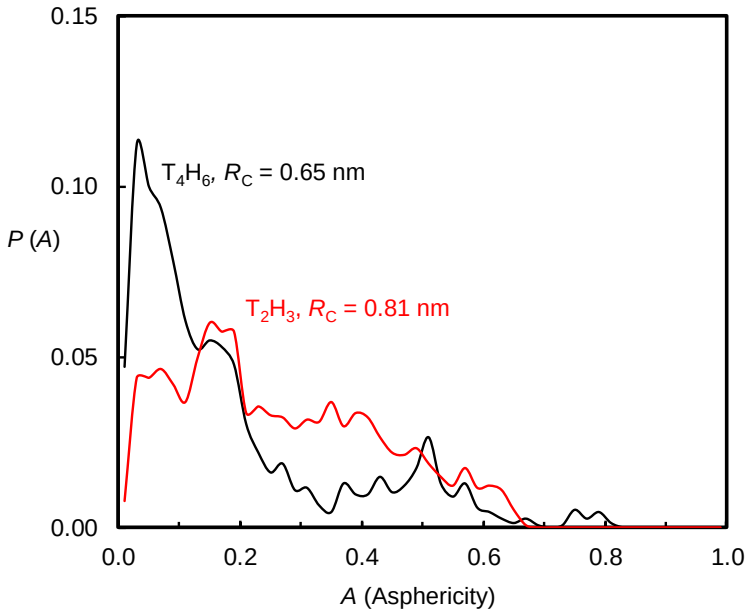

Figure 5-7. Normalized asphericity distribution of the micelles for model $C_{12}E_9$ surfactant. The finer model, T_4H_6 at R_C = 0.65 nm (black line), has more well-defined spherical micelles; the coarser model, T_2H_3 at R_C = 0.81 nm (red line), has micelles in more irregular shape and agglomeration between small micelles.

At the same time, we have found that the use of large R_c substantially alters micelle sizes and shapes even when CMC is correct. Figure 5-7 shows the micelle asphericity as observed in 2 vol% solution of $C_{12}E_9$ predicted with T_4H_6 model (R_c = 0.65 nm) and T_2H_3 model (R_c = 0.8 nm). Asphericity factor (A) is a generalized quantitative which measures the shape of micelle departure from spherical symmetry. [109] It is calculated as

$$A = \frac{1}{2R_g^4}\left[\left(R_1^2 - R_2^2\right) + \left(R_1^2 - R_3^2\right) + \left(R_3^2 - R_2^2\right)\right], \qquad (5\text{-}3)$$

where R_1^2, R_2^2, R_3^2 are eigenvalues of the gyration tensor that $S_{ij} = \frac{1}{N}\sum_{l=1}^{N}\left(S_{il} - S_i^{CM}\right)\left(S_{jl} - S_j^{CM}\right)$. S_i^{CM} stands for the center of mass of the micelle in

coordinate *i* (*i* denotes x, y, or z). Asphericity factor is 0 for perfectly spherical micelles and reaches 1 for perfect cylinders. As shown in Figure 5-7 (see also Figure 5-8a for visualization), the finer model (that is, with smaller R_c) predicts two pronounced peaks corresponding to spherical and elongated micelle. The average aggregation number is N_{ag} = 111, which agrees well with experimental value reported by Zulauf et al. (about 100 for $C_{12}E_8$ at 303 K). [121] The coarser model shows mostly elongated micelles with no characteristic values for *A*. The average aggregation number is about N_{ag} = 200, exceeding the experimental value. The explanation lies with the packing of the beads in the hydrophobic core: the bead size of the coarser model is comparable with the persistent length, and the chain therefore has no rigidity. It appears that despite the "softness" of DPD potentials which are unable to reproduce the atomistic details, the finer model with smaller and tightly spaced beads gives a better representation of the hydrophilic tail packing in the micelle core compared to the coarser model.

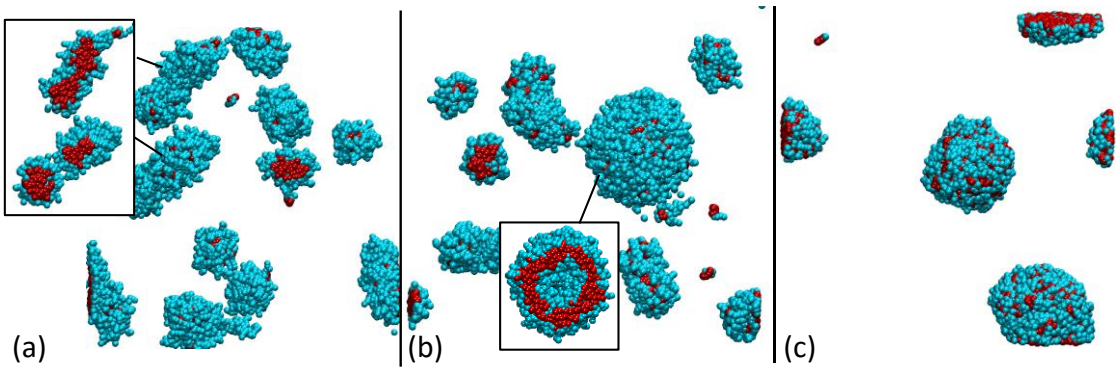

Figure 5-8. Characteristic aggregation patterns in solutions with 4 vol% C_nE_m surfactants simulated by DPD with R_C = 0.65nm bead size. Surfactant tail beads are in red, and head beads are in cyan. Water beads are not shown here. The zoomed figures show the inside structures of the aggregation. (a) C12E9: mixture a spherical and elongated micelles (b)

C12E6: mixture of spherical, elongated and core-shell micelles (c) C12E3: surfactant form core-shell micelles almost exclusive.

In general, the critical aggregation concentration (CAC) is underestimated by our models, especially for surfactants with shorter head segment, and prediction capability generally worsens as R_c increases. In experiments, the aggregation number generally decreases as the hydrophilic block becomes longer, due to the entropic repulsion between the hydrophilic chains. For the same hydrophobic segment length n = 12, this tendency is qualitatively reproduced in simulations, but it is much more pronounced compared to the experiments. (Table 5-5). Experimental N_{ag} increases from N_{ag} = 100 for $C_{12}E_8$ to N_{ag} = 150 for $C_{12}E_6$; in simulations with the rigorous fine model (R_C = 0.65 nm), N_{ag} increases from 111 and 258 respectively. The analysis of DPD configurations for $C_{12}E_6$ reveals a mixture of regular spherical micelles, elongated micelles and core micelles (Figure 5-8a). Core micelles are especially common in solutions of $C_{12}E_3$ (Figure 5-8c). Aggregation of micelles into bigger agglomerates was also observed for n = 8 with R_c = 0.71 nm. Although the micelles in C_8E_8 system are not of a well-defined spherical shape, they have a single hydrophobic core, and the aggregation number (N_{ag} = 83) agrees very reasonably with experimental value (N_{ag} = 72). [103] For the shorter molecule C_8E_4, the volumetric concentration ϕ = 0.04 at which the DPD simulations are performed is above the aggregation transition. The micelles are agglomerated via core-to-core contacts into larger agglomerates of complex irregular shapes with the formal N_{ag} reaching 905(!). In experiment, ϕ = 0.04 is below aggregation transition, with N_{ag} = 147. The approximate model is more prone to aggregation. The reason is constant bond length which is the same for hydrophilic and hydrophobic segments in the approximate model. This effectively shortens the head segments, reduces the entropic repulsion forces between the micelles and

makes them more prone to aggregation. Figure 5-9 shows the size distribution of the aggregates in the C_8E_8 system modeled by moth models 1 and 2. Model 1 with bonds fitted to the atomistic MD results predicts mostly spherical micelles with a well-defined peak. Some elongated micelles containing up to 350 molecules are also detected, but overall a very reasonable agreement with the experimental N_{ag} is observed. On the contrary, the approximate model 2 is prone to agglomeration. This results in several peaks (our box size and simulation length are not good enough to make a conclusion on the true micelle size distribution), and the resulting N_{ag} is overestimated as 128.

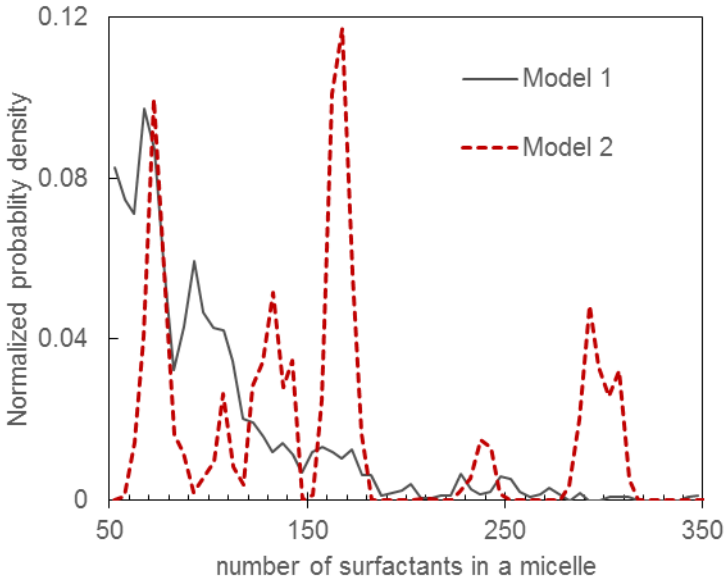

Figure 5-9. Normalized size distribution of the aggregate for C_8E_8 obtained with Model 1 (bonded terms are fitted to atomistic MD) and Model 2 (approximate bonded terms). Model 1 predicts smaller, mostly spherical micelles. With model 2 aggregates with larger sizes are also observed.

To conclude, we have thoroughly examined the techniques of parameterization of DPD models based on fitting the mismatch parameters to the infinite dilution activity coefficients of reference compounds. A reference compound closely resembles a fragment of a target molecule and is represented as a bead or a dimer of beads. A reliable parameterization technique should, in general, produce results more or less independent of the choice of coarse-graining level (that is the bead diameter) or the choice of reference compounds. In order to check the consistency of our parameterization strategy, we modeled aqueous solutions of C_nE_m surfactants that consist of hydrophobic alkane segment and hydrophilic PEO segment and are widely used in industry. We constructed DPD models of the C_nE_m surfactants for different length of each segment. The parameters for the nearest neighbor and second neighbor bonds which provide connectivity and rigidity, were matched to the results of atomistic simulations. We also employed an approximate model for the bonds, with the bond length and stiffness calculated from the number of flexible torsions between the bead centers. That approach is not universally applicable, but gave a very good agreement with experiments on CMC and N_{ag} of several chemically different surfactants. We parameterized the short-range conservative repulsion for different bead sizes from the IDAC of *n*-alkanes (from C_6 to C_{10}) in water and water in alkanes at room temperature. Water interactions with the hydrophilic segment were parameterized from the best match to experimental water activities in PEO-water mixtures of low molecular weight.

The models with different R_C parameterized with different reference alkanes generally show consistent results for CMC of C_nE_m surfactants. We correctly reproduced the increase of CMC with the hydrophilic block length and our most of our CMC values

agree (not without an exception) with the experimental data. This is the case for both rigorous and approximate model for bonds. For C_nE_m surfactants with longer hydrophilic segment we also obtained reasonable agreement on micelle size. The downside of the models is general underprediction of the CAC. In several systems we obtained various complex aggregates (such as cylindrical micelles, core shell micelles or irregular agglomerates), exceeding substantially the experimental N_{ag} values for the same surfactant concentrations. The predictions of N_{ag} generally worsens for short hydrophilic segments and larger bead sizes.

Overall, parameterization of DPD models from the activities appears to be a relatively straightforward and a reliable technique for parameterization of DPD models, and the accuracy of the models derived with this procedure as far as micellization of surfactants is concerned is very reasonable considering the general precision of DPD. The techniques does not require preliminary atomistic simulations, but does require calibration $\gamma(\Delta a)$ curves. They are obtained very easily for smaller bead sizes using standard codes for NVT simulations with Widom insertions. The accuracy of calculations of $\gamma(\Delta a)$ drastically declines with a, and advanced techniques may be needed when fluids of low compressibility are modelled with relatively large beads ($\sim R_c > 0.7$ nm).

Fitting molecule configuration from the atomistic level becomes relatively popular in the DPD simulation. The reason to do so is to preserve the geometry of molecule in the atomistic level in order to reverse mapping the morphologies obtained by DPD simulation. The relaxation time of the equilibrium in all-atom simulation is affordable in this case. The impact of the approach is the change of intra-molecule bead-bead distance and therefore

influence the contribution of hydrophobicity of the DPD molecule. Using the literature mismatch parameter correlation is no longer suitable, as the correlation was done at weak bonds with no chain rigidity. Inter-particle interaction need to be adjusted in order to reflect the correct bead-bead mismatch based on the DPD model's bond length and stiffness. This indicate the repulsion parameters need to be determined *ad hoc* and not transferable.

To resolve such issue, we proposed a simple method to determine DPD molecule constraints and mismatch parameter for each bead pair. [1] Based on our previous approach, the correlation between mismatch parameter and infinite dilution activity coefficient is established and extended to different coarse grained level from R_C = 0.65 to 0.81 nm. We use a variety of experimental solubility data of the reference compounds to determine the mismatch parameter of the corresponding bead type. At the same time, the effects of bond length is taken into account based on the configuration of DPD molecules fitted to the atomistic configurations. For the selected C_nE_m surfactant, we use hexadecane and PEO (molecular weight ~ 400) polymer melting as our reference system in order to obtain the bond and rigidity for our DPD model. Using only 1-2 and 1-3 FENE bond, the configuration of the whole polymer chain can be quantitatively reproduced. We examine our model by predicting micellar properties of C_nE_m at different tail and head length. Experimental observations of head length and tail length dependence on CMC are reproduced, and most of the CMC are semi-quantitatively reproduced by different coarse grained levels. The obtained aggregation number using models with sufficient chain rigidity also reproduces the experimental values quite well.

For comparison, we also use an approximate approach to determine constraints for coarse grained model. We found that our calibration still preserve the correct mismatch

between hydrophobic beads and water, which result in good agreement for CMC prediction. Nevertheless, the rigorous method still has privilege on description molecule configuration, and the qualitative prediction for micellization and aggregation number is better than that of the approximated method.

The limits of our approach is bound to the accuracy in constructing the calibration curves for $\gamma^{\infty}(\Delta a_{IJ})$. As the increase of like-bead repulsion parameters, the sampling process contains rare events which contributes significant deviation to average insertion energy. The reason is that DPD fluid becomes structured as a_{II} increases, creating an excluded region at bead-to-bead distance near zero. Although the coarse graining size in this work hasn't reached to the solidification limit (larger than 20 water per bead) discussed by Pivkin and Karniadakis, [122] the structured fluid for $R_C > 0.65$ nm has non-negligible uncertainty in chemical potential sampling. Further improvement of the sampling technique is desired in order to more accurately determine the mismatch parameter, which is crucial for some systems such as predicting micellization of surfactant with low CMC.

Section 6. Modeling proton transfer and dissociation in DPD

In this section, we introduce a mesoscale simulation framework that directly incorporates dissociation-association of proton-base complexes into the DPD forcefield. We specifically address the proton mobility in the water and protonation equilibria in the solution of acids by artificially mimicking Grotthuss-type mechanisms of formation and breakup of the proton-water and proton-anion (such as deprotonated acid) complexes. The proton is introduced as a separate charged bead that forms dissociable bonds with proton receptive base beads, such as water or deprotonated acid anions. The proton-base bonds are described by Morse potentials. When the proton established Morse bonds with two bases, they form an intermediate complex, and the proton is able to "hop" between the bases artificially mimicking the Grotthuss diffusion mechanism. We explain how the interaction of model proton with different bases and formation of the proton-base complexes are controlled by the Morse potential. We apply the proposed framework to modeling the proton mobility in water, and then study the equilibrium properties of dilute solutions of benzenesulfonic acid.

The system under consideration is presented as multicomponent mixture of beads with equal effective diameter R_C. Four types of beads are involved in simulations: deprotonated benzenesulfonic acid is represented by a dimer of bead C (C_5H_5) and bead S (CSO_3^-) connected by a harmonic bond. Proton (H^+) is modeled as a charged bead P described in Section III. Water bead W either includes a single H_2O molecule ($N_W = 1$; this model is used in simulations of proton mobility) or three H_2O molecules ($N_W = 3$). This bead size is chosen due to coarse graining of benzenesulfonic acid; dissociation of

which is considered in Section V. The system dynamics and equilibrium are studied by solving Newton equations of motions with pair-wise inter-bead forces given in Eq. 2-1.

In the model of benzenesulfonic acid, the hydrophobic benzene ring B and the hydrophilic sulfonate group C are connected by a harmonic bond. Long-range electrostatic forces $\mathbf{F}_{ij}^{(\mathbf{E})}$ between P and S beads representing charged species is implemented using the smeared charge approach. [123] Instead of point charges, the charge is modeled as a symmetric cloud around the bead center. Charge smearing avoids the divergence of electrostatic potential at $r_{ij} \rightarrow 0$ and allows for integration of the equations of motion with long time step that is the main advantage of DPD. In this work we use Slater type smearing model by Gonzales-Melchor et al. [123] where the charge distribution is $f(r) = \frac{qe}{\pi\lambda^3} \exp\left(\frac{-2r}{\lambda}\right)$, and λ is the effective smearing length chosen as 0.25 R_C to all charged beads. At long range, the electrostatic interaction of smeared charges (Eq. 2-2) reduces to the Coulomb potential and the standard Ewald summation [88] is used to account for the periodic boundary conditions. $\mathbf{F}_{ij}^{(M)}(\mathbf{r}_{ij})$ in Eq. 2-1 represents the Morse bond that accounts for the formation of dissociative complexes between proton bead P and base beads W and S. The details of the Morse bond implementation and parameterization are described below.

To introduce proton into the DPD framework, we employ a concept similar to that used in reactive MD. [124-126] We use a proton bead P, which bears +*e* positive charge and has the mass equaled $1/(18N_W)$ of the water bead mass. N_W is the number of water molecules in one water bead. P is allowed to form dissociable bonds with the proton-

receptive beads, which we call base beads, such as neutral water bead W and charged sulfonate (CSO_3^-) bead S. P bead experiences no short-range repulsion $\mathbf{F}^{(C)}$ with the bases, but may repel from other beads. The dissociable bonds are modeled by the Morse potential $\mathbf{U}_{ij}^{(M)}$ cut and shifted to zero at the cutoff distance r^M,

$$U_{ij}^{(M)}(r_{ij}) = K_{IJ}\left\{1-\exp\left[\alpha_{IJ}\left(r_{ij}-r_{ij}^0\right)\right]\right\}^2 - K_{IJ}\left\{1-\exp\left[\alpha_{IJ}\left(r_{ij}^M-r_{ij}^0\right)\right]\right\}^2 , \quad (6\text{-}3a)$$

and the Morse force is given by

$$\mathbf{F}_{ij}^{(M)}(\mathbf{r}_{ij}) = -2\alpha_{IJ}K_{IJ}\exp\left[\alpha_{IJ}\left(r_{ij}-r_{ij}^0\right)\right]\left\{1-\exp\left[\alpha_{PB}\left(r_{ij}-r_{ij}^0\right)\right]\right\}\mathbf{r}_{ij}/r_{ij} \text{ , at } r_{ij} < r_{ij}^M \quad (6\text{-}3b)$$

The Morse potential (Eq. 3a) has a minimum at $r_{ij} = r_{ij}^0$ and is characterized by the strength parameter K_{IJ} and effective steepness α_{IJ}. When $r_{ij} \approx r_{ij}^0$, the Morse potential is similar to the harmonic potential with effective stiffness K_{IJ}. Because the potential is cut and shifted, the overall depth does not equal to *K*, but rather depends on *K*, α and r^M and is denoted as E^M. This attractive force keeps the proton in the "associated" state, making it fluctuate around a particular base bead. The force is repulsive when $r_{ij} < r_{ij}^0$. Thus, the proton does not entirely "belong" to any host base, but the Morse interactions with overlapping base beads make its stand-alone existence apart from a base improbable especially in the densely packed DPD fluid.

Figure 6-1a illustrates the proton transfer between two water beads, W_1 and W_2, in the DPD model. Initially, the proton bead P is associated with W_1 by P-W_1 Morse bond. When another base W_2 appears within the P-W Morse potential cutoff, an intermediate complex W_1-P-W_2 is formed. The potential energy of the intermediate

shown in Figure 6-1b is the sum of the repulsion potential between water beads W_1 and W_2 and the two Morse potentials of P-W_1 and P-W_2 bonds. The potential energy profile has two minima along the reaction coordinate $r_{PW_1}/r_{W_1W_2}$ (P bead is assumed to be located on the line connecting the centers of water beads). The two minima are divided by a potential barrier associated with possible activated hopping of proton from W_1 to W_2. The minima merge when the distance between the water beads becomes shorter, effectively creating a single potential well. When W_1-W_2 distance increases again due to thermal fluctuations, the proton may either migrate from W_1 to W_2 or remains with W_1 after two water beads are separated later.

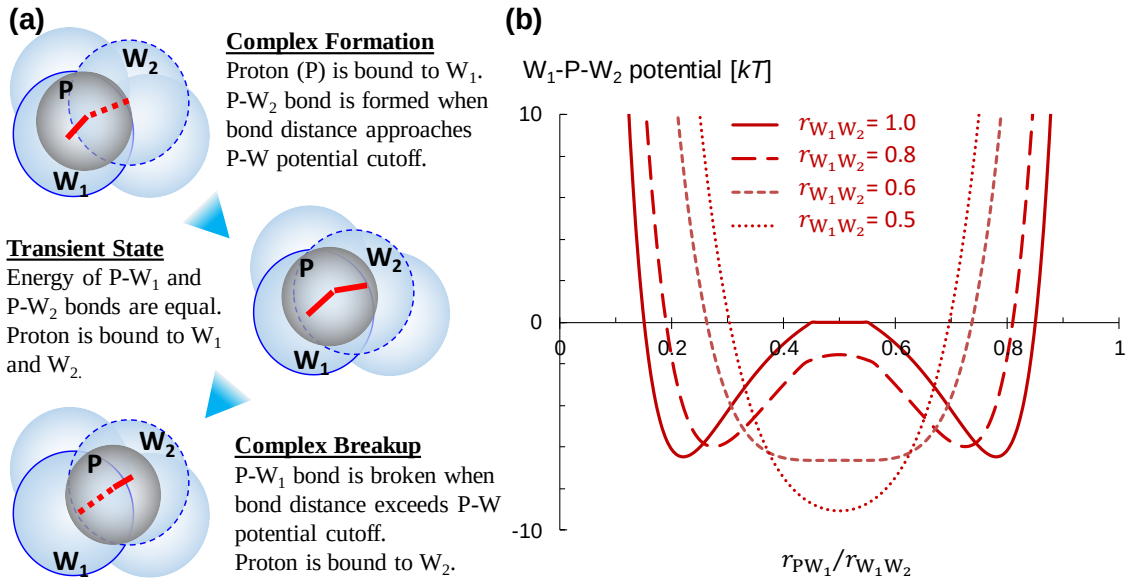

Figure 6-1. (a) Schematics of the coarse-grained model of the proton (P) transfer between two water beads W_1 to W_2 through the formation and breakup of an intermediate complex W_1-P-W_2. The radius of the P bead depicts the P-W Morse potential cutoff, and the red bars are effective P-W bonds (solid: strong, dashed: weak). (b) Potential energy of W_1-P-W_2 complex along the proton transfer reaction coordinate. The energy profile has two potential minima, and the transfer is associated with an energy barrier, crossing of which

mimics the proton hopping. The energy profiles are given for N_W=1, a_{WW}=23.4 kT/R_c, K_{PW} = 8.5, α_{PW} = 2, r_{PW}^0 = 0.22R_C =1 Å, and r_{PW}^M = 0.45R_C = 2 Å.

The same schematics holds for the proton transfer between any pair of base beads, which may be either neutral or charged. Neutral base beads may represent proton-accepting solvent molecules such as water, ammonia etc. (one bead can represent one or several solvent molecules). Charge base beads are commonly acid anions. In the latter case, the potential energy is augmented by the electrostatic attraction, which favors association. Therefore, the proposed model mimics proton transfer in a solvent bath and allows for equilibrium between protonated and deprotonated forms of acids in solutions. In the latter case, one of the water beads in Fig.6-1 should be replaced by the anion bead S. Below, we address both equilibrium and dynamic aspects of protonation.

Formation and breakup of intermediate complexes formed by proton P bead and two or more base beads allow one to mimic proton transfer from one base to another. By adjusting the depth and range of proton-base Morse potential, we can adjust the height of the potential barrier associated with the transfer of P bead between base beads, thus reproducing *proton dynamics*. Here, we consider a dilute aqueous solution, where the proton transport is controlled by proton transfer between water molecules (hopping mechanism) and diffusion of proton-water complexes (vehicular mechanism).

Simulations are performed as follows. One P bead is placed in the periodic cubic box of size 20 R_C filled with 24000 W beads (bead density ρR_C^3= 3). W beads interact with each other by standard DPD repulsion potentials. We consider two coarse-graining levels: N_w = 1 (that is, one DPD bead models a single water molecule) and N_w = 3 (three water molecules per bead). From the density and compressibility of water liquid at

ambient conditions, [4] for $N_w = 1$ we obtain $R_C = 4.45$ Å and $a_{WW} = 23.5\ kT/R_C$. For $N_W = 3$, $R_C = 6.45$ Å and $a_{WW} = 78\ kT/R_C$. W beads interact with the P bead only by the Morse potential. Since we deal with only very dilute solutions here, counterions are not considered and electrostatic interactions are not essential. The length of each simulation was 1 million steps and the reduced step length is 0.01τ, where τ is the dimensionless time unit in DPD. The self-diffusion coefficients of P and W beads are calculated in a standard manner from mean square displacements (MSD) via the Einstein relationship. Because of a limited ability of DPD to reproduce the dynamic properties of liquids, [23] we do not attempt to reproduce the self-diffusion coefficient of proton D_P *per se*, but rather its ratio to the self-diffusion coefficient of bulk water D_W determined in the same simulation, D_P/D_W. [127-128] Since the mobilities are compared to the experimental self-diffusion coefficients of water, we follow the literature approach [4] to convert DPD time unit τ into physical time. By matching MSD of W bead to the water self-diffusion coefficient (details are discussed in supporting information S2 of ref [89]), we obtain $\tau = 6.8$ ps for $N_W = 1$ and 10.4 ps for $N_W = 3$ with the simulation setup in this work. Note that for $N_W > 1$, the apparent diffusion coefficient calculated from the MSD of W beads is N_W times lower than the self-diffusion of water molecules as discussed in the ref. [4] Figure 6-2 shows the MSD of W bead (bulk region) and the P bead in the physical units.

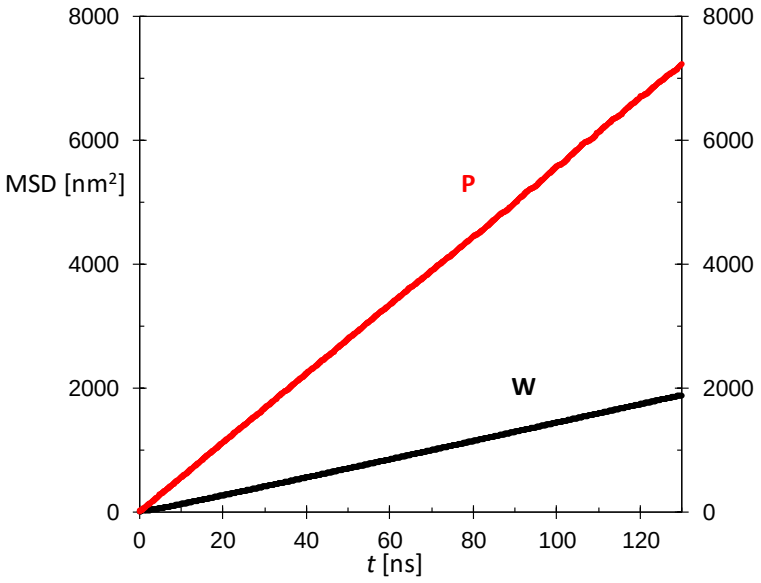

Figure 6-2. Mean square displacement (MSD, in nm^2) of proton bead (P) and bulk water bead (W) versus simulation time (ns). The ratio of the slopes between P and W in the figure is about 3.9. Parameters used here are the same as in Fig. 6-1(b).

At $N_W = 1$, W bead contains only one water molecule, P-W complex effectively corresponds to the hydronium ion H_3O^+, and W-P-W complex corresponds to the Zundel ion $H_5O_2^+$. Proton transfer in this case has a direct atomistic analogue: formation of Zundel complex from hydronium ion and water is followed by its breakup resulting in a successful or failed attempt of the proton transfer (Figure 6-1). On the atomistic modeling level, a similar scheme was implemented by Walbran et al. [129] As a consequence of coarse graining, the DPD model of hydronium has only one P bead, while a real hydronium ion has three equivalent protons, each of which can be involved in the formation of Zundel ion with a neighboring water molecule. The "fixed" nature of the proton bead does not allow larger complexes such as the Eigen ion $H_9O_4^+$ with $N_w = 1$. P bead moves in the solvent bath via a trajectory of interdigitating W-P ("hydronium") and

W-P-W ("Zundel") configurations. In W-P state, the proton, due to its low mass, experiences fast fluctuations around the hosting water bead before it forms a new Morse bond. We choose Morse parameters to reproduce (1) the number of W beads neighboring given P bead (that is, the W beads which simultaneously form Morse bonds with the same P bead) (2) P-W bond lifetime (3) experimental D_P/D_W ratio (proton self-diffusion in dilute solutions is about 4 times faster than that of bulk water at ambient conditions [127-128]).

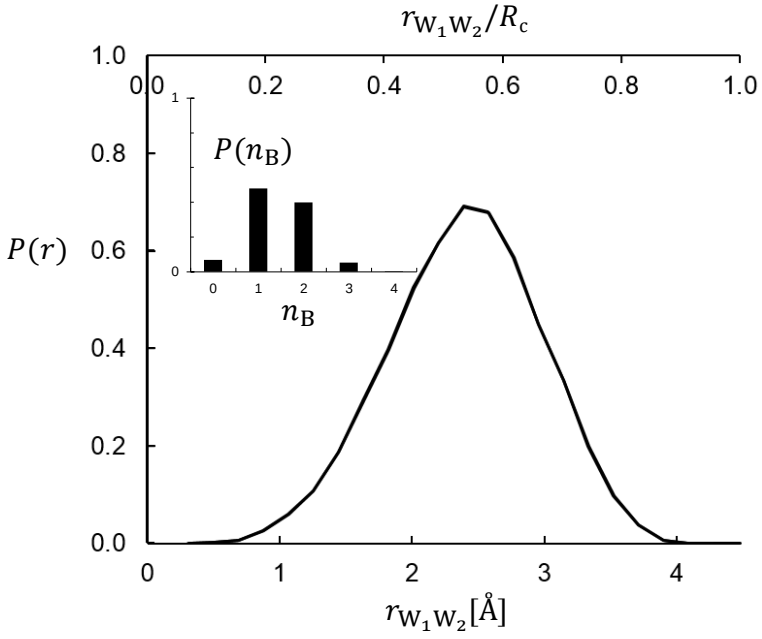

Figure 6-3. Distribution of distances between two beads W_1 and W_2 in W_1–P–W_2 complexes. Parameters used here are the same as in Fig. 6-1(b). The most probable distance of W_1 and W_2 is 2.4 Å, similar to the oxygen-oxygen distance in the Zundel complex. Insert shows the distribution of the number P-W bond.

In order to mimic the geometrical parameters of actual hydronium and Zundel complexes, we set the equilibrium P-W bonds distance at $r_{PW}^0 = 1\,\text{Å}$. The reasonable range for Morse cut-off r_{PW}^M is determined from the general definition of hydrogen bond, where

the donor-acceptor distance (in this case, it is the distance between two W beads connected to the same P bead) ranges from 2 to 4 Å. [130] This condition is satisfied only at relatively short r_{PW}^{M}; here we chose r_{PW}^{M} = 2Å. These parameters also give a reasonable estimate for the activation energy of the P bead transfer between the neighboring W beads. The characteristic distance between the nearest neighbor beads in the DPD fluid corresponds to the first maximum of the radial distribution function that is about 0.83 R_C. The barrier for the transition of the P bead from its current host to the neighboring one is 4.3 kT, which is very close to the experimental activation proton transfer activation energy in bulk water at room temperature (0.1 eV). [131-133] Figure 6-3 shows the distribution of distance between two W beads connected by Morse bonds to the same P bead at K_{PW} = 8.5 and α_{PW} = 2. The most probable distance between the bases W-P-W complex is approximately 2.5 Å. This is very close to the actual distance between two water oxygens in a Zundel complex and to the O−O distance in the water wire (2.5 to 2.6 Å) [128] and demonstrates the existence of Zundel-like structures in our DPD simulations. The distribution decays to zero at about 4 Å that as we noted above corresponds well to the actual maximum hydrogen bonds length in associating liquids. The insert on the figure shows the distribution of the number of bonds made by one proton at the same time. The proton mostly connected to one or two water beads, which corresponds to the hydronium-like and Zundel-like states. If r_{PW}^{M} increases, the P bead may establish the Morse bonds with multiple neighboring water beads, yet without identifiable hopping events.

Table 6-1. Parameters of DPD models. A. Morse parameters for P-W potential (Eq. 3), which reproduce experimental proton mobility ($D_P/D_W \sim 4$). E_M is the depth of the P-W Morse potential. B and C. Inter-bead repulsion and bond parameters for modeling benzenesulfonic acid solution, N_W=3.

A. Morse parameters						
Bead size	a_{WW}, kT/R_C	K_{PW},	r_{PW}^0, Å	α_{PW}	r_{PW}^M, Å	E_M [kT]
N_W=1, R_C = 4.48 Å	23.4	8.5	1	2	2.0	-1.2
N_W=3, R_C = 6.46 Å	78.5	16.0	0	1	3.9	-3.3
B. Short-range repulsion parameters, ($a_{IJ}R_C$)/kT						
N_W=3		W	S	C	P	
	W	78.5	78.5	91.2	0.0	
	S	78.5	78.5	78.5	0.0	
	C	91.2	78.5	78.5	91.2	
	P	0.0	0.0	91.2	0.0	
C. Bond parameters						
	Bond/type	K	r^0, Å	α	r^M, Å	
	C-S (harmonic)	200.0	5.2	–	–	
	P-W (Morse)	16.0	0.0	1	3.9	-3.3

	P-S (Morse)	18.5	2.2	2	4.2	-4.2

Once r_{PW}^{M} is fixed, the strength of the P-W Morse bond (that is, the actual depth of the Morse potential) determines the lifetime of the hydronium-like and Zundel-like configurations, and therefore, determines the hopping frequency and self-diffusion. For cut-and-shifted version of the Morse potential, the overall depth E_M determines the entire attractive part of the potential (this shortcoming of the chosen type of the dissociating bond is discussed in Section V of ref [89]). The deeper the P-W Morse potential well, the slower P bead moves in the water bath. By scanning the overall depths from –0.5 kT to –50 kT, we found that the sought proton mobility is achieved when $E^M \approx -1.2$. To impose a stronger repulsion between the P and W beads at short distances, we chose maximum value of the steepness parameter α in Eq. 6-3 that does not compromise the computational efficiency. The parameters employed in this work are given in Table 6-1.

With these parameters, we obtained the proton mobility that exceeds the water mobility by the factor of $D_P/D_W = 3.8$, which is very close to the experimental data. The P bead moves in the W bath via a series of "hops". We characterize the frequency of hopping events using a "hosting time" t_h. The hosting time is a period between two consecutive hopping events. The hosting time for our DPD model is about 2.6 ps, which agrees very reasonably to the experimental data of 2.0 ps. The average lifetime of a hydronium-like formation is 1.7 ps, and for the Zundel-like formation it is 1.4 ps.

A coarser representation of water (N_W=3) results in a higher repulsion parameter a_{WW}, more structured fluid, and lower degree of overlap between water beads. The proton is introduced similarly to the monomolecular model with N_W=1; P bead that forms dissociable Morse bonds to W bead and can be transfer between them according to the schematics shown in Fig. 6-1. The main difference is that the actual proton modeled by P bead can be transferred between the water molecules that effectively belong to the same W bead. Therefore, there is no geometrical reason to introduce Morse repulsion between W and P beads. We decided to set the equilibrium P-W distance r_{PW}^0 in Eq. 6-3 to zero. The removal of the repulsion part of the Morse potential at $r_{PW} < r_{PW}^0$ allows P to reside near the center of its host base. Therefore, the distance between the minima of potential energy for an individual act of proton transfer (Figure 6-1) increases, the number of Morse bonds formed concurrently by the same P bead decreases, which leads to slower transfer rates. However, the increasing ratio of W and P bead weight creates a more distinct velocity differences of P bead and W bead, requiring a stiffer P-W potential to reach the target D_P/D_W ratio. The dependence of overall proton mobility and P-W parameters follows the same trend as in the monomolecular model discussed above. The P-W potential, which reproduces proton mobility in bulk water, is used in the following section. The potential parameters obtained following the same approach as for the monomolecular model are listed in Table 6-1.

As a representative example, we chose benzenesulfonic acid aqueous solution, because polymers containing phenylsulfonic acid groups are commonly used in proton-exchange membranes, the systems of a particular practical interest. Analogy between the atomistic and DPD models is shown in Figure 6-4.

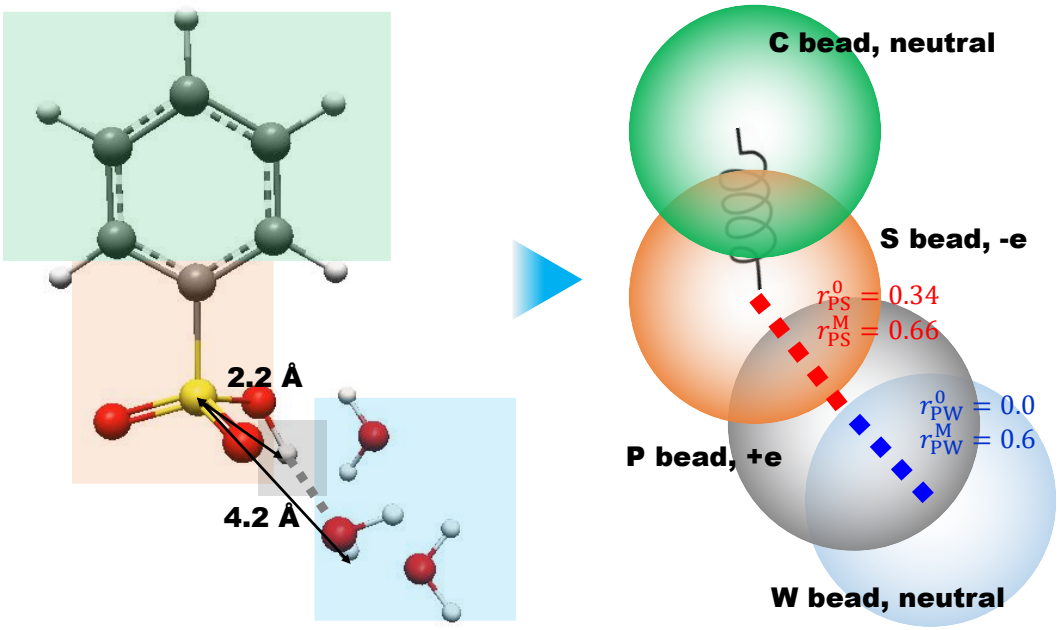

Figure 6-4. Coarse-grained representation of benzenesulfonic acid (sulfur in yellow, oxygen in red). Colored blocks on the atomistic model denote the fragments that constitute the respective DPD beads. The coarse-graining level corresponds to three water molecules per bead. C-S dimer represents the deprotonated acid ion. The equilibrium distance and the cutoff of the associative harmonic potential between beads S and P are chosen from the *ab-initio* calculations.

The coarse-graining level of $N_W = 3$ and $R_C = 6.65$ Å is dictated by the chosen dissection of the benzenesulfonate anion ($C_6H_5SO_3^-$) into two beads of the comparable size. It should be noted that the presence of dissociating species other than small solvent molecules limits the choice of N_w. In particular, $N_w = 4$ would be a convenient coarse graining level for water, since the protonated water bead could effectively represents an Eigen ion. However, acid groups (such as sulfonate) are typically rather small. If such a group were included in a bigger bead, the same bead would have to contain hydrophobic fragments or associated water that might be undesirable. The coarse graining level chosen here ($N_w = 3$) is very common in DPD simulations of surfactants. [4] According to our

calculation with the COSMO model [134] performed with PQS software, [135] the volume of the benzenesulfonate anion is about six times as large as that of a water molecule (Supporting Information, Section S3 of ref [89]). Therefore, we model benzenesulfonate as a dimer composed of a neutral hydrophobic C bead and a negatively charged hydrophilic S base bead. The beads are connected by a stiff harmonic bond at equilibrium length equals to 0.8 R_C with bond stiffness $K_B = 200\ kT/R_C^2$. Following the standard DPD formulation, [4] the intra-component repulsion parameter $a_{II} = 78.5\ kT/R_C$ was assigned for all bead types. Inter-component parameters between acid and water play no significant role in dilute solutions (0.01 to 0.09 M) considered here, since acid molecules are well dissolved in the solution with no aggregation. Parameter for hydrophobic component $a_{CW} = 91.2\ kT/R_C$ was estimated from benzene solubility in water using the approach suggested in our previous work. [136] Parameter a_{SW} for the hydrophilic component was set to zero.

Sulfur atom is the geometric center of the CSO_3^- fragment represented by the S bead. Naturally, the S-H distance observed in benzenesulfonic acid molecule serves as the equilibrium distance r_{PS}^0. The interaction between sulfonate and proton may be reduced to electrostatic attraction if the proton is separated from the anion by water oxygen. This distance was chosen as the Morse bond cutoff. It was estimated with the DFT optimization of C_6H_5-SO_3H•$3H_2O$ clusters described in the Supporting information Section S3 of ref [89] as $r_{PS}^M = 0.66\ R_C$.

The P bead experienced no short-range repulsion from W and A beads ($a_{PW} = a_{PS} = 0$), however, repulsion parameter $a_{CP} = 91.2kT/R_C$ was assigned in order to avoid

proton bead from overlapping with the benzene ring. P bead interacts with the acid anion S bead via electrostatic interaction as well as via the Morse bond, provided $r_{PS} < r_{PS}^{M}$. The existence of the Morse bond serves as a criterion that P and S beads are associated. The equilibrium and cutoff distance parameters for P-S Morse bonds were assigned from geometric considerations based on the distance from S atom to associate proton and to the H atom on the associated water molecule (See Supporting Information Table S3 of ref [89]). At the same time, P bead may form Morse bonds with the surrounding water beads W. The parameters of P-W Morse potential listed in Table 1 were determined to provide quantitative agreement with the experimental proton mobility, as described in the previous section.

Dissociation of benzenesulfonic acid is presented as a reaction: CSP + W $\leftrightarrow$ CS + WP, characterized by the equilibrium constant $K_a \approx [CS][WP]/[CSP]$. This approximation holds for dilute solutions, where the dependence of activity coefficients on concentration may be neglected. Experimental dissociation constant K_a for benzenesulfonic acid is 0.2. The dependence of the degree of dissociation on the total concentration of sulfonate may be calculated as Eq. 4 derived in Supporting Information Section S4 of ref [89].

$$\beta = \frac{[CS]}{[CSP]_0} = \left[-K_a + \sqrt{K_a^2 + 4K_a[CSP]_0} \right] \Big/ 2[CSP]_0 \qquad (6\text{-}4)$$

The DPD simulations of protonation equilibrium were performed in 30×30×30 R_C^3 simulation box containing the total of 81,000 DPD beads over 500,000 DPD time steps of 0.01 $(kT/m)^{-1/2}R_C$. After 100,000 steps for equilibration, the degree of

dissociation was calculated as a fraction of S beads that formed no Morse bonds with any of the P beads at given moment, i.e. $r_{PS} > r_{PS}^{M} = 4.2$ Å. Noteworthy, the electrostatic interactions alone are insufficient for describing CS protonation: the calculated degrees of dissociation was close to 1 in all systems with $K_{PS} = 0$. Although the electrostatics with the short decay length (Eq. 6-2) provides -4 *kT* when P and S beads are fully overlapped (integral of Eq. 6-2 at $r = 0$), P bead prefers being hosted by W bead (-3.3 *kT*), which is repelled from S bead. Temporary association of P and S beads is due to the rarely happened overlap of S bead with P associated W bead.

Intuitively, the stronger is the P-S potential, which results from higher values of α_{PS} and K_{PS}, more P beads are associated with S beads for longer times that implies a lower degree of dissociation β. We characterize the P-S potential by reproducing the experimentally derived degree of dissociation β at the given initial acid concentration at 0.05 M, or about 82.5% as calculated by Eq. 6-4. It is found that with the P-S potential well of $E_M = -4.2\ kT$, the simulated degree with dissociation agrees well with the experimental derived value. In order to examine whether the obtained P-S potential properly characterizes the proton equilibrium between the S bead and the surrounding W beads, we predict the degree of dissociation at several different concentrations in the dilute region without future adjustment of P-S parameters. As the concentration of sulfonate in the system increases, the degree of dissociation naturally declines. Figure 6-5 shows the dependence of β on the total molarity using the parameters obtained at 0.05 M ($\alpha_{PS} = 2$ and $K_{PS} = 18.5$), which gives practically exact agreement with Eq. 6-4 for the entire concentration range up to 0.1 M. The validity of Eq. 6-4 is questionable at higher

concentrations as it implies that the water concentration remains constant. Good agreement between the theoretical and simulated degrees of dissociation confirms that the proposed model mimics the essence of the process. The model can be parameterized from the dissociation constant only and then applied at different concentrations. The reaction constant is mostly determined by the P-S potential well. The value of $E^{M} = -4.2\ kT$ used in this particular example, can be obtained by different combinations of α_{PS} and K_{PS}, the potential profile and influence on the degree of dissociation are discussed in Supporting Information Section S5 of ref [89].

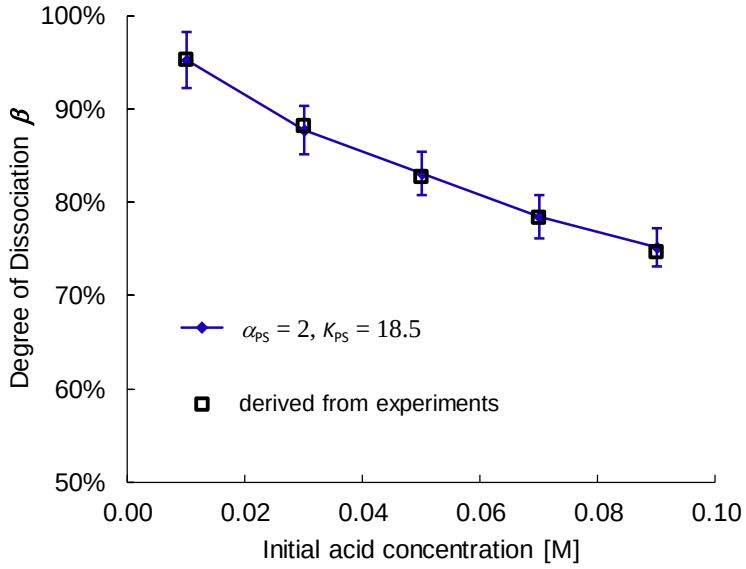

Figure 6-5. Degree of dissociation versus molarity of 0.01 to 0.1 M. Experimentally derived values are marked by squares. Lines are obtained from the DPD simulation with the Morse potential parameters fitted to reproduce the degree of dissociation at 0.05 M.

To conclude, we develop a coarse-grained model of the proton transfer that allows for the incorporation of protonating compounds directly into the DPD forcefield. We introduce a new bead type that represents the proton that can be associated with base

beads. The proton bead P interacts with base beads by a dissociative, short-range Morse-type bonds. Base beads represent either neutral solvent (water W) or charged acid anions (sulphonate S). Protonation-deprotonation of bases is effectively modeled as a reversible reaction that occurs naturally in the course of DPD simulation. In a close analogy with the atomistic representation of protonation, the reaction proceeds via formation of an intermediate complex B_1-P-B_2 (B = S or W) where proton is simultaneously bound with two base beads. An unavoidable breakup of the intermediate complex results in a successful or failed attempt of the proton transfer between the bases. In case, when the base beads represent individual water molecules, the intermediate complex W-P-W effectively mimics Zundel ion. With a proper choice of the Morse potential parameters, we are able to reproduce the O-O and O-H distances in the Zundel complex in DPD simulations. The proton motion is DPD simulation consists of a sequence of distinct transfers between the neighboring base beads, imitating the Grotthuss mechanism of proton diffusion.

The short-range dissociable potentials preserve computational efficiency of DPD and may be easily implemented in standard DPD codes. In this work, we used DL_MESO, an openly distributed code that allows for the implementation of smeared charges. The Morse potential that is cut and shifted within 1 bead diameter does not compromised the computational advantages of DPD simulations. In order to monitor the detailed transfer of P beads, the physical unit of simulation time used in this work is relatively smaller than in regular DPD simulations, [4] that causes an insignificant increase of computational costs.

The proposed model successfully describes the equilibrium between dissociated and non-dissociated forms of a common organic acid of a moderate strength drawing on the example of benzenesulfonic acid. The potential parameters are and quantitatively predict the degree of dissociation at several concentrations in dilute and semi-dilute solutions. At the same time, the model is capable of reproducing the experimental ratio of proton and water self-diffusion coefficients, as well as the proton hopping frequency at ambient conditions with different degrees of coarse graining. We specifically studied the models with different bead sizes corresponding to one and three water molecules per bead.

Incorporation of dissociable bonds expands the DPD method to a new class of systems with chemical equilibria. The proposed model can be suitable for modeling proton conductivity and ion-exchange reactions in solid electrolyte membranes like Nafion, for example, by embedding it directly into explicit charge DPD models for Nafion segregation (e.g. ref. [7]). Certain difficulties may be expected in applying this model to complex environments. For example, the activation energy for proton transfer in hydrated polyelectrolytes may differ substantially from that in the water bulk [131] and depends on fine details of the structure, such as the arrangement of surrounding anions [132, 137-138]. Such fine features are difficult to reproduce in DPD. On the other hand, a very reasonable agreement with experiment was obtained in recent simulations of Jorn and Voth , [139] where proton diffusion in Nafion was modeled implicitly in a segregated structure obtained by DPD and electrostatic field created by the sulfonate groups. In this paper, we demonstrate the capabilities of the proposed model on a particular simple protonation reaction, however, a similar scheme can be elaborated for other equilibrium

reactions sensitive to the solvent composition, which involve ion dissociation and complexation.

Section 7. Modeling sPS PEM using DPD

In this section, we present a direct DPD study of proton diffusion in a hydrated polyelectrolye. The basic approach to incorporation of proton into DPD simulations was suggested by us recently [89]. There, proton was modelled as a special P-bead; the protonating compounds (e.g. water and acid anions) are modelled as proton-receptive base beads, and they interact with P-beads by dissociative Morse potential. The calibration of is performed by matching simulated proton mobility in bulk water and dissociation degree in dilute solutions of reference acids to the experimental data. Now we extend our approach onto PEM. We have chosen sulfonated polystyrene (sPS) as a characteristic example. sPS is a polymer of a significant practical importance, since various sPS based materials (especially block copolymers of sPS and polyolefins) are used in proton exchange fuel cells; their industrial potential is propped by a low cost, as they are generally cheaper that perfluorinated PEM of Nafion type. In sPS-polyolefin block copolymers, water-swollen sPS forms the hydrophilic domain. But the hydrophilic domain itself is segregated onto the aqueous subphase formed by the sulfonic acid groups surrounded by water and protons and the hydrophobic alkylbenzene subphase. The segregation inside hydrated sPS was observed both experimentally and in simulations. [84-86] The morphology is irregular and depends on the level of sulfonation, and the scale of segregation is believed to be relatively small. Small size of the hydrophilic channels, tangible dissociation constant of the acid group, and the ability to vary the sulfonation level substantially, make sPS an ideal system for examining the advantages and limitations of our DPD approach.

Figure 7-1 illustrates the coarse grained model of sulfonated polystyrene. A monomer contains an ethyl benzene fragment and a sulfonic acid group if the monomer is

sulfonated. Evaluating the volume of each functional group using from the standard Bondi tables used in UNIFAC group contribution model, we found that an ethylbenzene can be modeled as a dimer of two hydrophobic beads (B-C), and the deprotonated sulfonated group is modeled as a single S bead (the volume calculations are given in Supporting Information, Section S1). The B bead represents four aromatic carbons of the benzene ring, and each C bead contains two aromatic carbons and two aliphatic skeleton carbons (exact mapping of atoms onto the beads is shown in Supporting Information, Section S1). The S beads contains the sulfur and three oxygens, making the CG mapping consistently has four heavy atoms in one DPD bead. A solvent bead W represents three water molecules. The corresponding bead size is 0.65 nm, estimated from the bulk density of liquid water. [4] sPS in this work is represented by oligomers composed of 20 monomers each. A fraction of monomers in each oligomer is sulfonated in para position according to the sulfonation level, which is varied from 10% to 40%. The sulfonated monomers are uniformly distributed among the chain, as shown in Figure 1b. Each proton H^+ is modeled separately as a single bead P, according to ref [89].

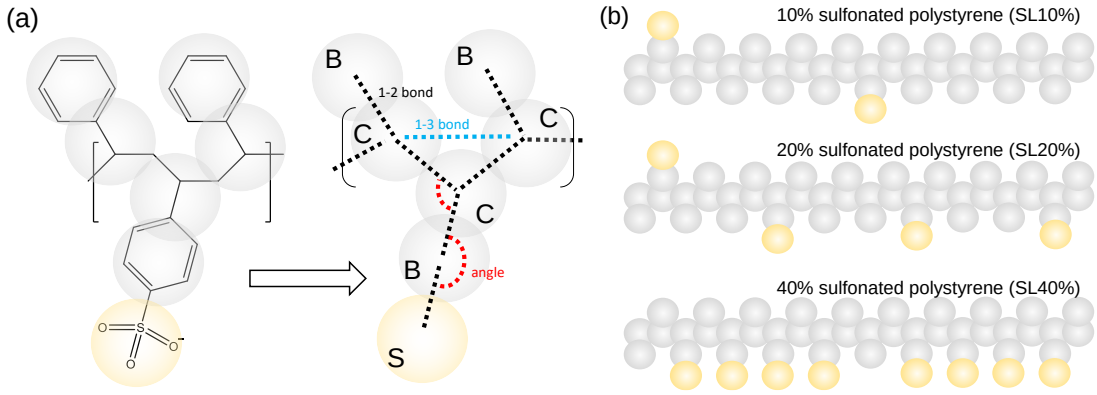

Figure 7-1. (a) Chemical structure of partially sulfonated polystyrene (sPS), and the corresponding DPD model. The beads are connected by 1-2 body bond (dashed black lines), and 1-3 body bonds (dashed blue line) provides chain rigidity. Rigidity on side chain are controlled by harmonic angle (dashed red curves). Details of these constraints are discussed in Section 2.4. (b) sPS at different sulfonation level, denoted as vol% sPS. For example, 10% sPS means there are 2 sulfonate groups in a chain of 20 monomers.

The employed DPD scheme is introduced in Section 2. All beads are assigned an equal effective diameter R_c= 0.65nm. Following the standard approach to DPD simulations of self-assembly, [23] the intra-component repulsion parameters a_{II} between beads of the same type are set equal, irrespective to the type. The beads are tightly packed the reduced density of ρR_c^3=3, common in DPD simulations. [23] Drag coefficient is assumed γ = 4.5, a common value used in DPD simulations of water. [23] The chain beads are connected by FENE bonds with the nearest neighbor (1-2) bonds, as well as with the second neighbor (1-3) bonds in order to control the flexibility of the molecule. Because the conformation of the polymer is important for segregation structure of hydrated sPS, while the polymer is relatively complex (compared to linear chains we considered earlier) and contains very rigid fragments, we also introduced standard harmonic angle potentials between certain pairs of nearest neighbor bonds as shown in Figure 7-1b. The electrostatic interactions are modeled using the smeared charge approach with the Slater-type charge density distribution with an exponential decay. [76] The standard Ewald summation [88] is used to account for long-range electrostatics. The choice of the smearing radius $\lambda = 0.25R_c$ for all charged beads was made on technical reasons (Supporting Information to ref [89], Section S2). Similar suggestions can be found in recent DPD studies. [78, 80, 90]. Morse potential $\mathbf{F}_{ij}^{(M)}(\mathbf{r}_{ij})$ is applied between the proton bead P and bases that are water bead W and

sulfonate bead S. The P—base interactions are modelled by the Morse potential, cut and shifted at cutoff radius r^M, as the same fashion in Section 6.

Following the most common DPD implementation, intracomponent repulsion parameters a_{II} are assume equal for all bead types I and determined from the compressibility of water, which gives $a_{II} = 78.5\ kT/R_c$ for $R_c = 0.65$ nm. [4, 89] The intercomponent repulsion parameters are mapped to the infinite dilution activity coefficient in solutions of reference compounds for different bead types. [1]

We assume that hydrophobic beads B and C have the same short-range repulsion parameters with hydrophilic bead types (that is, $a_{BI} = a_{CI}$, where I = P,W, or S.). In order to estimate a_{BW}, we choose ethylbenzene as a reference compound for hydrocarbon skeleton, and (similarly to ref [1]) coarse-grain it as a symmetric dimer BB. The bond length in the BB dimer is equal to the length of B-C bond in the coarse grained sPS model and is found from energy minimized structures of small sPS fragments (see Table 7-1). Water was presented as a bath of monomer beads W; each of them models 3 water molecules. We performed standard canonical MC simulations with Widom trial particle insertions, and determined the calibration dependences γ^∞ (a_{WB}) for W beads in BB dimer bath, as well as BB dimers in the W bead bath. The bead density in the W bath is $\rho_W = 3R_c^{-3}$; the density of BB bath is ρ_B to have the same pressure as in liquid DPD water. [30]. Using this procedure, we obtain the calibration correlations between γ^∞ and $\Delta a_{WB} = a_{WB} - a_{WW}$. They are similar to those reported for other compounds [1] and are given in Supporting Information (section S4 of ref [140]). By interpolating the γ^∞ values for ethylbenzene and water, we find a_{WB} values. γ^∞ for ethylbenzene and water $\ln \gamma^\infty = 12.76$ is calculated from the experimental

solubility (169 mg/L), and $\ln \gamma^{\infty} = 6.36$ for water in ethylbenzene is calculated using COSMO-RS thermodynamic model. [141] The resulting values of Δa are 21.3 kT/R_c and 26.3 kT/R_c correspondingly, and we use the average Δa=23 kT/R_c, therefore $a_{WB} = a_{WC} = 102.3kT/R_c$.

S bead that models the sulphonate anion is hydrophilic; because parameterization techniques for ionic species are still poorly developed, we applied $a_{SW} = a_{WW}$ and imposed strong repulsion between S and hydrocarbon beads. (it is worth noting that $a_{SW} < a_{WW}$ is often used when electrostatic interactions are implicitly accounted for [8]). P bead experienced no short-range repulsion from the bases or other P beads but repelled from B and C beads.

Table 7-1. Parameters of DPD model for hydrated sPS.

A. Morse interaction between P bead and bases				
Bead pair	$K_{PW,}$	α_{PW}	r_{PW}^{0} (R_C)	r_{PW}^{M} (R_C)
P-W	16.0	1	0	0.60
P-S	18.5	2	0.34	0.66
B. Short-range repulsion parameters, ($a_{IJ}R_C$)/kT				
bead J \ bead I	W	S	C & B	P
W	78.5	78.5	102.3	0.0
S	78.5	78.5	78.5	0.0
C & B	102.3	78.5	78.5	102.3
P	0.0	0.0	102.3	0.0
C. Bonds				

Bond type	forcefield type	K (kT/R_c^2)	r_0 (R_C) or θ_0	r_m (R_C)
C-C	1-2 FENE	800.0	0.50	2.0
C-(C)-C [(a)]	1-3 FENE	130.0	0.59	3.0
B-C	1-2 harmonic	800.0	0.35	∞
S-B	1-2 harmonic	800.0	0.43	∞
D. Angles				
Angle type	forcefield type	K (kT/ rad^2)	θ_0 (rad.)	
S-B-C	Harmonic	500.0	180^o	
B-C-C	Harmonic	40.0	90^o	

[(a)] second-neighbor bond between two C beads separated by another C bead

The parameterization of bonded forcefield terms was performed similarly to Section 5. We performed MD simulation of 10-unit oligomer of 100% sulfonated sPS in water using forcefields from refs [85-86] and calculated the distribution of distances between the centers of mass of polymer fragments corresponding to the different beads (see Figure 7-1). The distributions are shown in Figure 2. We fit the DPD bonded parameters to achieve the best agreement between MD distributions of the distances between the fragments and DPD distributions of distances between the corresponding beads. Unlike previous simulations of linear chain molecules [1, 84], the conformations of sPS are quite complex. The overall rigidity of the aliphatic skeleton is reproduced well (Figure 7-2a). However, the distribution of 1-3 and 1-4 distances (that is, distances between two C beads separated by one or two other C beads) are multi-modal and it is difficult to capture the details of molecular structure by simple DPD potentials. For the same reason, the most probable

distance between second neighbor B and C beads (separated by one C bead) is 0.5Å shorter in the DPD model compared to the MD results (Figure 7-2b). Table 7-1 contains the final parameters that yield the best overall agreement between the DPD and MD distance distributions.

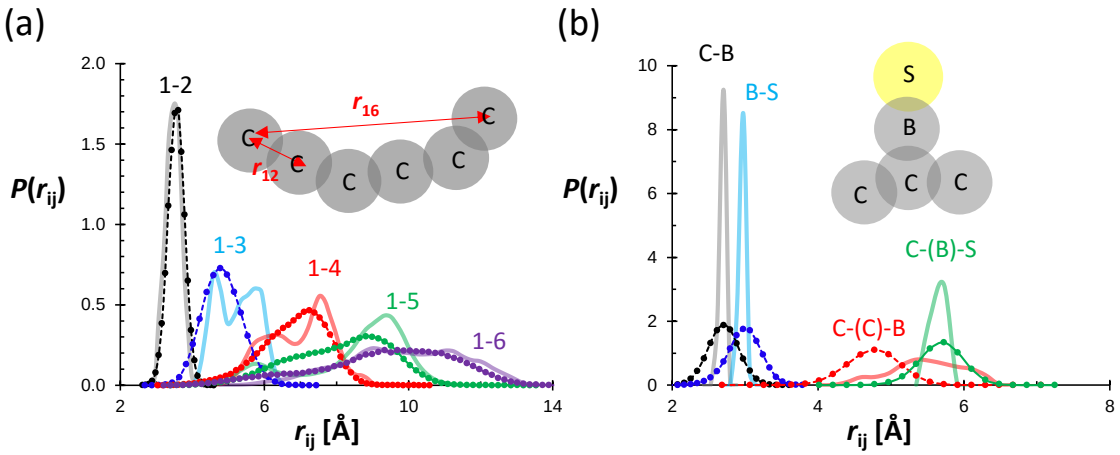

Figure 7-2. Intramolecular distance distribution function $P(r_{ij})$ for the distance between bead i and bead j, r_{ij}. (a) Distribution of distances between backbone C beads from closest neighbor distance r_{12} to C beads separated by 5 other C beads r_{16}. Solid lines are from MD simulation, and lines with symbols are from DPD simulation. (b) Distribution distances between of backbone C beads and sidechain B and S beads. For the second neighbor 1-3 distances brackets denote the bead that separates the pair of beads in consideration.

Using the forcefield described above, we perform several DPD simulations of hydrated sPS. We considered sulfonation levels of 10%, 20%, and 40%. From water sorption data in pure sPS [142] and sPS-polyolefin block copolymers [143] (water sorption in the hydrophobic block was neglected) we estimated the correlation between sulfonation level and the saturated hydration (that is, the amount of water absorbed by the polymer in contact with the saturated water vapor): HL = 1.44 * SL – 3.42, where HL (hydration level) is mass of the sorbed water related to the mass of the dry polymer, and SL (sulfonation

level) is the fraction of sulfonated monomer. For each sulfonation level, we modelled several systems at different hydration, ranging from half of the saturated hydration to fully saturated sPS. Similarly to ref, the density of each system was adjusted to give the pressure equal to the pressure of pure coarse-grained water. All systems modelled are listed in Table 2. DPD simulation details are described in Supporting Information (Section S5 of ref [140]).

Table 7-2. System information and simulation results. Abbreviations: SL, sulfonation level; HL, hydration level; λ, number of water molecule per sulfonate group; N_{sPS}, N_W, N_P are number of sPS molecules, W beads, and P beads; time: simulation time in ns; box length: simulation box size in nm; D_{H+}, self-diffusion coefficient of the P bead (H^+); D_{H2O} self-diffusion coefficient of water in (three times larger than that of the W bead); α_P, degree of dissociation of the P bead from S bead; σ, proton conductivity calculated from Nernst equation based on D_{H+} and N_P.

SL (%)	HL (%)	λ	N_{sPS}	N_W	N_P
10	0.05	3	1829	4182	3658
10	0.11	6	1739	7962	3478
20	0.13	4	1631	9236	6524
20	0.19	6	1544	13064	6176
20	0.25	8	1465	16540	5860
40	0.35	6	1234	21768	9872
40	0.45	8	1147	25944	9176
40	0.54	10	1077	29304	8616

time (ns)	box length (nm)	D_{H+} [cm^2/s]	D_{H2O} [cm^2/s]	α_P	σ [S/cm]
93.6	18.3	2.10E-08	1.40E-07	7.50%	8.00E-05
52	18.4	9.50E-08	3.40E-07	19.80%	3.30E-04
52	18.4	2.30E-07	5.50E-07	10.40%	1.50E-03
52	18.5	9.60E-07	1.30E-06	17.10%	5.90E-03

52	18.5	2.10E-06	2.30E-06	22.70%	1.20E-02
52	18.6	5.90E-06	4.40E-06	16.90%	5.70E-02
52	18.7	8.50E-06	5.50E-06	21.00%	7.50E-02
52	18.7	1.10E-05	7.00E-06	24.60%	9.30E-02

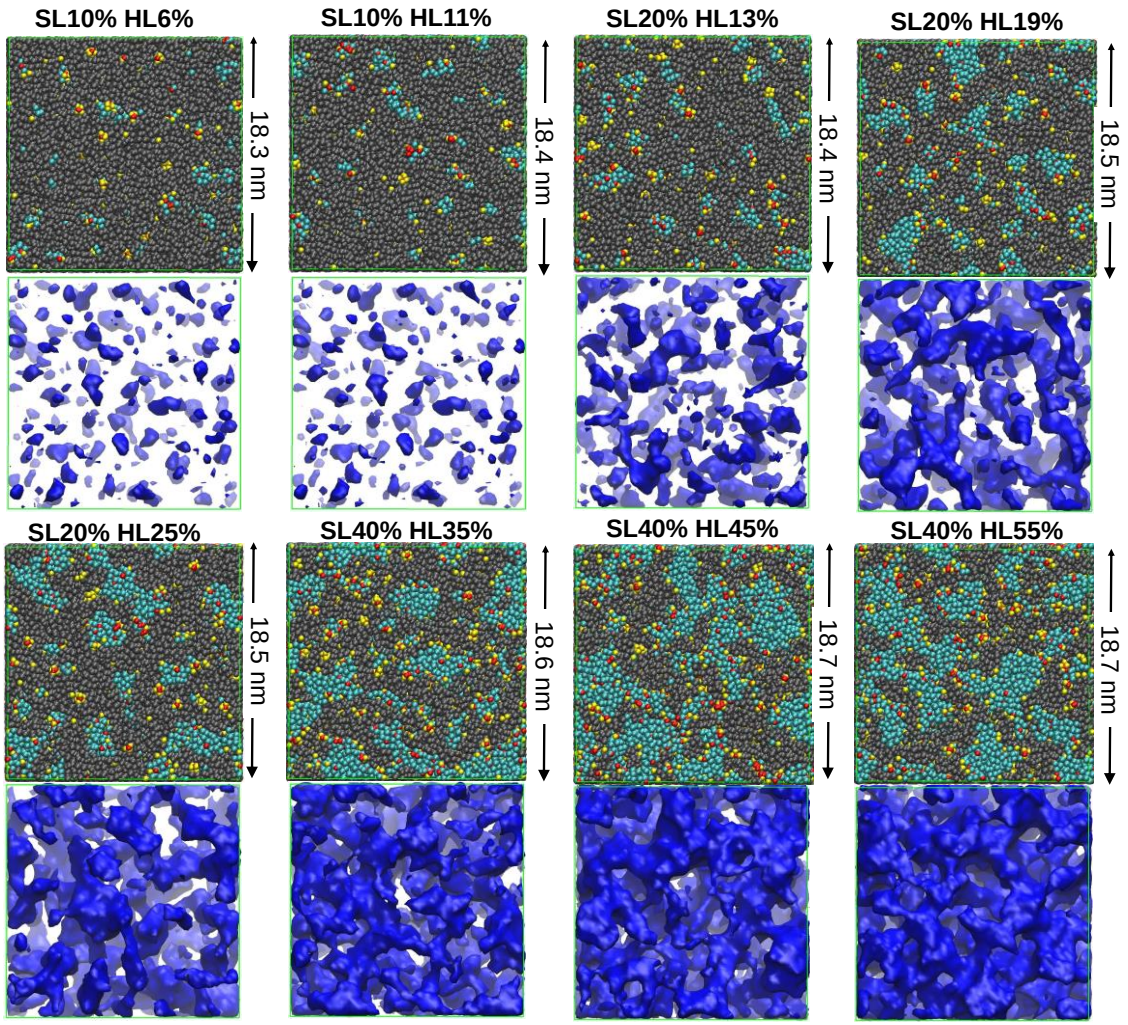

Figure 7-3. 3D perspective of hydrated sulfonated polyetyrene (sPS) at different sulfonation level (SL) and hydration level (HL). Upper figures are visualized as beads: grey – polymer beads, blue – water beads, yellow – sulfonate beads, and red – proton beads. Lower figures are isosurface of W beads.

DPD simulations show that the hydrated sPS is indeed segregated onto the aqueous and organic subphases, in agreement with the experimental and atomistic MD results. Figure 7-3 shows the morphology of the hydrophilic subphase shown in blue at different sulfonation and hydration level. Similarly to Nafion and other PEM, at low hydration water forms separate small clusters, which make an interconnected network as the hydration increases. To characterize the segregated structure, we employed a geometrical algorithm commonly applied to pore structure in solid porous adsorbents, because the hydrophilic phase essentially forms a network of pores in the hydrophobic matrix. First, we created a lattice replica of each segregated sPS structure. The lattice was cubic with a step of $0.5R_c$. Each lattice site was assigned to either mobile aqueous or immobile polymer subphase the local composition of beads around that particular site in that particular moment. In order to assign a lattice site to either the mobile or immobile subphase, we calculate the site preference as follows,

$$p(\vec{r}_l) = \sum_{i=1}^{N} t_i w(\vec{r}_i, \vec{r}_l) \text{ , where } w(\vec{r}_i, \vec{r}_l) = \left(1 - \left|\vec{r}_i - \vec{r}_l\right| / R_c\right)^2 \text{ at } \left|\vec{r}_i - \vec{r}_l\right| < R_c \text{ , } w = 0 \text{ at } \left|\vec{r}_i - \vec{r}_l\right| \geq R_c \text{ ,}$$

Here, r_l is the radius-vector to the center of lattice site l, r_i is the radius-vector to i-th bead, and t_i is a mobility coefficient related to the bead type: $t_i = -1$ for all mobile W beads and $t_i = 1$ was assigned to all polymer beads (B, C, S). $p(\vec{r}_l)$ shows whether mobile of immobile beads prevail in the close vicinity of site l. If p is negative, site l is assigned to mobile (hydrophilic) subphase, otherwise site l is assigned to the immobile (hydrphobic) subphase. (Note that S beads were treated as a part of immobile subphase. Even though they are hydrophilic, they are rigidly attached to the aliphatic skeleton. The situation differs from that in Nafion, where the sidechains are dramatically more flexible compared to the

skeleton and arguments can be made to identify them with either mobile or immobile subphase). The digitized morphologies are illustrated in Supporting Information, S3 of ref [140] The pore size distributions for the hydrophilic pore networks were obtained with algorithms based on the Connely surfaces [144] and applied previously to both irregular [145] and regular porous materials [146]. Any point X belongs to a pore of size *d*, if there exists a sphere of that diameter that includes X but does not include any of the lattice sites that belong to the immobile subphase. Obviously, any point in the system belongs to a pore of size 0, and the volume of space that belongs to pores of size *d* monotonically decreases with *d*. If $V_m(d)$ is the total volume of the space that belongs only to pores of diameters less than *d*, the differential pore size distribution is obtained as a derivative $-V_m'(d)$. For selected systems, they are shown in Figure 4. For calculations, we use Poreblazer 3.0.2 [146-147]. Pore size distributions for all systems are in Supporting Information S4 of ref [140].

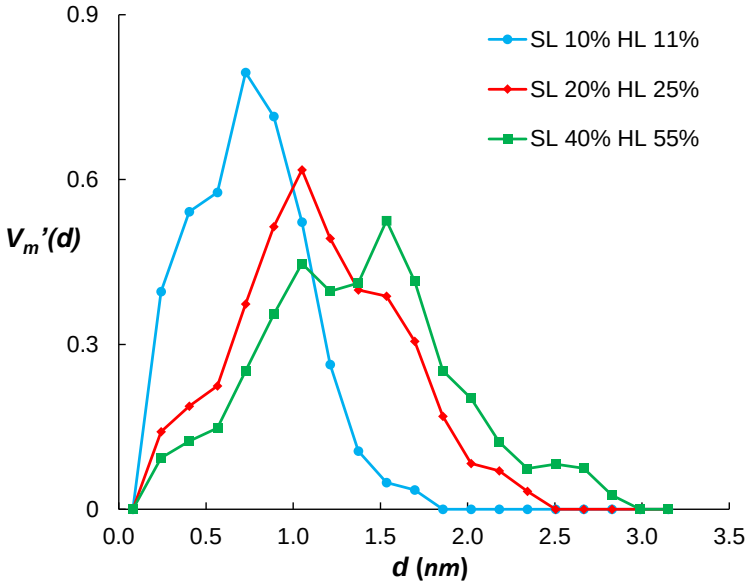

Figure 7-4. Pore size distributions for sPS of different sulfonation level at saturated hydration level. Blue line: SL = 10% and HL = 11%; red line: SL = 20% and HL = 25%, green line: SL = 40% and HL = 55%.

Figure 7-4 shows that the segregation scale in hydrated sPS is indeed small compared to Nafion and other PEM. At low hydration levels, the pore sizes are comparable with R_c, which means that the typical water aggregates only include several beads and may include only one. The total volume of the hydrophilic pores is, obviously, proportional to the hydration, and characteristic pore size increases with hydration. Even for 40% sulfonation level at saturation conditions, the characteristic pore size is limited to 2nm, and the largest pores observed do not exceed 3nm. This generally agrees with the MD simulations of potassium substituted sPS. [85] In all systems, the PSD is unimodal; a characteristic pore size can be identified for each system. The distributions are slightly asymmetric with a "tail" corresponding to larger pores that becomes more prominent as the total hydration increases. Figure 7-5 shows the pore surface per unit volume area. It is clear that the area depends mostly on hydration rather than on the sulfonation level: the results obtained in different systems fall onto the same curve. Thus, the segregation morphology for all systems with the same hydration level is similar and barely depends on the surface density of the sulfonate groups at the interface between the hydrophilic and hydrophobic subphases.

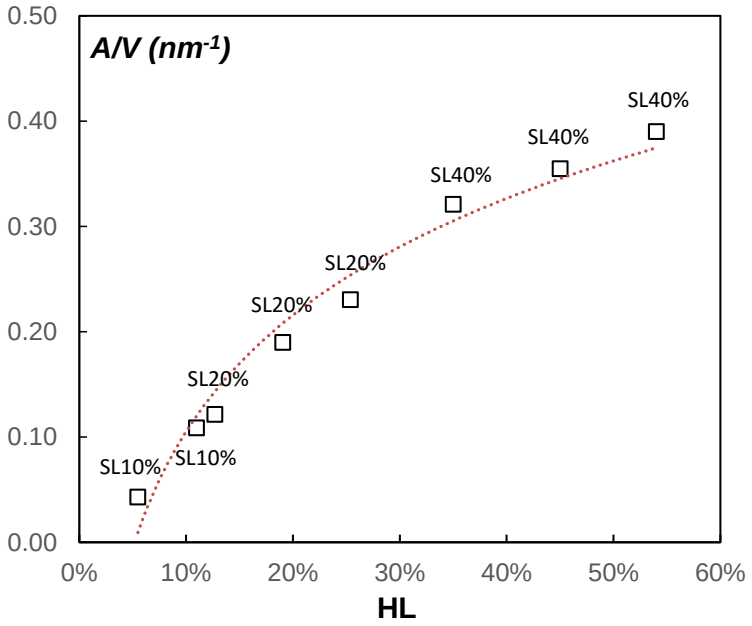

Figure 7-5. Accessible surface area per cubic volume (nm^{-1}) of sPS at different SL and HL Fitting curve and line are for visualization only.

We applied two different techniques for evaluation of water mobility. First, water self-diffusion can be directly calculated from the mean square displacement of water beads in the course of DPD simulation using the Einstein relationship. Since the DPD model cannot reproduce the hydrodynamics of hydrated sPS, we calculate not the diffusion coefficient per se, but its ratio to that in pure bulk coarse-grained water D_W/D_{bulk}. The other technique is based on the random walks in the lattice replicas of segregated sPS structure. [7, 65] We modeled water diffusion within the hydrophilic subphase as a simple random walk of a tracer particle within the mobile domain of the lattice replicas created for hydrophilic subphase characterization and described above. Each random walk started from a randomly selected lattice site that belonged to the hydrophilic subphase, and each step was an attempted move to one of the six sites that neighbored the current location. The move was

accepted if the attempted site belonged to the mobile subphase. 10^4 random walks were performed on each of 400 replicas for proper averaging. We calculated the MSD between current location and the original location as a function of the number of steps.

The two manners to estimate the water mobility appear very similar, yet differ qualitatively. The random walks are conducted in a static lattice replica. That is, any change in the segregation structure (no matter how minor) is assumed infinitely slow compared to the water molecule diffusion. Such a consideration excludes dynamic percolation effects REF entirely: if two clusters are not connected, they will never be connected. Evaluation of D_W from DPD MSDs is on the other extreme: the segregation structure is allowed to evolve in the process of simulation, and the soft-core DPD potentials employed here may significantly overestimate the fluidity of the hydrophobic subphase, which in reality the structure may be semi-glassy. The difference between the two methods of water mobility evaluation is demonstrated by Figure 7-7, which shows the dependence of water self-diffusion on the sulfonation level at saturation conditions. As the sulfonation increases from 10% to 40%, saturation hydration grows from 10% (λ = 3) to 55% (λ = 10), and the volume of the mobile phase increases respectively. In 40% sulfonates PS, both techniques predict $D_W/D_{bulk} \approx 0.25$. Interestingly, this result agrees extremely well with our earlier atomistic MD simulation (although that was carried out with a metal counterion, which may affect diffusion). In 20% sulfonated PS, the random walk technique shows a slightly lower D_W compared to the direct method, and in 10% sulfonated PS, the two estimates differ by five orders of magnitude. The evolution of the segregated structure is the obvious reason for the difference, since in the course of DPD simulation the hydrophilic aggregates are allowed to merge and split and thus water beads are exchanged and their overall

mobility increases (this dynamic percolation effects were also observed in MD simulations of hydrated Nafion [148]). Experimental data on water mobility in pure sPS are very sparse (most measurements have been performed on block copolymers). The gravimetric result of Manoj et al [142] is very close to the simulated D_W/D_{bulk} obtained directly from DPD simulations. This likely means that dynamic percolation effects are indeed very significant in this system, as they are not accounted for in lattice random walk simulations, and the mobility of the W beads in DPD simulations accurately reproduces the actual mobility of water molecules in sPS. However, there is also a possibility that the percolation transition in experiment corresponds to a lower hydration compared to the simulation, but the absence of continuous pore network is somehow artificially substituted by dynamic evolution of the network in DPD.

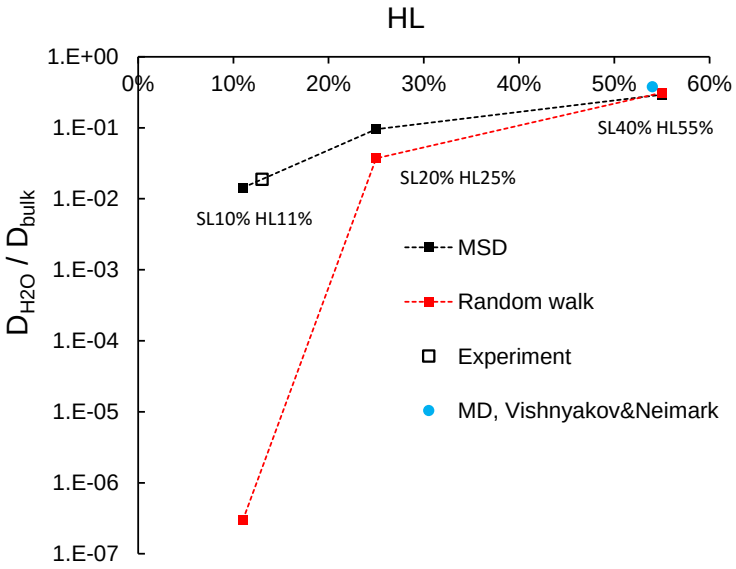

Figure 7-7. Self-diffusion coefficient of water compared to the bulk water mobility at different hydration level (SL10% at HL11%, SL20% at HL25%, and SL40% at HL55%). Black line is calculated directly from the MSD of the water from the simulation. Red line is calculated by using random walk approach in 400 static trajectories. The empty square is the experimental data for 11% sPS (H^+) at 13 wt% water adsorption. Cyan circle is MD results for 40% sPS (Ca^{2+}) at 54 wt% water uptake.

The proton self-diffusion and membrane conductivity are determined not only by the segregation morphology, but also by the dissociation of the acid groups, which is modeled explicitly. The snapshots of the DPD configuration shown in Figure 7-8 display an expected picture: S beads, some protonated and some not, are located at the interface between the hydrophobic and hydrophilic subphases. To characterize the dissociation, we use the same criterion, as in Section 6: a P bead is considered as dissociated if no S bead is found within the Morse cutoff radius r^{M} from the P bead. The degree of dissociation α is the fraction of dissociated P beads. The dependence of α on sulfonation and hydration is shown in Figure 7-8.

Naturally, α increases with hydration and is mostly determined by λ, the number of water molecules per sulphonic group. In all systems, even for the highest λ considered, most P beads are associated with at least one S bead. state It is worth mentioning that the dissociation constant of benzenesulfonic acid is $K_a = 0.2$, unlike $K_a = 10^{12\,149}$ for triflic acid that serves as a reference compound for Nafion. Assuming that the activity coefficients γ of H^+ and $PhSO_3^-$ ions in a bulk aqueous solution of benzenesulfonic acid are equal to one, one would obtain $\alpha = 0.18$ at $\lambda = 10$. The $\gamma_{H+} = \gamma_{PhSO3-} = 1$ assumption is only valid in dilute solutions and is not applicable in the systems of interest to this work. Yet, it is obvious that one can hardly expect full dissociation of protons in concentrated $PhSO_3H$ solutions, and therefore the low dissociation degree in hydrated sPS is not surprising. At constant λ, α decreases with sulfonation (that is, as the surface density of the sulfonates at the interface between the hydrophobic and hydrophilic subphases), which is also expected.

In the snapshots shown in Figure 7-3, one may notice that in some cases, S and P beads form “clusters” or agglomerates consisting nearly entirely of charges beads with barely any W beads inside. Morse and electrostatic attraction between P and S beads overpower the conservative short-range repulsion between S beads and the entropy that favors charge bead solvation by W beads. It is also illustrated in Supporting Information, Section This effect is probably artificial and shows the shortcomings of the simplistic DPD potentials, which do not correctly reproduce the actual short-range interactions between the beads. Despite the shortcoming, the general picture of ion solvation and dissociation in sulfonated sPS is quite reasonable and agrees with experimental data

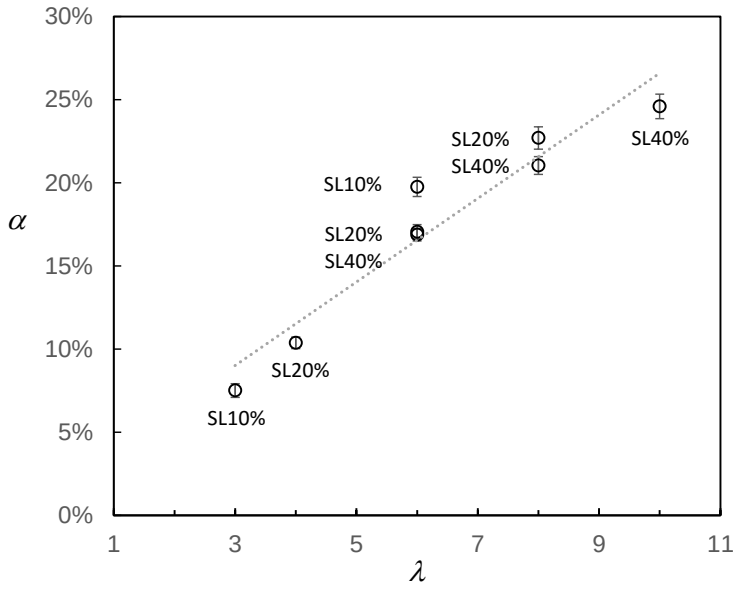

Figure 7-8. Degree of proton dissociation α as the function of number of water per sulfonate group λ. Systems with the same λ are marked based on the sulfonation levels.

Since the proton is incorporated directly into DPD calculations, we estimated the ratio of its self-diffusion coefficient to that of water from the MSDs of the P beads. In the

water bulk, $D_P/D_W \approx 3.8$: the proton is about four times as mobile as a water molecule thanks to the Grotthuss "hopping" mechanism. In hydrated PEM, the Grotthuss mechanisms are also in effect; sulfonate ions can also participate in the Grotthuss type hopping. To utilize the Grotthuss mechanism the proton has to dissociate from its sulfonate, first of all, and then to overcome the electrostatic attraction to its former anion. As a result the difference between water and protons self-diffusion in poorly hydrated PEM is not as significant as in the water bulk. Proton may be even slower than water at low λ.

Figure 7-9a shows the self-diffusion coefficient of water and proton in hydrated sPS related to the diffusion coefficient of bulk water. It appears remarkable that D_W and D_P data obtained for different sulfonation levels fall onto the same master curves and only depend on the hydration (the same figure in terms of λ is shown in Supporting Information, Section S5 of ref [140]). Water indeed is more mobile than the proton at low hydration. Hydration contributes to the proton diffusion stronger than to the diffusion of water. At about 20% water content, water and proton diffusion coefficients become equal, and at higher hydration proton diffuses faster than water: in PS with 40% sulfonation and saturated hydration of 55% DP/DW≈ 2 at 40% sulfonation and 55% water content. The ratio is still two times lower than in bulk water. In experiments, a similar qualitative behavior was observed for PVDF-grafted-PSSA block copolymer. [150] Proton diffuse slower than water at λ = 5, but become faster than water at around λ = 10. Such crossover happens at lower λ =6-7, because there is no distinct segregated morphology such as PVDF-g-PSSA and water diffuse much slower at low λ compared to that in PVDF-g-PSSA. Interesting enough, proton diffusion coefficient reaches 1E-5 cm^2/s at similar values λ = 10 in both sPS and PVDF-g-PSSA. In Nafion , where dissociating is more facile due

to a much higher K_a, D_P is generally higher than in PEM with benzenesulfonic acid groups and $D_P/D_W > 1$ even at low λ, but qualitatively $D_P(\lambda)$ is very similar. Thus, our DPD model reproduces the mechanism of proton mobility protons in hydrated PEM at least on the qualitative level.

To compare our mobilities with experimental results, we calculated the conductivities of hydrated sPS from proton self-diffusion coefficients using the Nernst equation: $\sigma_{H^+} = \frac{F^2}{RT} D_{H^+} C_{H^+}$, where F is the Faraday constant and C_{H^+} is the overall proton concentration. Figure 9b shows the proton conductivity in sPS fully saturated with water. The experiment data are derived from ref. [151] The experimental conductivities are only available for sulfonation levels between 10% and 20%; the water content is not reported in ref [151], but we calculated it from sulfonation using the experimental sorption data. Our conductivities are of the same order of magnitude as the experimental ones, but show more gradual dependence on hydration. In particular, we underestimate the conductivity at high hydration. The possible reason are the artificial S-H "clusters" noted above, since the protons that belong to such cluster are less mobile in simulation compared to the experiment.

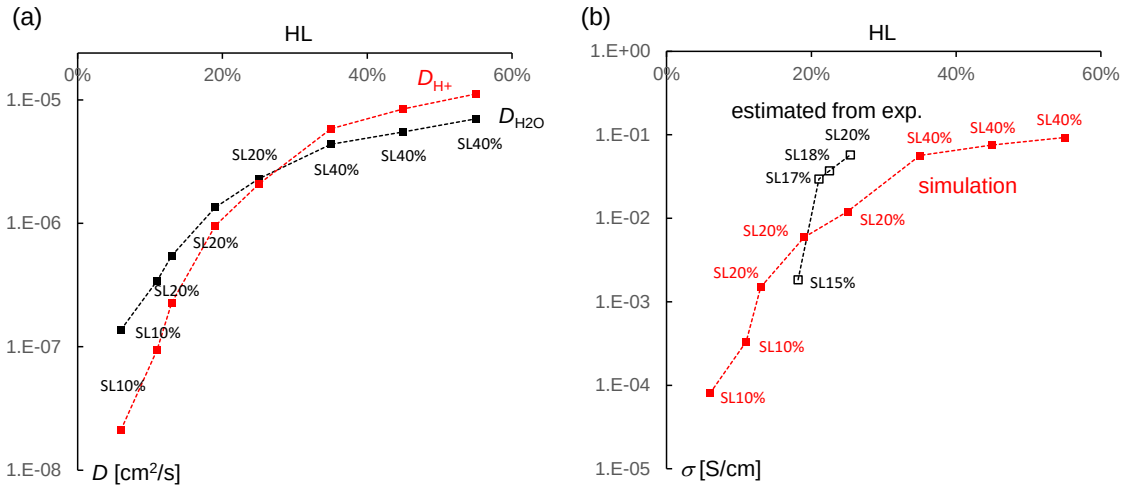

Figure 7-9. (a) Diffusion coefficient of water and proton estimated from the MSD of W beads and P bead, at different sulfonation (SL) and hydration levels (HL). (b) Proton conductivity calculated by proton concentration and diffusion coefficient. Black lines are derived from the experimental data at different sulfonation level. Conductivity of sPS (sulfonation level from 10% to 20% at fully hydrated state) at 22 ºC and 60 ºCare interpolated to obtain the conductivity at 30 ºC,

To conclude, we applied our DPD modelling approach developed for systems with protonation equilibria to sulfonated polystyrene, which forms the hydrophilic domain of several prospective proton-exchange membranes for fuel cells. Our approach offers a few advances in such simulations (i) the smeared charge models allows explicit consideration of electrostatic interactions (2) the dissociating Morse bonds between the proton (which is explicitly introduces as a separate bead) and the base beads (water and the anion) establishes dissociation equilibrium between protonated and deprotonated forms of an acid (3) the model artificially mimics Grotthuss mechanism of proton diffusion. The Morse potentials are parameterized from proton mobility in pure water and benzenesulfonic acid dissociation constant and involve no data on hydrated polymer. The short-range conservative repulsion parameters were parameterized from infinite dilution activity

coefficients of reference compounds, and bonded forcefield terms are parameterized from atomistic MD simulations of sPS fragments.

Although sPS forms the hydrophilic domain on the PEM materials, it itself segregates into irregular hydrophilic and hydrophobic subphases upon hydration. The fact of the segregation and its approximate scale were correctly reproduced by DPD simulations. The sulfonate groups locate at the interface between the hydrophilic and hydrophobic subphases. The acid showed a partial dissociation; the dissociation degree showed an approximately linear dependence on the number of water molecules per sulfonate group, and a weak dependence on the sulfonation level. We also observed some unphysical clusters of sulfonate anions and protons, relatively tight with little water inside. Water self-diffusion was estimated directly from the mean square displacement of water beads and showed a remarkable agreement with experimental results (at low hydration) and atomistic MD results (at high hydration). Interestingly, an estimate obtained from random walks in a static lattice replicas of the segregated structure showed much slower diffusion at low hydration, but the same diffusion at higher hydration. We refer this difference to dynamics percolation effects: water aggregates merge and break up in the course of DPD simulation, and this effect is ignored by random walks in static lattice replicas. Proton mobilities obtained from DPD also showed a reasonable agreement with experimental data: they are lower than the mobility of water molecule at low hydration and higher at high hydration. The conductivities estimated from self-diffusion using the Nernst equation showed reasonable agreement with the experiments as well.

Overall, the modeling approach presented here is certainly promising for mesoscale simulations of proton-exchange membranes. An absence of reliable techniques for

parameterization of the short-range interactions between the charged species as well as the charge smearing parameters remains a serious problem; we suspect that the unphysical clustering between sulphonate and proton beads originates from underestimated short-range repulsion of such species. Perhaps activity coefficient or even radial distribution functions in reference electrolyte solutions or can be used as target properties for parameterization of short-range interactions and charge distributions.

Section 8. Conclusion

Dissipative particle dynamics is a simple yet powerful tool for studying self-assembly of polymeric systems. Generally speaking, DPD can reproduce most equilibrium morphologies of the selected systems by tweaking the repulsion parameters. This thesis addresses several important issues in coarse grained model construction and forcefield parameterization. The development achieved here elevates the DPD method to be more predictive and robust for modeling equilibrium and dynamics properties for the system of interests. It is crucial for the research fields involving the design of surfactant based detergent and polyelectrolyte implemented fuel cell devices.

The construction of coarse grained model and parameterization of the interaction parameters need to be done simultaneously. We have shown that the “bottom-up” configurational constraints which reproduces the conformation of chain molecule at atomistic level certainly improve the performance of DPD in modeling self-assembly. The repulsion parameter should be determined using the “top-down” approach introduced here taking into account bond, rigidity, and the coarse grained bead size. The obtained repulsion parameters produce the accurate hydrophobicity of the target molecule, which matches to the thermodynamic properties of its represented compounds such as solubility or activity coefficient. The combined use of the top down parameterization and bottom up configurational constraints have shown reliable performances in predicting micellar properties of various surfactant, which is a benchmark problem for coarse graining modeling.

Through studying the proton transfer in the hydrated PEM, we has exhibited the possibility to recover the atomistic details in the coarse grained DPD model using a customized bead type and forces. The modified DPD scheme preserves the ability in describing the bulk properties of polymeric system, yet adding the function to mimic the detailed reaction-like association which is important to the systems with significant ion/proton dissociation and relocation. Compiled with the parameterization method developed with surfactant micellization, it shows a impressing predictive ability in describing PEM morphologies, water permeability, and even proton conductivity without using any empirical correlations.

In addition to all the success we have presented here, we also discuss several important limitations for future DPD development. The most crucial part is the assumption of equal volume and equal intra-component repulsion parameter made by Groot and Warren, which is the basis of our approach. Although there have been several improved algorithms related to this assumption, we are not aware of any successful application of these approaches in systematically reproducing the self-assembly of complex fluids. Another issue is related to the future application of proton model and association potential. Unlike protonated PEM in the fuel cell unit, the counterion are usually co-valent in the PEM which is applied in the protective cloth. The morphologies of the hydrated PEM is highly related to the association between counterion and PEM sidechain. The Morse potential should be parameterized (or with constraints) in order to reproduce the correct coordination number of the counterion with water and sulfonate group. These developments can be easily extended based on the theoretical framework in this thesis.

References

1. Vishnyakov, A.; Lee, M.-T.; Neimark, A. V., Prediction of the Critical Micelle Concentration of Nonionic Surfactants by Dissipative Particle Dynamics Simulations. *Journal of Physical Chemistry Letters* **2013,** *4* (5), 797-802.
2. Rekvig, L.; Kranenburg, M.; Vreede, J.; Hafskjold, B.; Smit, B., Investigation of surfactant efficiency using dissipative particle dynamics. *Langmuir* **2003,** *19* (20), 8195-8205.
3. Prinsen, P.; Warren, P. B.; Michels, M. A. J., Mesoscale simulations of surfactant dissolution and mesophase formation. *Physical Review Letters* **2002,** *89* (14).
4. Groot, R. D.; Rabone, K. L., Mesoscopic simulation of cell membrane damage, morphology change and rupture by nonionic surfactants. *Biophysical Journal* **2001,** *81* (2), 725-736.
5. Shillcock, J. C.; Lipowsky, R., Equilibrium structure and lateral stress distribution of amphiphilic bilayers from dissipative particle dynamics simulations. *Journal of Chemical Physics* **2002,** *117* (10), 5048-5061.
6. Groot, R. D., Electrostatic interactions in dissipative particle dynamics-simulation of polyelectrolytes and anionic surfactants. *Journal of Chemical Physics* **2003,** *118* (24), 11265-11277.
7. Vishnyakov, A.; Neimark, A. V., Self-Assembly in Nafion Membranes upon Hydration: Water Mobility and Adsorption Isotherms. *Journal of Physical Chemistry B* **2014,** *118* (38), 11353-11364.
8. Yamamoto, S.; Hyodo, S. A., A computer simulation study of the mesoscopic structure of the polyelectrolyte membrane Nafion. *Polymer Journal* **2003,** *35* (6), 519-527.
9. Bernardes, A. T.; Henriques, V. B.; Bisch, P. M., Monte-carlo simulation of a lattice model for micelle formation. *Journal of Chemical Physics* **1994,** *101* (1), 645-650.
10. Smit, B.; Esselink, K.; Hilbers, P. A. J.; Vanos, N. M.; Rupert, L. A. M.; Szleifer, I., Computer-simulations of surfactant self-assembly. *Langmuir* **1993,** *9* (1), 9-11.
11. Larson, R. G., Monte-carlo simulation of microstructural transitions in surfactant systems. *Journal of Chemical Physics* **1992,** *96* (11), 7904-7918.
12. Cheong, D. W.; Panagiotopoulos, A. Z., Monte Carlo simulations of micellization in model ionic surfactants: Application to sodium dodecyl sulfate. *Langmuir* **2006,** *22* (9), 4076-4083.
13. Jusufi, A.; Hynninen, A.-P.; Panagiotopoulos, A. Z., Implicit Solvent Models for Micellization of Ionic Surfactants. *Journal of Physical Chemistry B* **2008,** *112* (44), 13783-13792.
14. Lazaridis, T.; Mallik, B.; Chen, Y., Implicit solvent simulations of DPC micelle formation. *Journal of Physical Chemistry B* **2005,** *109* (31), 15098-15106.
15. LeBard, D. N.; Levine, B. G.; Mertmann, P.; Barr, S. A.; Jusufi, A.; Sanders, S.; Klein, M. L.; Panagiotopoulos, A. Z., Self-assembly of coarse-grained ionic surfactants accelerated by graphics processing units. *Soft Matter* **2012,** *8* (8), 2385-2397.
16. Sammalkorpi, M.; Sanders, S.; Panagiotopoulos, A. Z.; Karttunen, M.; Haataja, M., Simulations of Micellization of Sodium Hexyl Sulfate. *Journal of Physical Chemistry B* **2011,** *115* (6), 1403-1410.

17. Sanders, S. A.; Panagiotopoulos, A. Z., Micellization behavior of coarse grained surfactant models. *Journal of Chemical Physics* **2010,** *132* (11).
18. Lazaridis, T.; Karplus, M., Effective energy function for proteins in solution. *Proteins* **1999,** *35*, 133-152.
19. Pool, R.; Bolhuis, P. G., Can purely repulsive soft potentials predict micelle formation correctly? *Physical Chemistry Chemical Physics* **2006,** *8* (8), 941-948.
20. Groot, R. D., Mesoscopic simulation of polymer-surfactant aggregation. *Langmuir* **2000,** *16* (19), 7493-7502.
21. Li, Z.; Dormidontova, E. E., Kinetics of Diblock Copolymer Micellization by Dissipative Particle Dynamics. *Macromolecules* **2010,** *43* (7), 3521-3531.
22. Lin, Y.-L.; Wu, M.-Z.; Sheng, Y.-J.; Tsao, H.-K., Effects of molecular architectures and solvophobic additives on the aggregative properties of polymeric surfactants. *Journal of Chemical Physics* **2012,** *136* (10).
23. Groot, R. D.; Warren, P. B., Dissipative particle dynamics: Bridging the gap between atomistic and mesoscopic simulation. *Journal of Chemical Physics* **1997,** *107* (11), 4423-4435.
24. Wijmans, C. M.; Smit, B.; Groot, R. D., Phase behavior of monomeric mixtures and polymer solutions with soft interaction potentials. *Journal of Chemical Physics* **2001,** *114* (17), 7644-7654.
25. Lyubartsev, A. P.; Karttunen, M.; Vattulainen, I.; Laaksonen, A., On coarse-graining by the inverse Monte Carlo method: Dissipative particle dynamics simulations made to a precise tool in soft matter modeling. *Soft Mater.* **2003,** *1* (1), 121-137.
26. Backer, J. A.; Lowe, C. P.; Hoefsloot, H. C. J.; Iedema, P. D., Combined length scales in dissipative particle dynamics. *Journal of Chemical Physics* **2005,** *123* (11).
27. Travis, K. P.; Bankhead, M.; Good, K.; Owens, S. L., New parametrization method for dissipative particle dynamics. *Journal of Chemical Physics* **2007,** *127* (1).
28. Maiti, A.; McGrother, S., Bead-bead interaction parameters in dissipative particle dynamics: Relation to bead-size, solubility parameter, and surface tension. *Journal of Chemical Physics* **2004,** *120* (3), 1594-1601.
29. Spaeth, J. R.; Dale, T.; Kevrekidis, I. G.; Panagiotopoulos, A. Z., Coarse-Graining of Chain Models in Dissipative Particle Dynamics Simulations. *Industrial & Engineering Chemistry Research* **2011,** *50* (1), 69-77.
30. Kacar, G.; Peters, E. A. J. F.; de With, G., A generalized method for parameterization of dissipative particle dynamics for variable bead volumes. *Epl* **2013,** *102* (4).
31. Liyana-Arachchi, T. P.; Jamadagni, S. N.; Eike, D.; Koenig, P. H.; Siepmann, J. I., Liquid-liquid equilibria for soft-repulsive particles: Improved equation of state and methodology for representing molecules of different sizes and chemistry in dissipative particle dynamics. *Journal of Chemical Physics* **2015,** *142* (4).
32. Groot, R. D.; Madden, T. J., Dynamic simulation of diblock copolymer microphase separation. *Journal of Chemical Physics* **1998,** *108* (20), 8713-8724.
33. Yamamoto, S.; Maruyama, Y.; Hyodo, S., Dissipative particle dynamics study of spontaneous vesicle formation of amphiphilic molecules. *Journal of Chemical Physics* **2002,** *116* (13), 5842-5849.
34. Marshall, B. D.; Emborsky, C.; Cox, K.; Chapman, W. G., Effect of Bond Rigidity and Molecular Structure on the Self-Assembly of Amphiphilic Molecules Using Second-

Order Classical Density Functional Theory. *Journal of Physical Chemistry B* **2012,** *116* (9), 2730-2738.
35. Heerklotz, H.; Tsamaloukas, A.; Kita-Tokarczyk, K.; Strunz, P.; Gutberlet, T., Structural, volumetric, and thermodynamic characterization of a micellar sphere-to-rod transition. *Journal of the American Chemical Society* **2004,** *126* (50), 16544-16552.
36. Sterpone, F.; Briganti, G.; Pierleoni, C., Sphere versus Cylinder: The Effect of Packing on the Structure of Nonionic C12E6 Micelles. *Langmuir* **2009,** *25* (16), 8960-8967.
37. Srinivasan, V.; Blankschtein, D., Prediction of conformational characteristics and micellar solution properties of fluorocarbon surfactants. *Langmuir* **2005,** *21* (4), 1647-1660.
38. Sharma, S. C.; Abe, M.; Aramaki, K., Viscoelastic Worm - Like Micelles in Nonionic Fluorinated Surfactant Systems. In *Self-Organized Surfactant Structures.*, Tadros, T. F., Ed. WILEY-VCH Verlag GmbH & Co. KGaA, Weinheim: 2010.
39. Firetto, V.; Floriano, M. A.; Panagiotopoulos, A. Z., Effect of stiffness on the micellization behavior of model H4T4 surfactant chains. *Langmuir* **2006,** *22* (15), 6514-6522.
40. Savinell, R.; Yeager, E.; Tryk, D.; Landau, U.; Wainright, J.; Weng, D.; Lux, K.; Litt, M.; Rogers, C., A POLYMER ELECTROLYTE FOR OPERATION AT TEMPERATURES UP TO 200-DEGREES-C. *Journal of the Electrochemical Society* **1994,** *141* (4), L46-L48.
41. Gierke, T. D.; Hsu, W. Y., The Cluster-Network Model of Ion Clustering in Perfluorosulfonated Membranes. In *Perfluorinated Ionomer Membranes*, Eisenberg, A.; Yeager, H., Eds. ACS: 1982; Vol. 180.
42. Shiryaeva, I. M.; Victorov, A. I., Equilibrium of ion-exchange polymeric membrane with aqueous salt solution and its thermodynamic modeling. *Fluid Phase Equilibria* **2001,** *180* (1-2), 115-138.
43. Galperin, D.; Khalatur, P. G.; Khokhlov, A. R., Morphology of Nafion Membranes: Microscopic and Mesoscopic Modeling. *Device and Materials Modeling in Pem Fuel Cells* **2009,** *113*, 453-482.
44. Galperin, D. Y.; Khokhlov, A. R., Mesoscopic morphology of proton-conducting polyelectrolyte membranes of Nafion((R)) type: A self-consistent mean field simulation. *Macromolecular Theory and Simulations* **2006,** *15* (2), 137-146.
45. Kyrylyuk, A. V.; Fraaije, J., Structure formation in films of weakly charged block polyelectrolyte solutions. *Journal of Chemical Physics* **2004,** *121* (18), 9166-9171.
46. Malek, K.; Eikerling, M.; Wang, Q.; Liu, Z.; Otsuka, S.; Akizuki, K.; Abe, M., Nanophase segregation and water dynamics in hydrated Nafion: molecular modeling and experimental validation. *The Journal of chemical physics* **2008,** *129* (20), 204702.
47. Komarov, P. V.; Veselov, I. N.; Chu, P. P.; Khalatur, P. G., Mesoscale simulation of polymer electrolyte membranes based on sulfonated poly(ether ether ketone) and Nafion. *Soft Matter* **2010,** *6* (16), 3939-3956.
48. Malek, K.; Eikerling, M.; Wang, Q. P.; Navessin, T. C.; Liu, Z. S., Self-organization in catalyst layers of polymer electrolyte fuel cells. *Journal of Physical Chemistry C* **2007,** *111* (36), 13627-13634.

49. Wescott, J. T.; Qi, Y.; Subramanian, L.; Capehart, T. W., Mesoscale simulation of morphology in hydrated perfluorosulfonic acid membranes. *Journal of Chemical Physics* **2006,** *124* (13), 14.
50. Xiao, Y.; Dou, M. L.; Yuan, J. L.; Hou, M.; Song, W.; Sunden, B., Fabrication Process Simulation of a PEM Fuel Cell Catalyst Layer and Its Microscopic Structure Characteristics. *Journal of the Electrochemical Society* **2012,** *159* (3), B308-B314.
51. Yamamoto, S., Mesoscopic simulation for the drying process of polymer films. *Nihon Reoroji Gakkaishi* **2004,** *32* (5), 295-301.
52. Dorenbos, G., Dependence of pore morphology and diffusion on hydrophilic site distribution within hydrated amphiphilic multi block co-polymer membranes. *Polymer* **2013,** *54* (18), 5024-5034.
53. Dorenbos, G., Pore network design: DPD-Monte Carlo study of solvent diffusion dependence on side chain location. *Journal of Power Sources* **2014,** *270*, 536-546.
54. Dorenbos, G., Water diffusion within hydrated model grafted polymeric membranes with bimodal side chain length distributions. *Soft Matter* **2015,** *11* (14), 2794-2805.
55. Dorenbos, G.; Morohoshi, K., Pore morphologies and diffusion within hydrated polyelectrolyte membranes: Homogeneous vs heterogeneous and random side chain attachment. *Journal of Chemical Physics* **2013,** *138* (6).
56. Elliott, J. A.; Paddison, S. J., Modelling of morphology and proton transport in PFSA membranes. *Physical Chemistry Chemical Physics* **2007,** *9* (21), 2602-2618.
57. Elliott, J. A.; Wu, D.; Paddison, S. J.; Moore, R. B., A unified morphological description of Nafion membranes from SAXS and mesoscale simulations. *Soft Matter* **2011,** *7* (15), 6820-6827.
58. Wu, D.; Paddison, S. J., Mesoscopic Simulations of the Hydrated Morphology of the Short-Side-Chain Perfluorosulfonic Acid Ionomer. In *Fuel Cell Chemistry and Operation*, Herring, A. M.; Zawodzinski, T. A.; Hamrock, S. J., Eds. 2010; Vol. 1040, pp 83-+.
59. Wu, D.; Paddison, S. J.; Elliott, J. A., A comparative study of the hydrated morphologies of perfluorosulfonic acid fuel cell membranes with mesoscopic simulations. *Energy & Environmental Science* **2008,** *1* (2), 284-293.
60. Wu, D.; Paddison, S. J.; Elliott, J. A., Effect of Molecular Weight on Hydrated Morphologies of the Short-Side-Chain Perfluorosulfonic Acid Membrane. *Macromolecules* **2009,** *42* (9), 3358-3367.
61. Wu, D.; Paddison, S. J.; Elliott, J. A.; Hamrock, S. J., Mesoscale Modeling of Hydrated Morphologies of 3M Perfluorosulfonic Acid-Based Fuel Cell Electrolytes. *Langmuir* **2010,** *26* (17), 14308-14315.
62. Din, X. D.; Michaelides, E. E., Transport processes of water and protons through micropores. *Aiche Journal* **1998,** *44* (1), 35-47.
63. Spohr, E., Molecular dynamics simulations of proton transfer in a model Nafion pore. *Molecular Simulation* **2004,** *30* (2-3), 107-115.
64. Eikerling, M.; Kornyshev, A. A.; Stimming, U., Electrophysical properties of polymer electrolyte membranes: A random network model. *Journal of Physical Chemistry B* **1997,** *101* (50), 10807-10820.

65. Dorenbos, G.; Suga, Y., Simulation of equivalent weight dependence of Nafion morphologies and predicted trends regarding water diffusion. *Journal of Membrane Science* **2009,** *330* (1-2), 5-20.
66. Dorenbos, G.; Pomogaev, V. A.; Takigawa, M.; Morohoshi, K., Prediction of anisotropic transport in Nafion containing catalyst layers. *Electrochemistry Communications* **2010,** *12* (1), 125-128.
67. Sawada, S.; Yamaki, T.; Ozawa, T.; Suzuki, A.; Terai, T.; Maekawa, Y., Water Transport in Polymer Electrolyte Membranes Investigated by Dissipative Particle Dynamics Simulation. In *Polymer Electrolyte Fuel Cells 10, Pts 1 and 2*, Gasteiger, H. A.; Weber, A.; Strasser, P.; Edmundson, M.; Lamy, C.; Darling, R.; Uchida, H.; Schmidt, T. J.; Shirvanian, P.; Buchi, F. N.; Mantz, R.; Zawodzinski, T.; Ramani, V.; Fuller, T.; Inaba, M.; Jones, D.; Narayanan, S. R., Eds. 2010; Vol. 33, pp 1067-1078.
68. Giotto, M. V.; Zhang, J. H.; Inglefield, P. T.; Wen, W. Y.; Jones, A. A., Nanophase structure and diffusion in swollen perfluorosulfonate ionomer: An NMR approach. *Macromolecules* **2003,** *36* (12), 4397-4403.
69. Gong, X.; Bandis, A.; Tao, A.; Meresi, G.; Wang, Y.; Inglefield, P. T.; Jones, A. A.; Wen, W. Y., Self-diffusion of water, ethanol and decafluropentane in perfluorosulfonate ionomer by pulse field gradient NMR. *Polymer* **2001,** *42* (15), 6485-6492.
70. Jorn, R.; Savage, J.; Voth, G. A., Proton Conduction in Exchange Membranes across Multiple Length Scales. *Accounts of Chemical Research* **2012,** *45* (11), 2002-2010.
71. Espanol, P.; Revenga, M., Smoothed dissipative particle dynamics. *Physical Review E* **2003,** *67* (2).
72. Kreuer, K. D.; Schuster, M.; Obliers, B.; Diat, O.; Traub, U.; Fuchs, A.; Klock, U.; Paddison, S. J.; Maier, J., Short-side-chain proton conducting perfluorosulfonic acid ionomers: Why they perform better in PEM fuel cells. *Journal of Power Sources* **2008,** *178* (2), 499-509.
73. Zawodzinski, T. A.; Neeman, M.; Sillerud, L. O.; Gottesfeld, S., DETERMINATION OF WATER DIFFUSION-COEFFICIENTS IN PERFLUOROSULFONATE IONOMERIC MEMBRANES. *Journal of Physical Chemistry* **1991,** *95* (15), 6040-6044.
74. Wang, C.; Paddison, S. J., Mesoscale modeling of hydrated morphologies of sulfonated polysulfone ionomers. *Soft Matter* **2014,** *10* (6), 819-830.
75. Dorenbos, G.; Morohoshi, K., Chain architecture dependence of pore morphologies and water diffusion in grafted and block polymer electrolyte fuel cell membranes. *Energy & Environmental Science* **2010,** *3* (9), 1326-1338.
76. Gonzalez-Melchor, M.; Mayoral, E.; Velazquez, M. E.; Alejandre, J., Electrostatic interactions in dissipative particle dynamics using the Ewald sums. *Journal of Chemical Physics* **2006,** *125* (22), 224107.
77. Warren, P. B.; Vlasov, A.; Anton, L.; Masters, A. J., Screening properties of Gaussian electrolyte models, with application to dissipative particle dynamics. *Journal of Chemical Physics* **2013,** *138* (20), 204907.
78. Warren, P. B.; Vlasov, A., Screening properties of four mesoscale smoothed charge models, with application to dissipative particle dynamics. *Journal of Chemical Physics* **2014,** *140* (8).

79. Peter, E. K.; Pivkin, I. V., A polarizable coarse-grained water model for dissipative particle dynamics. *Journal of Chemical Physics* **2014,** *141* (16), 10.
80. Posel, Z.; Limpouchova, Z.; Sindelka, K.; Lisal, M.; Prochazka, K., Dissipative Particle Dynamics Study of the pH-Dependent Behavior of Poly(2-vinylpyridine)-block-poly(ethylene oxide) Diblock Copolymer in Aqueous Buffers. *Macromolecules* **2014,** *47* (7), 2503-2514.
81. Lee, M.-T.; Vishnyakov, A.; Neimark, A. V., Calculations of Critical Micelle Concentration by Dissipative Particle Dynamics Simulations: The Role of Chain Rigidity. *Journal of Physical Chemistry B* **2013,** *117* (35), 10304-10310.
82. Mao, R.; Lee, M.-T.; Vishnyakov, A.; Neimark, A. V., Modeling aggregation of ionic surfactants using a smeared charge approximation in dissipative particle dynamics simulations. *Journal of Physical Chemistry B* **2005**, in press.
83. Cheng, J. L.; Vishnyakov, A.; Neimark, A. V., Morphological Transformations in Polymer Brushes in Binary Mixtures: DPD Study. *Langmuir* **2014,** *30* (43), 12932-12940.
84. Lee, M.-T.; Vishnyakov, A.; Gor, G. Y.; Neimark, A. V., Interactions of Sarin with Polyelectrolyte Membranes: A Molecular Dynamics Simulation Study. *Journal of Physical Chemistry B* **2013,** *117* (1), 365-372.
85. Vishnyakov, A.; Neimark, A. V., Molecular Dynamics Simulation of Nanoscale Distribution and Mobility of Water and Dimethylmethylphosphonate in Sulfonated Polystyrene. *Journal of Physical Chemistry B* **2008,** *112* (47), 14905-14910.
86. Vishnyakov, A.; Neimark, A. V., Specifics of solvation of sulfonated polyelectrolytes in water, dimethylmethylphosphonate, and their mixture: A molecular simulation study. *Journal of Chemical Physics* **2008,** *128* (16).
87. Espanol, P.; Warren, P., STATISTICAL-MECHANICS OF DISSIPATIVE PARTICLE DYNAMICS. *Europhysics Letters* **1995,** *30* (4), 191-196.
88. Ewald, P. P., *Ann. Phys.* **1921,** *64* (253).
89. Lee, M.-T.; Vishnyakov, A.; Neimark, A. V., Modeling Proton Dissociation and Transfer Using Dissipative Particle Dynamics Simulation. *J. Chem. Theory Comput.* **2015**.
90. Sindelka, K.; Limpouchova, Z.; Lisal, M.; Prochazka, K., Dissipative Particle Dynamics Study of Electrostatic Self-Assembly in Aqueous Mixtures of Copolymers Containing One Neutral Water-Soluble Block and One Either Positively or Negatively Charged Polyelectrolyte Block. *Macromolecules* **2014,** *47* (17), 6121-6134.
91. Seaton, M. A.; Anderson, R. L.; Metz, S.; Smith, W., DL_MESO: highly scalable mesoscale simulations. *Molecular Simulation* **2013,** *39* (10), 796-821.
92. Lu, J. R.; Li, Z. X.; Thomas, R. K.; Staples, E. J.; Tucker, I.; Penfold, J., NEUTRON REFLECTION FROM A LAYER OF MONODODECYL HEXAETHYLENE GLYCOL ADSORBED AT THE AIR-LIQUID INTERFACE - THE CONFIGURATION OF THE ETHYLENE-GLYCOL CHAIN. *Journal of Physical Chemistry* **1993,** *97* (30), 8012-8020.
93. Vishnyakov, A.; Talaga, D. S.; Neimark, A. V., DPD Simulation of Protein Conformations: From alpha-Helices to beta-Structures. *J. Phys. Chem. Lett.* **2012,** *3* (21), 3081-3087.
94. Widom, B., Some Topics in the Theory of Fluids. *J. Chem. Phys.* **1963,** *39* (11), 2808-2812.
95. Shaw, D. G.; Maczynski, A.; Goral, M.; Wisniewska-Goclowska, B.; Skrzecz, A.; Owczarek, L.; Blazej, K.; Haulait-Pirson, M. C.; Hefter, G. T.; Kapuku, F.; Maczynska, Z.; Szafranski, A., IUPAC-NIST solubility data series. 81. Hydrocarbons with water and

seawater revised and updated. Part 7. C8H12-C8H18 hydrocarbons with water. *Journal of Physical and Chemical Reference Data* **2005,** *34* (4), 2261-2298.
96. Klamt, A.; Eckert, F., COSMO-RS: a novel and efficient method for the a priori prediction of thermophysical data of liquids. *Fluid Phase Equilibria* **2000,** *172* (1), 43-72.
97. Eckert, F.; Klamt, A. *COSMOtherm, Version C3.0, Release 12.01; COSMOlogic GmbH & Co. KG, Leverkusen, Germany, 2012*, 2012.
98. Yalkowsky, S. H.; He, Y., *Handbook of aqueous solubility data*. CRC Press LLC: 2003.
99. Saeki, S.; Kuwahara, N.; Nakata, M.; Kaneko, M., UPPER AND LOWER CRITICAL SOLUTION TEMPERATURES IN POLY (ETHYLENEGLYCOL) SOLUTIONS. *Polymer* **1976,** *17* (8), 685-689.
100. Martin, M. G.; Siepmann, J. I., Transferable potentials for phase equilibria. 1. United-atom description of n-alkanes. *J. Phys. Chem. B* **1998,** *102*, 2569-2577.
101. Pagonabarraga, I.; Hagen, M. H. J.; Frenkel, D., Self-consistent dissipative particle dynamics algorithm. *Europhysics Letters* **1998,** *42* (4), 377-382.
102. Berthod, A.; Tomer, S.; Dorsey, J. G., Polyoxyethylene alkyl ether nonionic surfactants: physicochemical properties and use for cholesterol determination in food. *Talanta* **2001,** *55* (1), 69-83.
103. Frindi, M.; Michels, B.; Zana, R., ULTRASONIC-ABSORPTION STUDIES OF SURFACTANT EXCHANGE BETWEEN MICELLES AND BULK PHASE IN AQUEOUS MICELLAR SOLUTIONS OF NONIONIC SURFACTANTS WITH A SHORT ALKYL CHAIN .2. C6E3, C6E5, C8E4, AND C8E8. *Journal of Physical Chemistry* **1992,** *96* (14), 6095-6102.
104. Calbiochem, *Detergents: A guide to the properties and uses in biological systems*. Calbiochem-Novabiochem Corporation: 2001.
105. Sigma-Aldrich D6277 SIGMA N-Decanoyl-N-methylglucamine ≥98% (GC). http://www.sigmaaldrich.com/catalog/product/sigma/d6277?lang=en&region=US.
106. Plimpton, S., FAST PARALLEL ALGORITHMS FOR SHORT-RANGE MOLECULAR-DYNAMICS. *Journal of Computational Physics* **1995,** *117* (1), 1-19.
107. Bhattacharya, A.; Mahanti, S. D.; Chakrabarti, A., Self-assembly of neutral and ionic surfactants: An off-lattice Monte Carlo approach. *Journal of Chemical Physics* **1998,** *108* (24), 10281-10293.
108. Panagiotopoulos, A. Z.; Floriano, M. A.; Kumar, S. K., Micellization and phase separation of diblock and triblock model surfactants. *Langmuir* **2002,** *18* (7), 2940-2948.
109. Rudnick, J.; Gaspari, G., THE ASPHERICITY OF RANDOM-WALKS. *Journal of Physics a-Mathematical and General* **1986,** *19* (4), L191-L193.
110. Noguchi, H.; Yoshikawa, K., Morphological variation in a collapsed single homopolymer chain. *Journal of Chemical Physics* **1998,** *109* (12), 5070-5077.
111. Zhang, Z.; Zheng, P.; Guo, Y.; Yang, Y.; Chen, Z.; Wang, X.; An, X.; Shen, W., The effect of the spacer rigidity on the aggregation behavior of two ester-containing Gemini surfactants. *Journal of Colloid and Interface Science* **2012,** *379*, 64-71.
112. NIH Sodium Cholate - Compound Summary (CID 23668194). http://pubchem.ncbi.nlm.nih.gov/summary/summary.cgi?cid=23668194.
113. Oviedo-Roa, R.; Martinez-Magadan, J. M.; Munoz-Colunga, A.; Gomez-Balderas, R.; Pons-Jimenez, M.; Zamudio-Rivera, L. S., Critical Micelle Concentration of an

Ammonium Salt Through DPD Simulations Using COSMO-RS-Based Interaction Parameters. *Aiche Journal* **2013,** *59* (11), 4413-4423.
114. Truszkowski, A.; Epple, M.; Fiethen, A.; Zielesny, A.; Kuhn, H., Molecular fragment dynamics study on the water-air interface behavior of non-ionic polyoxyethylene alkyl ether surfactants. *Journal of Colloid and Interface Science* **2013,** *410*, 140-145.
115. Jusufi, A.; Sanders, S.; Klein, M. L.; Panagiotopoulos, A. Z., Implicit-Solvent Models for Micellization: Nonionic Surfactants and Temperature-Dependent Properties. *Journal of Physical Chemistry B* **2011,** *115* (5), 990-1001.
116. Maczynski, A.; Shaw, D. G.; Goral, M.; Wisniewska-Goclowska, B.; Skrzecz, A.; Owczarek, I.; Blazej, K.; Haulait-Pirson, M. C.; Hefter, G. T.; Kapuku, F.; Maczynska, Z.; Young, C. L., IUPAC-NIST solubility data series. 81. Hydrocarbons with water and seawater-revised and updated. Part 4. C6H14 hydrocarbons with water. *Journal of Physical and Chemical Reference Data* **2005,** *34* (2), 709-753.
117. Shaw, D. G.; Maczynski, A.; Goral, M.; Wisniewska-Goclowska, B.; Skrzecz, A.; Owczarek, I.; Blazej, K.; Haulait-Pirson, M. C.; Hefter, G. T.; Huyskens, P. L.; Kapuku, F.; Maczynska, Z.; Szafranski, A., IUPAC-NIST solubility data series. 81. Hydrocarbons with water and seawater-revised and updated. Part 9. C-10 hydrocarbons with water. *Journal of Physical and Chemical Reference Data* **2006,** *35* (1), 93-151.
118. Kushare, S. K.; Shaikh, V. R.; TerdaleC, S. S.; Dagade, D. H.; Kolhapurkar, R. R.; Patil, K. J., Thermodynamics of aqueous polyethylene-glycol (PEG) solutions at 298.15 K: Activity, activity coefficients and application of molecular theories. *Journal of Molecular Liquids* **2013,** *187*, 129-136.
119. Malcolm, G. N.; Rowlinson, J. S., The thermodynamic properties of aqueous solutions of polyethylene glycol, polypropylene glycol and dioxane. *Transactions of the Faraday Society* **1957,** *53*, 921-931.
120. Kim, N. H.; Won, Y. S.; Choi, J. S., Partial molar heat of mixing at infinite dilution in solvent/polymer (PEG, PMMA, P(ET-VA)) solutions. *Fluid Phase Equilibria* **1998,** *146* (1-2), 223-246.
121. Zulauf, M.; Weckstrom, K.; Hayter, J. B.; Degiorgio, V.; Corti, M., NEUTRON-SCATTERING STUDY OF MICELLE STRUCTURE IN ISOTROPIC AQUEOUS-SOLUTIONS OF POLY(OXYETHYLENE) AMPHIPHILES. *Journal of Physical Chemistry* **1985,** *89* (15), 3411-3417.
122. Pivkin, I. V.; Karniadakis, G. E., Coarse-graining limits in open and wall-bounded dissipative particle dynamics systems. *Journal of Chemical Physics* **2006,** *124* (18).
123. Gonzalez-Melchor, M.; Mayoral, E.; Velazquez, M. E.; Alejandre, J., Electrostatic interactions in dissipative particle dynamics using the Ewald sums. *J. Chem. Phys.* **2006,** *125* (22).
124. Hofmann, D. W. M.; Kuleshova, L.; D'Aguanno, B., A new reactive potential for the molecular dynamics simulation of liquid water. *Chemical Physics Letters* **2007,** *448* (1-3), 138-143.
125. Hofmann, D. W. M.; Kuleshova, L.; D'Aguanno, B., Molecular dynamics simulation of hydrated Nafion with a reactive force field for water. *Journal of Molecular Modeling* **2008,** *14* (3), 225-235.
126. Selvan, M. E.; Keffer, D. J.; Cui, S., Reactive Molecular Dynamics Study of Proton Transport in Polymer Electrolyte Membranes. *Journal of Physical Chemistry C* **2011,** *115* (38), 18835-18846.

127. Choi, P.; Jalani, N. H.; Datta, R., Thermodynamics and proton transport in Nafion - II. Proton diffusion mechanisms and conductivity. *Journal of the Electrochemical Society* **2005,** *152* (3), E123-E130.
128. Kornyshev, A. A.; Kuznetsov, A. M.; Spohr, E.; Ulstrup, J., Kinetics of proton transport in water. *Journal of Physical Chemistry B* **2003,** *107* (15), 3351-3366.
129. Walbran, S.; Kornyshev, A. A., Proton transport in polarizable water. *Journal of Chemical Physics* **2001,** *114* (22), 10039-10048.
130. Jeffrey, G., *An introduction to hydrogen bonding*. Oxford University Press: 1997; p 12.
131. Cappadonia, M.; Erning, J. W.; Stimming, U., PROTON CONDUCTION OF NAFION((R))-117 MEMBRANE BETWEEN 140 K AND ROOM-TEMPERATURE. *Journal of Electroanalytical Chemistry* **1994,** *376* (1-2), 189-193.
132. Eikerling, M.; Kornyshev, A. A.; Spohr, E., Proton-Conducting Polymer Electrolyte Membranes: Water and Structure in Charge. In *Fuel Cells I*, Scherer, G. G., Ed. 2008; Vol. 215, pp 15-54.
133. Spohr, E.; Commer, P.; Kornyshev, A. A., Enhancing proton mobility in polymer electrolyte membranes: Lessons from molecular dynamics simulations. *Journal of Physical Chemistry B* **2002,** *106* (41), 10560-10569.
134. Klamt, A.; Schuurmann, G., COSMO - A NEW APPROACH TO DIELECTRIC SCREENING IN SOLVENTS WITH EXPLICIT EXPRESSIONS FOR THE SCREENING ENERGY AND ITS GRADIENT. *Journal of the Chemical Society-Perkin Transactions 2* **1993,** (5), 799-805.
135. Pulay, P.; Baker, J.; Wolinski, K. *Parallel Quantum Solutions (PQS)*, 1997.
136. Vishnyakov, A.; Lee, M. T.; Neimark, A. V., Prediction of the Critical Micelle Concentration of Nonionic Surfactants by Dissipative Particle Dynamics Simulations. *J. Phys. Chem. Lett.* **2013,** *4* (5), 797-802.
137. Roudgar, A.; Narasimachary, S. P.; Eikerling, M., Ab initio study of surface-mediated proton transfer in polymer electrolyte membranes. *Chem. Phys. Lett.* **2008,** *457* (4-6), 337-341.
138. Ioselevich, A. S.; Kornyshev, A. A.; Steinke, J. H. G., Fine morphology of proton-conducting ionomers. *Journal of Physical Chemistry B* **2004,** *108* (32), 11953-11963.
139. Jorn, R.; Voth, G. A., Mesoscale Simulation of Proton Transport in Proton Exchange Membranes. *Journal of Physical Chemistry C* **2012,** *116* (19), 10476-10489.
140. Lee, M.-T.; Vishnyakov, A.; Neimark, A. V., Proton Conductivity in Hydrated Polyelectrolyte Membrane by Dissipative Particle Dynamics Simulation. *Journal of Physical Chemistry B* **2015**, in preparation.
141. Klamt, A., Conductor-like Screening Model for Real Solvents: A New Approach to the Quantitative Calculation of Solvation Phenomena. *J. Phys. Chem.*, **1995,** *99*, 2224-2235.
142. Manoj, N. R.; Ratna, D.; Weiss, R. A., Diffusion of water in sulfonated polystyrene ionomers. *Macromolecular Research* **2004,** *12* (1), 26-31.
143. Schneider, N. S.; Rivin, D., Solvent transport in hydrocarbon and perfluorocarbon ionomers. *Polymer* **2006,** *47* (9), 3119-3131.
144. Connolly, M. L., ANALYTICAL MOLECULAR-SURFACE CALCULATION. *Journal of Applied Crystallography* **1983,** *16* (OCT), 548-558.

145. Gelb, L. D.; Gubbins, K. E., Pore size distributions in porous glasses: A computer simulation study. *Langmuir* **1999,** *15* (2), 305-308.
146. Sarkisov, L.; Harrison, A., Computational structure characterisation tools in application to ordered and disordered porous materials. *Molecular Simulation* **2011,** *37* (15), 1248-1257.
147. Sarkisov, L.; Harrison, A. *PoreBlazer*, 3.0.2; University of Edinburg: 2011.
148. Vishnyakov, A.; Neimark, A. V., Molecular dynamics simulation of microstructure and molecular mobilities in swollen Nafion membranes. *Journal of Physical Chemistry B* **2001,** *105* (39), 9586-9594.
149. Raamat, E.; Kaupmees, K.; Ovsjannikov, G.; Trummal, A.; Kütt, A.; Saame, J.; Koppel, I.; Kaljurand, I.; Lipping, L.; Rodima, T.; Pihl, V.; Koppel, I. A.; Leito, I., Acidities of strong neutral Brønsted acids in different media *J. Phys. Org. Chem.* **2013,** *26*, 162-170.
150. Hietala, S.; Maunu, S. L.; Sundholm, F.; Lehtinen, T.; Sundholm, G., Water sorption and diffusion coefficients of protons and water in PVDF-g-PSSA polymer electrolyte membranes. *Journal of Polymer Science Part B-Polymer Physics* **1999,** *37* (20), 2893-2900.
151. Carretta, N.; Tricoli, V.; Picchioni, F., Ionomeric membranes based on partially sulfonated poly(styrene): synthesis, proton conduction and methanol permeation. *Journal of Membrane Science* **2000,** *166* (2), 189-197.

Acknowledgement of previous publications

This thesis is the compilation of several published papers and papers in preparation. My contribution is specified as follows:

Section 3.

Reference: Vishnyakov, A.; Lee, M.-T.; Neimark, A. V., Prediction of the Critical Micelle Concentration of Nonionic Surfactants by Dissipative Particle Dynamics Simulations. *Journal of Physical Chemistry Letters* **2013,** *4* (5), 797-802.

Contribution: I performed all the calculations for this paper, but the original theoretic framework is proposed by Dr. Vishnyakov.

Section 4.

Reference: Lee, M.-T.; Vishnyakov, A.; Neimark, A. V., Calculations of Critical Micelle Concentration by Dissipative Particle Dynamics Simulations: The Role of Chain Rigidity. *Journal of Physical Chemistry B* **2013,** *117* (35), 10304-10310.

Contribution: I perform all the calculations for this paper, with the assistances from Dr. Vishnyakov and Dr. Neimark.

Section 5.

Paper in preparation: Lee, M.-T.; Vishnyakov, A.; Neimark, A. V., Parameterization of Chain Molecule in Dissipative Particle Dynamics. *Journal of Physical Chemistry B* **2015**, in preparation.

Contribution: I perform most the calculations for this paper. The determination of bond and rigidity coefficient was done by the mentored graduate student Runfang Mao.

Section 6.

Reference: Lee, M.-T.; Vishnyakov, A.; Neimark, A. V., Modeling Proton Dissociation and Transfer Using Dissipative Particle Dynamics Simulation. *J. Chem. Theory Comput.* **2015**.

Contribution: I performed all the calculations for this paper, with the assistances from Dr. Vishnyakov and Dr. Neimark.

Section 7.

Paper in preparation: Lee, M.-T.; Vishnyakov, A.; Neimark, A. V., Proton Conductivity in Hydrated Polyelectrolyte Membrane by Dissipative Particle Dynamics Simulation. *Journal of Physical Chemistry B* **2015**, in preparation.

Contribution: I performed all the calculations for this paper, with the assistances from Dr. Vishnyakov and Dr. Neimark